Metal–Organic Frameworks in Italy: From synthesis and advanced characterization to theoretical modeling and applications

Metal-Organic Frameworks in Italy: from synthesis and advanced characterization to theoretical modeling and applications

Giorgio Mercuri,[a,b] *Giuliano Giambastiani,*[a,c] *Corrado Di Nicola,*[b] *Claudio Pettinari,*[d] *Simona Galli,*[e] *Rebecca Vismara,*[e] *Riccardo Vivani,*[f] *Ferdinando Costantino,*[g] *Marco Taddei,*[h] *Cesare Atzori,*[i,j] *Francesca Bonino,*[i] *Silvia Bordiga,*[i] *Bartolomeo Civalleri*[i] *and Andrea Rossin*,*[a]

[a] Istituto di Chimica dei Composti Organometallici (ICCOM-CNR), Via Madonna del Piano 10, 50019 Sesto Fiorentino (Firenze), Italy.

[b] Scuola di Scienze e Tecnologie, Università di Camerino, Via S. Agostino 1, 62032 Camerino, Italy.

[c] Institute of Chemistry and Processes for Energy, Environment and Health (ICPEES), UMR 7515 CNRS-University of Strasbourg (UdS), 25, rue Becquerel, 67087 Strasbourg Cedex 02, France.

[d] Scuola del Farmaco e dei Prodotti della Salute, Università di Camerino, Via S. Agostino 1, 62032 Camerino, Italy.

[e] Dipartimento di Scienza e Alta Tecnologia, Università dell'Insubria, Via Valleggio 11, 22100 Como, Italy.

[f] Dipartimento di Scienze Farmaceutiche, Università di Perugia, Via del Liceo 1, I-06123 Perugia, Italy.

[g] Dipartimento di Chimica, Biologia e Biotecnologia, Università di Perugia e CIRCC, Via Elce di Sotto 8, I-06123 Perugia, Italy.

[h] Dipartimento di Chimica e Chimica Industriale, Università di Pisa, Via Giuseppe Moruzzi 13, 56124 Pisa, Italy.

[i] Dipartimento di Chimica, Centro interdipartimentale NIS e di riferimento INSTM, Università di Torino, Via G. Quarello 15, I-10135 and Via P. Giuria 7, I-10125 Torino, Italy.

[j] European Synchrotron Radiation Facility, 71 Avenue des Martyrs, CS 40220, 38043 Grenoble Cedex 9, France.

Author to whom correspondence should be addressed: a.rossin@iccom.cnr.it.

Abstract. As a celebration of the 44th International Conference on Coordination Chemistry (ICCC2022) that will take place in Italy, the Italian groups working in the research field of Metal-Organic Frameworks (MOFs) have decided to gather together and collect the results they have obtained in this area over the past 15 years. A survey that starts from the synthesis of novel heterocyclic linkers and the related MOFs and moves through advanced characterization techniques, theoretical investigations and assorted applications in the fields of gas storage and separation, heterogeneous catalysis, magnetism and sensing.

Keywords

Metal-Organic Frameworks – Italy – thiazole – pyrazole – tetrazole – phosphonate – formate – cerium – theoretical calculations – advanced characterization – heterogeneous catalysis – gas storage – gas separation – luminescence – magnetism

Introduction: history of MOFs in Italy

Metal-Organic Frameworks (MOFs) nowadays represent the main coordination chemistry investigation field, and the number of research groups dedicating their scientific efforts to this topic is constantly growing Worldwide. This is witnessed by the increasing popularity of MOF-dedicated International Conferences in terms of attendance or by the inclusion of MOF-centered Symposia within General/Coordination Chemistry meetings like the International Conference on Coordination Chemistry (ICCC) we are now celebrating in its Italian 2022 edition. MOFs extraordinary versatility as "Tinkertoy©" materials (built through a myriad of metallic building units / polytopic organic spacers pairings) is at the basis of the huge interest in their synthesis, characterization and applicative exploitation shown by many chemists, physicists and material scientists over the five Continents. The birth of a MOF research in Italy was not uniform; different groups over the country have independently turned their scientific interest to this topic, and only more recently some collaborative activities have started and have led to joint publications. The timeline of the start of MOF research in our research groups is sketched in Fig. 1.

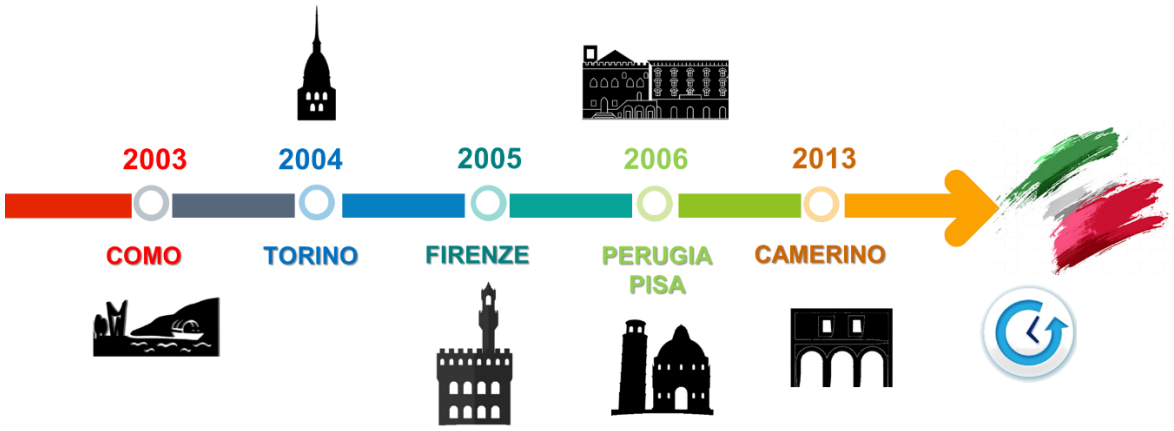

Fig. 1. Timeline illustrating when each Italian group authoring this review has started its own MOF research activity.

At odds with colleagues in other countries (like Germany)[1] whose MOF networks were born concomitantly with the approval of several national and international MOF-centered projects, the

Italian groups currently working on MOFs are not linked by any commonly funded project. The beginning of the MOF adventure in Firenze dates back to 2005, through the FIRENZE HYDROLAB (part I and II) projects funded by Ente Cassa di Risparmio di Firenze (ECRF, a private institution). Initially, the focus was on the preparation of MOFs for hydrogen storage. Over the years, the target has moved from hydrogen storage to carbon dioxide storage and valorization, in accordance with the targets of new projects that were funded later on, like the "Premiale Energia" project of the Italian National Research Council (CNR) in 2012 or the PRIN 2017 Multi-e project started in late 2019. The research activity on MOFs in Como started in 2003. The collaboration on this topic with the research group in Camerino began in 2006 on the occasion of a collaborative national project funded by the Ministero dell'Istruzione, dell'Università e della Ricerca (MIUR) devoted to multifunctional hybrid metal-organic materials with poly(azolate) linkers. Later on, the two groups continued their research activity in the MOF field with joint or separate works, also involving collaborators at the international level. The first functional property of choice studied by the Camerino and Como teams was hydrogen storage. Then, the focus of both groups moved on other applicative aspects, mainly carbon capture and heterogeneous catalysis. Torino started the activities on MOFs applying a multi-technique characterization (previously consolidated on zeolites) to MOF-5 in 2004.[2] This approach was extended to other materials developed for fundamental studies of H_2 and CO_2 capture within some EU projects of the VI and VII Framework Programme (MOFCAT, nanoMOF, MATESA). More or less at the same time, the theoretical modelling of MOFs began in Torino in the Theoretical Chemistry Group through quantum mechanical periodic calculations by means of the CRYSTAL code.[3] The first study on a MOF, reported in 2006, was a thorough investigation of MOF-5[4] that was still considered a challenge at that time. By starting from an initial interest in the adsorption capabilites of MOFs, the focus of the Theoretical Chemistry Group then moved to explore the rich portfolio of their physico-chemical properties (*i.e.* structural, electronic, dielectric, vibrational, elastic, mechanical, etc…) with the aim at highlighting the structure-property relationship. This was accomplished by fruitful collaborations with experimentalists in Torino and in other Italian Universities (Como and

Camerino) but also with colleagues in Oslo and Oxford. Research on MOFs in Perugia was born in the second half of 2000s as a spillover of the main research direction existing within the Inorganic Chemistry Laboratory since the 1970s, devoted to the chemistry of metal phosphates and phosphonates. The primary drive was the awareness that the outstanding stability of metal phosphonates, when compared to metal carboxylates, could serve to overcome one of the main pitfalls for MOFs. Main focus was the design and synthesis of new organic linkers, their use for the synthesis of metal derivatives (Mainly Zr and Cu) and structural characterization of these materials using powder-ray diffraction (PXRD) methods, often combined with other techniques, such as spectroscopies and gas sorption analysis. The work also involved collaborations with groups in Italy (Università di Milano-Bicocca, Università di Firenze), in the United States (University of California, San Diego) and in the United Kingdom (University of Swansea). Nowadays, each group that is part of this collective review has developed its own research niche in the MOF World. The geographical location of our research groups and the related main scientific activities is depicted in Fig. 2. Firenze has focused on the preparation of thiazole- and selenophene-containing MOFs for applications in CO_2 capture / conversion into added-value chemicals (the so-called "CCS+CCU" approach) and for luminescence sensing of polluting ions and small molecules. Torino has developed original characterization techniques and computational approaches for the study of MOFs peculiar physico-chemical properties; in the last few years, this team has synthesized cerium MOFs for CO_2 separation and storage. The Perugia and Pisa teams are expert in the synthesis and structural characterization of phosphonate-based MOFs and of cerium-based MOFs containing perfluorinated linkers for CO_2 capture. The Como and Camerino teams have focused their research activity on (poly)azolate-based MOFs for applications in CO_2 storage and catalysis, through which Como has built up a solid expertise in the structural characterization of (microcrystalline) powders, also under non ambient conditions.

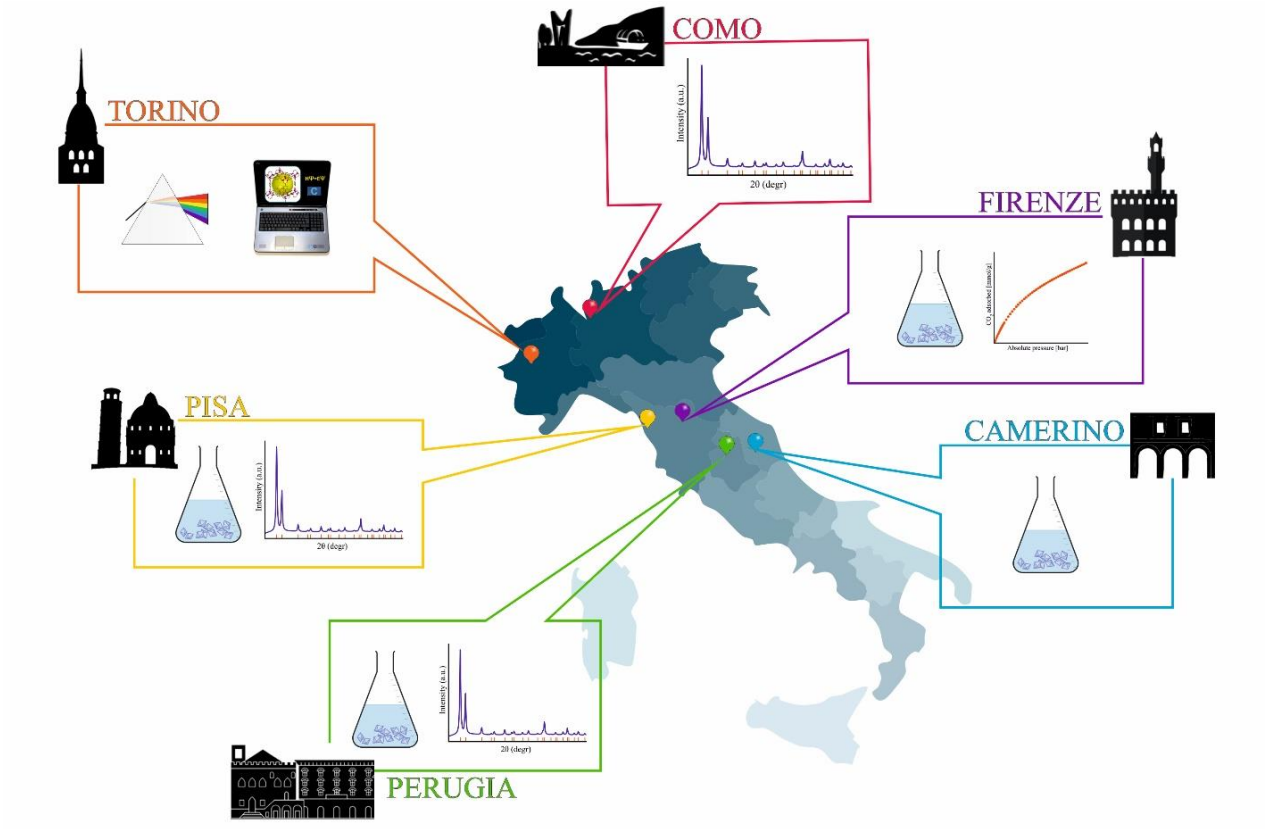

Fig. 2. Geographical distribution of the Italian research units working in MOFs and the related main scientific activities.

Many collaborative papers written by two or more Italian groups have started to appear since 2010. The first example in this respect comes from Torino and Como, with the extended structural characterization of the [Ni_8] MOF discussed in Chapter 2 at the periodic and local levels, by juxtaposing powder X-ray diffraction and X-ray absorption, infrared and UV-Vis spectroscopy, respectively. Since then, further joint activities have followed: a Torino-Firenze collaborative work published in 2012 describing the cobalt(II) thiazolidine MOF reported in Section 1.2; a series of joint papers Firenze-Como-Camerino published between 2018 and 2020 on the synthesis, characterization and application in carbon dioxide storage and valorization or heterogeneous catalysis with tagged bipyrazolate MOFs, detailed in Section 1.1.2. The scientific outcomes obtained by these groups over the past 15 years are collected and discussed in this review. Over this time period, MOF research in Italy has also benefited from excellent international cooperation with other research groups all over

the World (in Germany, Spain, United Kingdom and United States in particular). With this review, we would like to celebrate our results and also set the start of future national and international new joint activities and prospective scientific exchange.

1. Novel MOFs in Italy: from synthetic paths to key structural aspects

1.1 Pyrazole- and tetrazole-based MOFs (Como, Camerino, Firenze)

This project line initially developed (jointly or independently) by the research groups based in Camerino and Como has mainly focused on the synthesis and structural/functional characterization of MOFs containing rigid or flexible poly(azolate) spacers. The interest for this class of linkers can be traced back to their higher basicity *vs.* the corresponding poly(carboxylate) linkers, which grants stronger coordination bonds and related thermal and chemical stability to the corresponding MOFs, as extensively shown by us and other research groups.[5-10] Furthermore, metal-to-nitrogen coordinative bonds are less affected by hydrolysis than those involving oxygen donors.[11-13] On this basis, in the past twenty years poly(azolate)-containing linkers have raised increasing interest as a valid alternative to poly(carboxylate)-based spacers in MOFs preparation.[5, 6] Among azoles, pyrazole is the strongest base (pK_a in DMSO 19.8), which implies that pyrazolate forms stronger coordinative bonds than those involving other azolates (*e.g.* tetrazolate, 1,2,3-triazolate, 1,2,4-triazolate, and imidazolate, with pK_a in DMSO of 8.3, 13.9, 14.8 and 18.2, respectively),[14] with a significant impact on the thermal and chemical stability of its derivatives.[15] Deprotonation of pyrazole concomitantly increases its hapticity and basicity. Moreover, due to the position of its nitrogen donor atoms, pyrazolate can coordinate in a symmetric *exo*-bidentate mode featuring a bridging angle of ~70°, which enables to keep two metal centers at a distance ranging between 3.5 and 4.7 Å, depending on the metal ionic radius.[6] Tetrazole is the weakest base among the azoles;[14] consequently, tetrazolate forms weaker coordinative bonds than other azolates, this resulting into a lower thermal stability of the corresponding coordination compounds. At variance,

owing to its four nitrogen donor atoms, the tetrazolate anion displays seven different coordination modes, with hapticity ranging between two and four (Scheme 1).

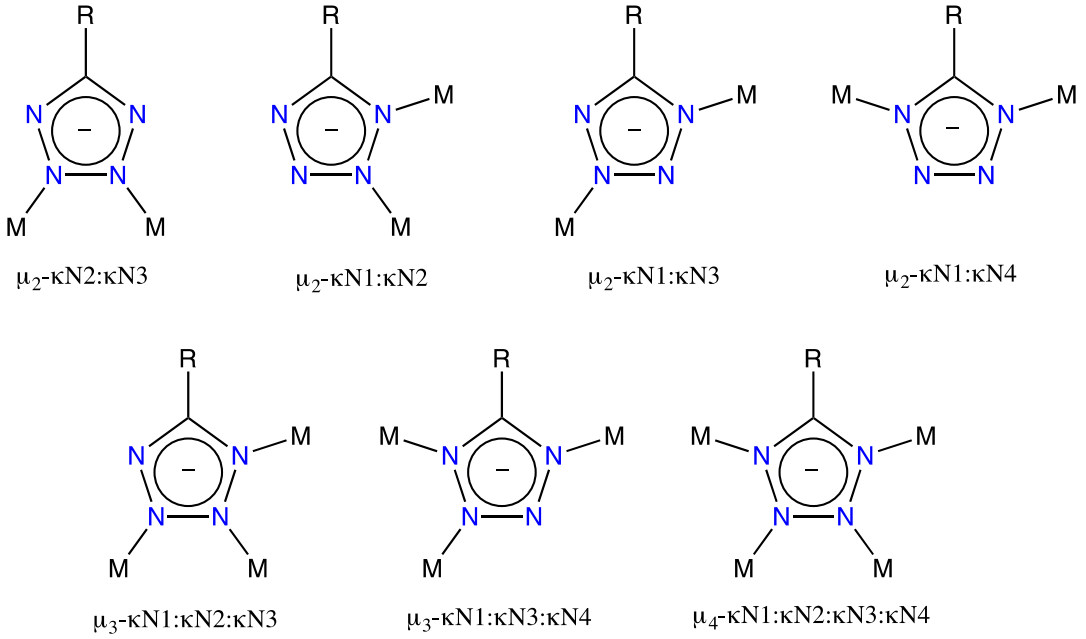

Scheme 1. The different coordination modes of the tetrazolate anion.

Tetrazole-based linkers tailored synthesis is a widely explored investigation field, because of their rich coordination chemistry; nowadays, there is a vast library of tetrazole-containing coordination polymers and metal-organic frameworks[16] displaying a variety of physical properties, ranging from fluorescence to ferroelectric and dielectric behavior.[17] All the azole linkers described in this section along with the related MOFs are collected in Table 1.

Table 1. List of the poly(azole)-linkers and the corresponding MOFs reported in this section, along with the corresponding BET specific surface areas (SSAs) and decomposition temperatures.

Linker	Compound	BET SSA (m^2/g)	T_{dec} (°C)	Ref.

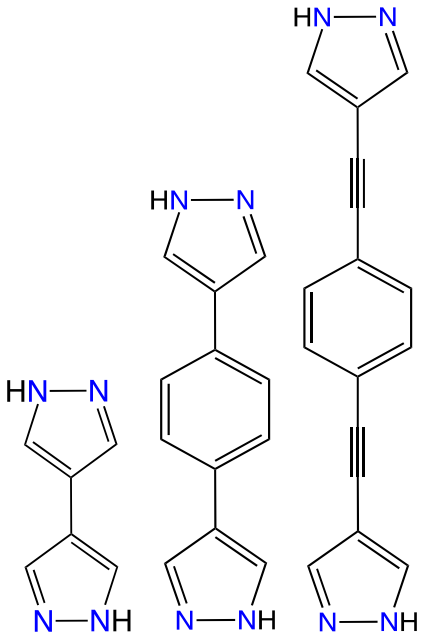

H_2BPZ H_2BDP H_2BPEB

Cd(BPZ)	993	350	[18]
Co(BPZ)	926	320	[18]
Cu(BPZ)	314	350	[18]
Ni(BPZ)	767	330	[18]
Zn(BPZ)	778	450	[18]
Ni(BDP)	1600	460	[19]
Zn(BDP)	2200	410	[19]
$Fe_3(BPEB)_2$	1273	415	[20]
Ni(BPEB)	1900	422	[20]
Zn(BPEB)	985	410	[20]

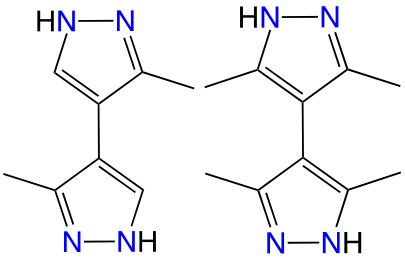

H_2Me_2BPZ H_2Me_4BPZ

$Co(Me_2BPZ)$	434	340	[21]
$Zn(Me_2BPZ)$	290	460	[21]
$Cd(Me_4BPZ)$	88	430	[22],[23]
$Co(Me_4BPZ)$	318	320	[22],[23]
$Cu(Me_4BPZ)$	376	320	[22],[23]
$Zn(Me_4BPZ)$	396	400	[22],[23]

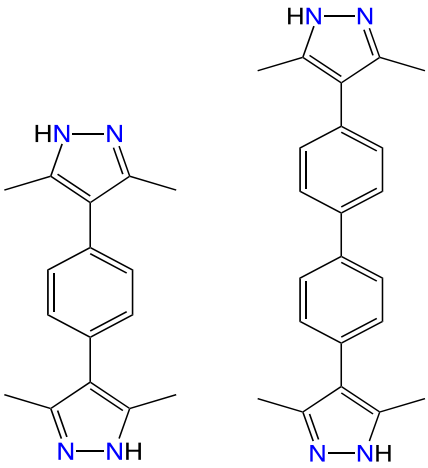

H_2Me_4BDP H_2Me_4BDPB

$Cd(Me_4BDPB)$	427	420	[24]
$Co(Me_4BDP)$	791	450	[24]

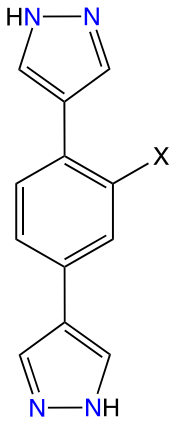

H_2BDPX
(X = -NO_2, -NH_2,
-OH, -SO_3H)

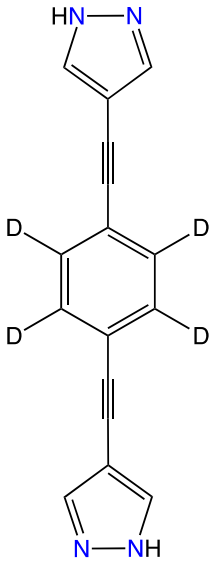

d_4-H_2BPEB

Ni(BDPNO_2)	1131	400	[25]
Ni(BDPNH_2)	1305	470	[25]
Ni(BDPOH)	1103	450	[25]
Ni(BDPSO_3H)	819	410	[25]
Zn(BDPNO_2)	1875	420	[25]
Zn(BDPNH_2)	1345	470	[25]
Zn(BDPOH)	1170	420	[25]
Zn(d_4-BPEB)	1214	-	[26]

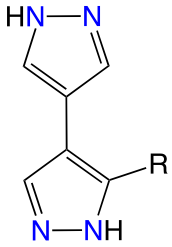

H_2BPZNO_2: R = NO_2
H_2BPZNH_2: R = NH_2

Co(BPZNO_2)	645	350	[27]
Cu(BPZNO_2)	408	310	[27]
Zn(BPZNO_2)	916	390	[27]
Cu(BPZNH_2)	100	290	[28]
Ni(BPZNH_2)	182	390	[28]
Zn(BPZNH_2)	395	430	[28]

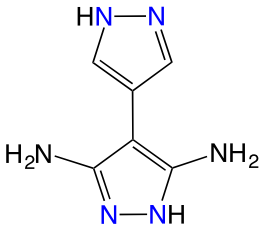

$H_2$3,5NH_2BPZ

Zn(3,5NH_2BPZ)	155	450	[29]

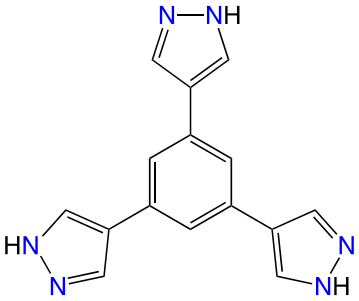

H_3BTP

Co_3(BTP)$_2$	1027	450	[30]
Cu_3(BTP)$_2$	1860	390	[30]
Ni_3(BTP)$_2$	1650	450	[30]
Zn_3(BTP)$_2$	930	510	[30]
$Cu^{I}_4Cu^{II}_2$(OH)$_2$(BTPP)$_2$	660	350	[31]

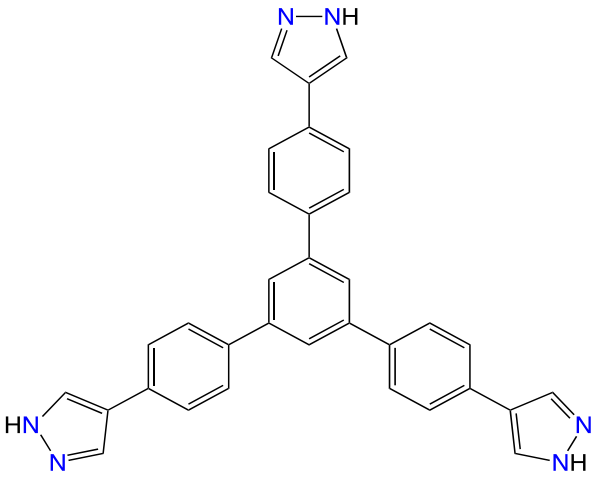

H_3BTPP

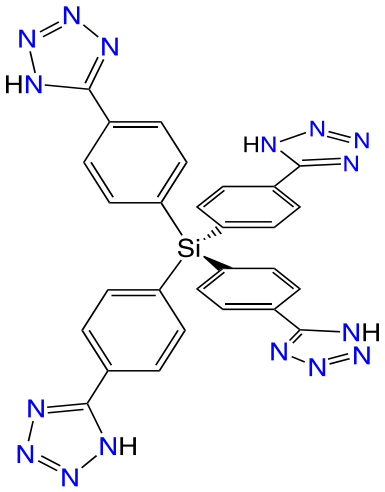

H_4ttps

IMP-16Cu	2665	240	[32],[33]
IMP-16Mn	2510	200	[32],[33]
IMP-17Cd	-	-	[33]
IMP-17Cu	-	-	[33]
IMP-17Mn	-	-	[33]

1.1.1 Bipyrazole-based MOFs (Como, Camerino)

We started the investigation on the coordination chemistry of the rigid ditopic linkers 4,4′-bipyrazole (H_2BPZ) and 1,4-bis(pyrazolyl)benzene (H_2BDP) (Table 1) with late transition metals between 2010 and 2011. Before that date, only a few articles had appeared on the subject dealing with transition-metal coordination compounds containing H_2BPZ in its neutral form as bidentate linker[34] or in dianionic form as tetradentate linker.[35] More recently, the longer H_2BPEB spacer (Table 1) was also engineered and prepared. H_2BPZ was synthesized as reported by Domasevich and coworkers,[34] while H_2BDP[36] and H_2BPEB[20] were prepared following synthetic routes originally tailored in Como. The preparation of the M(BPZ) (M = Co, Ni, Cu, Zn) MOFs required either a conventional synthetic route in the presence of a base or solvothermal conditions.[18]

Isolation of M(BDP) (M = Co, Ni, Zn),[19] M(BPEB) (M = Ni, Zn) and $Fe_3(BPEB)_2$[20] proceeded through classical synthetic routes. All these compounds precipitate in the form of air- and moisture-stable microcrystalline powders with decomposition temperatures between 320 and 460 °C (Table 1). The M(BPZ) (M = Co, Zn) and Zn(BDP) MOFs on one hand, and the M(BPZ) (M = Ni, Cu), Ni(BDP) and Ni(BPEB) compounds on the other hand, form two isoreticular series. Their open framework is characterized by MN_4 tetrahedral (M = Co, Zn) or square planar (M = Cu, Ni) nodes bridged through *exo*-tetradentate spacers to form 3D architectures featuring 1D square (M = Co, Zn; Fig. 3a) or diamond-shaped (M = Cu, Ni; Fig 3b) channels. As expected, the empty volume increases as a function of the spacer length, being 40-42%, 57-65% and 70% in M(BPZ), M(BDP) and Ni(BPEB), respectively. Unexpectedly, Zn(BPEB) and Zn(BPZ) [or Zn(BDP)] are not isoreticular, despite sharing the same stereochemistry at the metal ion and possessing a 3D open framework with 1D rhombic channels. Interpenetration about the spacer triple bonds is observed, this occurrence implying an empty volume (42%) comparable to that of Zn(BPZ). Finally, $Fe_3(BPEB)_2$ shows octahedral FeN_6 nodes bridged by exo-tetradentate spacers within a 3D open framework with 1D triangular channels (Fig. 3c) resulting into an empty volume of 64%.

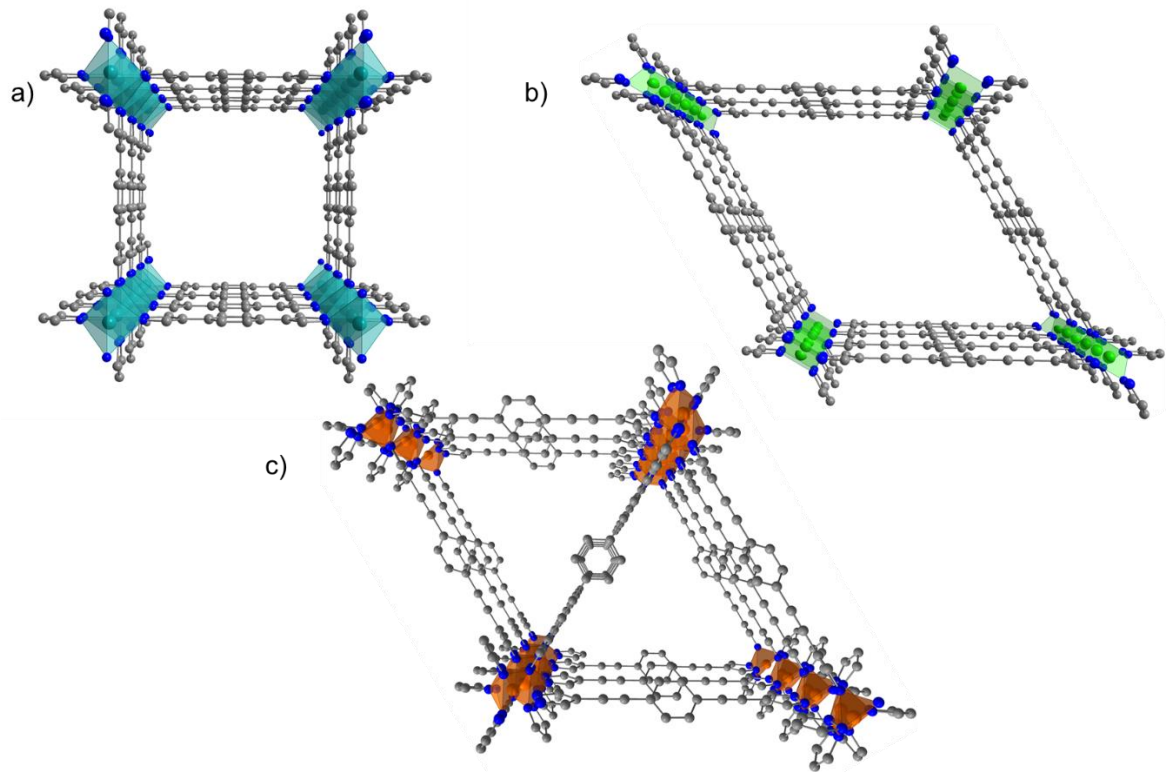

Fig. 3. Portion of the crystal structure of Zn(BDP) (a), Ni(BPEB) (b) and $Fe_3(BPEB)_2$ (c) showing the channels shape. Hydrogen atoms on the linkers and clathrated solvent molecules in the channels omitted for clarity. Atom color code: gray, C; blue, N; turquoise, Zn; green, Ni; orange, Fe. Adapted from refs.[19] and [20].

1.1.2 Tagged bipyrazole-based MOFs (Como, Camerino, Firenze)

As a natural development of the research line described above, we decided to study the effect of substituents of different chemical nature and/or steric hindrance (-CH_3, -NO_2, -NH_2, -OH, -SO_3H), decorating the channels walls on the functional properties of the corresponding MOFs, preserving the structural motif with respect to the parent, unfunctionalized material. With this aim, a wide variety of tagged linkers have been prepared (Table 1). The role of the steric hindrance of the substituent(s) on a rigid, linear skeleton with increasing length was investigated upon preparing 3,3′-dimethyl-1*H*,1′*H*-4,4′-bipyrazole (H_2Me_2BPZ),[21] tetramethyl-1*H*,1′*H*-4,4'-bipyrazole (H_2Me_4BPZ),[22] 1,4-bis-4′-(3′,5′-dimethyl)-pyrazolylbenzene (H_2Me_4BDP) and 1,4-bis-4′-(3′,5′-dimethyl-pyrazolyl)biphenyl (H_2Me_4BDPB). H_2Me_2BPZ and H_2Me_4BPZ were prepared adopting the synthetic paths proposed by Sharko *et al.*[37] and Mosby[38] respectively, whereas the linkers H_2Me_4BDP and H_2Me_4BDPB were prepared following the synthesis reported by Li and co-workers,[39] based on the condensation of the pertinent bis(diketone) with hydrazine hydrate in aqueous medium. These methyl-functionalized linkers were employed in the isolation of the corresponding MOFs M(Me_2BPZ) (M = Co, Zn),[21] M(Me_4BPZ)[22] (M = Co, Cu, Zn), Co(Me_4BDP) and Cd(Me_4BDPB).[24] These MOFs were prepared through solvothermal routes by reacting H_2Me_4BPZ and the pertinent MX_2 salt [*N*,*N*-dimethylformamide (DMF), 100-150 °C, autogenous pressure, 24 h]. To isolate Cu(Me_4BPZ), the temperature of 100 °C was adopted to prevent the Cu^{II} to Cu^{I} reduction. All these compounds were isolated in the form of air- and moisture-stable powdery batches, which are not soluble in water and in the most common organic solvents, and show moderate to remarkable thermal stability (Table 1), clearly influenced by the different redox reactivity of the involved metal ions. The M(Me_2BPZ) (M = Co, Zn) and M(Me_4BPZ) (M = Co, Cu, Zn) series as well as Co(Me_4BDP) share the same structural motif of the untagged parents M(BPZ) (M = Co, Cu, Zn) and Co(BDP), with an expected decrease of

the empty volume percentage [15% vs. 38% vs. 40-42%, respectively, moving from M(Me_4BPZ) to M(Me_2BPZ) and M(BDP); 57% vs. 65%, respectively, on passing from Co(Me_4BDP) to Co(BDP)]. On the other hand, Cd(Me_4BDPB) (where the linker rings are not coplanar) shows a different 3D open framework featuring 1D slit-like channels. The chemical nature of the substituent was modified besides its steric hindrance, to verify the role of its polarity on the functional properties. To this aim, we engineered and prepared the linkers 3-X-4,4'-bipyrazole (H_2BPZX; X = NO_2, NH_2), 3,5-diamino-4,4'-bipyrazole (3,5-H_2BPZNH_2), 2-X-1,4-bis(1*H*-pyrazol-4-yl)benzene (H_2BDPX; X = -NO_2, -OH, -SO_3H) and 1,4-bis(1*H*-pyrazol-4-ylethynyl)benzene-d_4 (d_4-H_2BPEB) (Table 1). H_2BPZNO_2[27] and H_2BDPNO_2[25] were synthesized through direct nitration of the untagged spacer. H_2BPZNH_2[28] and 3,5-H_2BPZNH_2[29] were prepared from the reduction of their nitro-functionalized analogues in 2-propanol, using hydrazine as a reducing agent and a Ni-Re slurry as catalyst. The amino functionalized H_2BDPNH_2 spacer was prepared upon reducing H_2BDPNO_2 with ammonium formate in DMF adopting Pd/C as catalyst.[25] H_2BDPOH was subsequently obtained treating H_2BDPNH_2 with $NaNO_2$, followed by addition of $H_2SO_{4(aq)}$, while H_2BDPSO_3H was synthesized by directly treating H_2BDP with fuming H_2SO_4.[25] Finally, the synthesis of d_4-H_2BPEB proceeded as that of H_2BPEB, starting from the proper perdeuterated precursor.[26] The MOFs M(BPZNO_2) (M = Co, Cu, Zn),[27] M(BPZNH_2) (M = Ni, Cu, Zn)[28] and Zn(3,5-BPZNH_2)[29] were isolated as microcrystalline powders by combining the corresponding metal acetates (or nitrate in the case of cobalt) with the nitro- or amino-substituted organic linkers, under solvothermal conditions in DMF. As a general procedure, the M(BDPX) families (M = Ni, Zn; X = NO_2, NH_2, OH) were prepared along classical routes upon reacting the proper metal acetate and linker (DMF, 60 °C, 5 h), while Ni(BDPSO_3H) was obtained coupling $Ni(CH_3COO)_2 \cdot 4H_2O$ and the linker (DMF:DMSO = 1:1 v/v, 160 °C, 5 h).[25] Zn(d_4-BPEB)[26] was straightforwardly isolated following the same protocol adopted for the Zn(BPEB) parent. Also in this case, the structural motif of the tagged M(Me_2BPZ), M(Me_4BPZ), M(BDPX) and deuterated Zn(d_4-BPEB) MOFs can be traced back to that of the parent M(BPZ) and M(BDP) and M(BPEB) compounds sharing the same metal ion. In the case of

Ni(BDPSO$_3$H) though, its 3D open framework shows 1D rhombic channels but the nodes are octahedral NiN_4O_2 moieties, because of the different coordination geometry at the metal center that includes the sulfonic groups on the linker.

1.1.3. Tris(pyrazole)-based MOFs (Como, Camerino)

The two tris(pyrazoles) 1,3,5-tris(1*H*-pyrazol-4-yl)benzene, (H_3BTP)[30] and 1,3,5-tris((1*H*-pyrazol-4-yl)phenyl)benzene (H_3BTPP)[31] (Table 1) were synthesized *via* the Suzuki coupling of 1-(tetrahydro-pyran-2-yl)-4-pyrazoleboronic acid pinacol ester with 1,3,5-tribromobenzene and 1,3,5-tris(4-bromophenyl)benzene, respectively, in a mixture of dioxane and water, by adopting a very similar procedure to that reported in the literature.[40] Combining H_3BTP with nickel(II), copper(II) and cobalt(II) acetate or Zn(CF_3SO_3) under solvothermal reaction conditions (DMF, 160 °C) afforded the MOFs $M_3(BTP)_2$.[30] At variance, $Cu^I_4Cu^{II}_2(OH)_2(BTPP)_2$ was synthesized with the reaction temperature carefully set at 80 °C to avoid the complete reduction of Cu^{II} to Cu^I and the concomitant formation of a mixture of undesirable products.[31] Yields of these reactions are usually high, and all these MOFs could be obtained as air-stable powders insoluble in water and in most common solvents, and show moderate to remarkable decomposition temperatures (Table 1). The chemical stability of $Ni_3(BTP)_2$ and $Zn_3(BTP)_2$ is also remarkable, as they survive in boiling aqueous solutions of pH 2-14 for at least 14 days. $Ni_3(BTP)_2$ and $Cu_3(BTP)_2$ share the same sodalitic structural motif, in which square $M_4(pz)_8$ (pz = pyrazolate) nodes are bridged by the spacers to eight neighboring ones forming a 3D open framework (Fig. 4a) containing octahedral cages (Fig. 4b) separated by 1D channels. At variance, the isostructural MOFs $Zn_3(BTP)_2$ and $Co_3(BTP)_2$ show a 3D open framework with 1D channels. Finally, $Cu^I_4Cu^{II}_2(OH)_2(BTPP)_2$ is an example of 2D open framework in which the layers are formed by $CuN_6(OH)$ nodes bridged by the spacers to other six nodes, this resulting into 1D hexagonal channels.

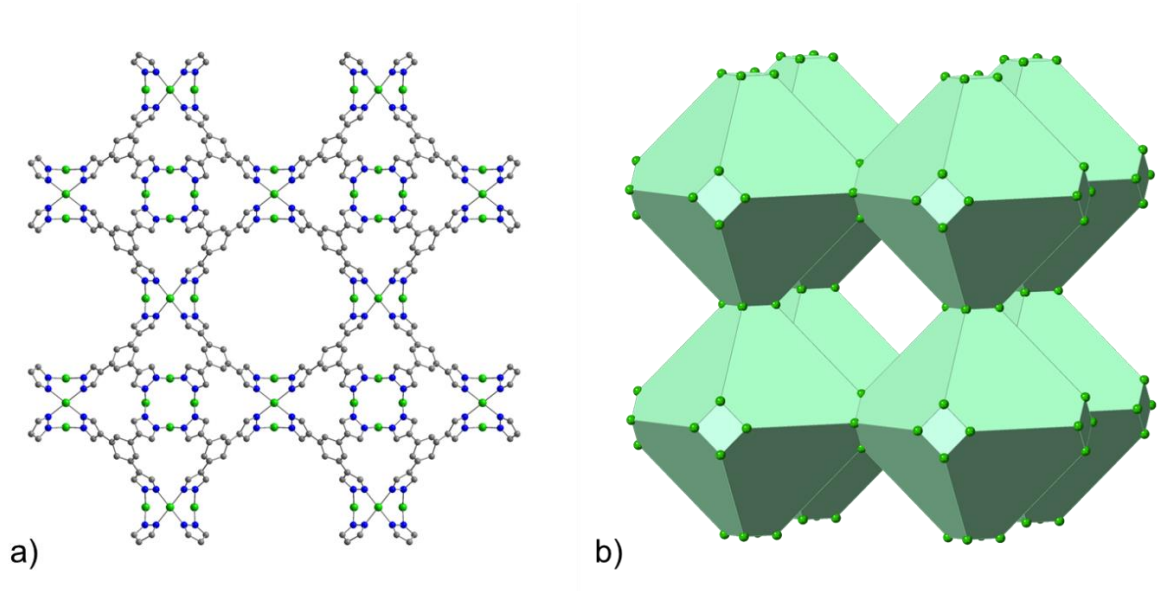

Fig. 4. Portion of the crystal structure of $Ni_3(BTP)_2$ (a) and schematic representation of its sodalite-like network topology highlighting the octahedral cavities (b). Hydrogen atoms on the linkers and solvent molecules in the pores omitted for clarity. Atom color code: gray, C; blue, N; green, Ni. Adapted from ref.[30].

1.1.4. Tetrazole-based MOFs (Camerino)

Beside poly(pyrazolates), poly(tetrazolates) are one of the most popular azolate families in the preparation of MOFs and coordination polymers. In tetrazolate-based MOFs, the N atoms that are not involved in the coordination to the metal centers may act as basic sites with high affinity for CO_2.[6, 41] Some tetrazolyl-containing linkers have been exploited for the isolation of MOFs having potential application as high-energy-density materials.[42] In 2013, we synthesized the new tetratopic linker tetrakis(4-tetrazolylphenyl)silane (H_4ttps, Table 1), the silicon analogue of the known carbon-centered tetrakis(4-tetrazolylphenyl)methane (H_4ttpm). The presence of silicon instead of carbon in this linker has some influence on the structure and properties of the corresponding MOF.[43] In addition, H_4ttps can be straightforwardly synthesized taking advantage of inexpensive and commercially available starting materials. Indeed, it was prepared from the tetracyano organosilicon $Si(C_6H_4CN)_4$ (easily obtained from $SiCl_4$ and BrC_6H_4CN) via a [2+3] cycloaddition reaction with sodium azide.[32] The isostructural MOFs $H(M_4Cl)(ttps)_2(DMF)_4 \cdot nDMF$ (IMP-16Cu, M = Cu, n = 18; IMP-16Mn, M = Mn, n = 20) were isolated as microcrystalline powders upon coupling H_4ttps and

the metal chlorides (DMF:methanol, 80 °C). Both MOFs are moderately stable and display a high BET specific surface area (Table 1). When $CdCl_2$ was exploited as metal-containing reagent, the IMP-16Cd analogue could not be obtained as expected, giving instead a mixture of phases of unknown nature. The IMP-16M compounds are a rare example (for MOFs) of (8,4)-connected net with fluorite topology: their crystal structure is characterized by chloride-centered square-planar $\{Cu_4(\mu_4\text{-}Cl)\}^+$ SBUs, in which the metal ions show a square pyramidal coordination and which are reciprocally connected by octadentate spacers. In order to understand if the counterion type (or its absence) could have some influence in the syntheses, the reactions of metal nitrates with the H_4ttps connector were carried out applying the same synthetic procedure described above, yielding the isotructural $M_6(ttps)_3(DMF)_6$ (IMP-17Mn, IMP-17Cu and IMP-17Cd for M = Mn, Cu, Cd, respectively) MOFs. Their (4,6)-connected 3D net of garnite topology, another rare topology for MOFs, is characterized by linear, trinuclear nodes, in which the metal ions show two distinct octahedral coordination spheres (MN_6 and *fac*-MN_3O_3). In contrast with the IMP-16M series, the IMP-17M one showed limited stability: IMP-17Cd and IMP-17Cu decompose within 24 hours when left in air, and all of them decompose rapidly also under thermal activation.

1.2 Thiazole-based MOFs (Firenze)

Interest in thiazole-containing MOFs stems from the intriguing physico-chemical properties of this heterocycle. Thiazoles are the simplest (N,S)-containing heterocycles, and both the hard (N) and the soft (S) base that are part of the organic ring modify the electron density distribution with respect to their fully carbocyclic analouges. Thiazoles luminescence is evident in natural biomolecules (often fused with benzene derivatives, *i.e.* benzothiazoles) like vitamin B1 (thiamine) or luciferin (the substance responsible for fireflies natural luminescence). From a medicinal point of view, thiazoles have found wide applications in the synthesis of dyes and fungicides like thifluzamide and tricyclazole, marketed for control of various agricultural pests. Another application field growing in

interest is the prepration of (thiazolo)thiazole-based organic sensitizers as light-responsive dyes to be incorporated within solar cells (DSSC) for the generation of renewable energy sources (mainly hydrogen through photocatalytic water splitting). The thiazole/thiazolidine-based linkers and related MOFs discussed in this work are collected in Table 2.

Table 2. List of the thiazole/thiazolidine-based linkers and the corresponding MOFs reported in this section, along with the corresponding BET specific surface areas (SSAs) and decomposition temperature. n.p. = non porous.

Linker	Compound	BET SSA (m^2/g)	T_{dec} (°C)	Ref.
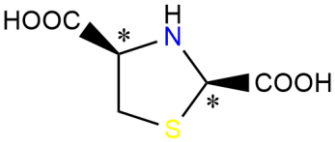 H_2L-*RR*	Co(L-*RR*)(H_2O)	n.p.	290	[44]
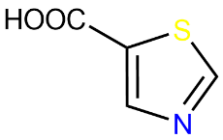 5-TzCOOH	Cu(5-TzCOO)$_2$·1.5 (H_2O)	n.p.	220	[45]
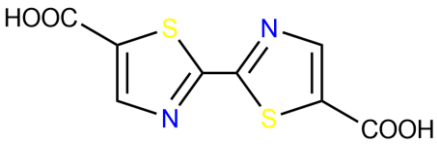 H_2TzTz	[$Zr_6O_4(OH)_4$(TzTz)$_6$]	840	500	[46]
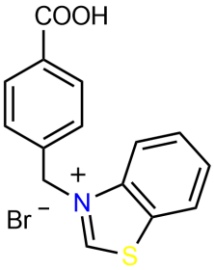 (HBzTz)Br	[$Zr_6O_4(OH)_{6.3}(H_2O)_4$(TBAPy)$_2$] ·1.7(BzTz)Br	1530	507	[47]

At the beginning of 2010, the Firenze team started the investigation on the chemistry of thiazole- and thiazolidine-based polycarboxylates. The very first publication on these linkers preparation dates back to 2011, describing the multi-gram scale and microwave-aided synthesis of a library of 2-

substituted-4-carboxy thiazoles and thiazolidines by condensation of the naturally occurring amino acid cysteine with aldehydes.[48] This new synthetic protocol is greener and less energy-demanding than the traditional Hantzch thiazole synthesis (*i.e.* the condensation of an α-halocarbonyl compound with a thioamide). In the same year, a collection of 0D discrete coordination compounds was published, obtained through the combination of Zn^{II}, Co^{II} and Cu^{II} salts with thiazole-2-carboxylic acid, thiazole-4-carboxylic acid and [2-(2-pyridyl)thiazole-4-carboxylic acid] under hydrothermal conditions in stainless steel autoclaves.[49] The presence of an extended hydrogen-bonding network due to the several hydrogen donor/acceptor polar groups confers a "pseudopolymeric" nature on these solids, being insoluble in all solvents. The linkers coordination mode is invariably η^2-(κ-N:κ-O), chelating a single metal ion. No polymeric compounds can be obtained when the carboxylic function is either in the 2- or in the 4-position of the heterocyclic ring. From this perspective, this study has to be considered as a propaedeutic step towards the synthesis of genuine thiazole-based MOFs.

One year later, in Firenze we succeeded in the preparation of a MOF by combining hydrated $CoCl_2$ with the polytopic aliphatic spacer thiazolidine-2,4-dicarboxylic acid (Table 2) in its (*R*,*R*) enantiomerically pure form, obtained through selective precipitation from a (*R*,*R*)/(*S*,*R*) diastereomeric mixture. The hydrothermal synthesis (T = 90 °C, 24 h) led to a MOF with minimal formula Co(L-*RR*)(H_2O)·H_2O.[44] The obtained MOF contains only the (*R*,*R*) linker enantiomer and it shows the same optical activity. The coordination geometry at cobalt is octahedral, and the linker occupies five coordination sites through its N atom and the four O atoms from the carboxylate groups (Fig. 5a). The last site hosts one water molecule as *aquo* ligand. The resulting 3D framework is featured by two alternating channels (Fig. 5b), being either hydrophobic (when the sulfur atoms protrude in the pores) or hydrophilic (from the *aquo* ligand side sitting on cobalt). In the latter, a number of water molecules as crystallization solvent can be found. Co(L-*RR*)(H_2O)·H_2O has been characterized through a plethora of techniques: X-ray diffraction, Circular Dichroism (CD), Infrared Spectroscopy (IR), UV-Visible spectroscopy, X-ray Absorption Near Edge Structure (XANES),

extended X-Ray absorption fine-structure (EXAFS). The dehydration process leads to a color change from pink to violet.

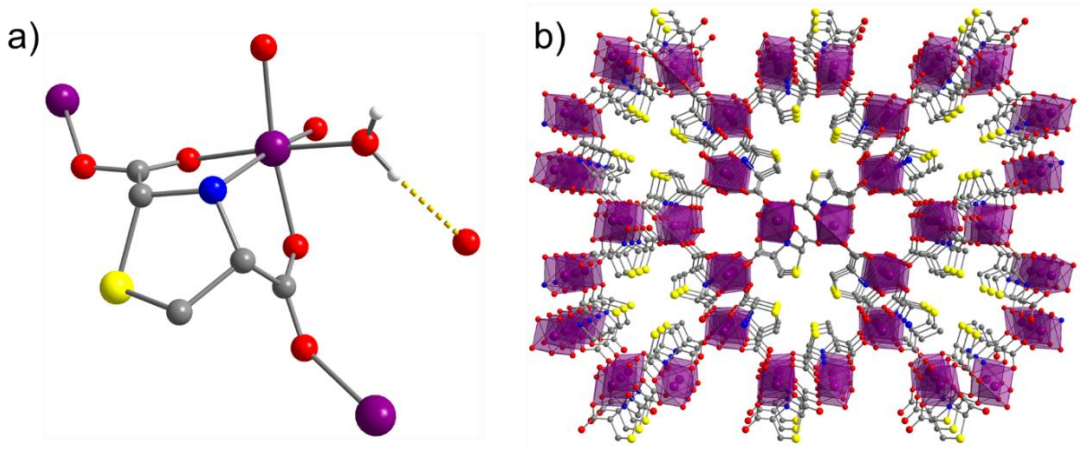

Fig. 5. Representation of the metal coordination environment (a) and of portion of the crystal structure (b) of [Co(L-*RR*)(H_2O)·H_2O], where L-RR^{2-} = (*R*,*R*)-thiazolidine-2,4-dicarboxylate. Atom color code: black, C; white, H; red, O; blue, N; yellow, S; purple, Co. Adapted from ref.[44].

The following step in linker design was to move the carboxylic function from the 4- to the 5-position on the thiazole ring, since the experimental evidence collected so far showed that in the former case (N,O)-chelation over a single metal center and formation of discrete 0D coordination compounds is preferred to bridging two or more metal centers to build a polymeric structure. Thus, simple thiazole-5-carboxylic acid and its 2-amino substituted analogue were employed as linkers in the construction of 1D and 2D coordination polymers (CPs) in combination with Cu^{II}.[45] The 2D polymer Cu(5-$TzCOO)_2$·1.5 (H_2O) (5-$TzCOO^-$ = thiazole-5-carboxylate, Table 2 and Fig. 6) features a porous structure containing square channels formed by the ordered stacking of planar sheets. In this CP, the is bridging nearby Cu^{II} ions through its N atom and the $–COO^-$ group; the coordination geometry around the metal center is distorted octahedral.

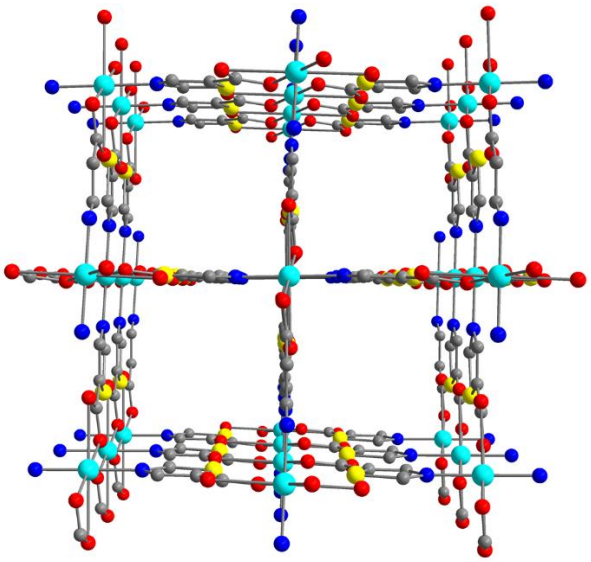

Fig. 6. Portion of the crystal structure of Cu(5-TzCOO)$_2$·1.5 (H_2O). Hydrogen atoms on the linkers and clathrated water molecules omitted for clarity. Atom color code: grey, C; red, O; blue, N; yellow, S; cyan, Cu. Adapted from ref.[45].

The most recent research activity in this field focuses on the preparation of a bridging dicarboxylate spacer containing a conjugated bithiazole core, namely: 2,2'-bithiazole-5,5'-dicarboxylic acid (H_2TzTz, Table 2). This spacer ideally comes from a "doubling" of thiazole-5-carboxylic acid through its self-coupling on the 2-position (the most reactive of the thiazolic ring). After linker synthesis optimization, the as-prepared H_2TzTz was reacted in DMF under solvothermal conditions with $ZrCl_4$ using HCl as crystal modulator, yielding a pale yellow powder of $[Zr_6O_4(OH)_4(TzTz)_6] \cdot n(DMF)$ (Fig. 7).[46] This MOF is isostructural with the members of the UiO-67 family[50] and with the bithiophene analogue prepared by Moon and co-workers in 2015.[51] Hence, it is of cubic crystallographic symmetry, and the [Zr_6] octahedral node is surrounded by twelve carboxylate groups generating a 3D microporous structure. Each zirconium(IV) ion is eight-coordinated in a square-antiprismatic coordination geometry defined by eight oxygen atoms. The 3D network contains two types of cages: one octahedral and another tetrahedral in shape.

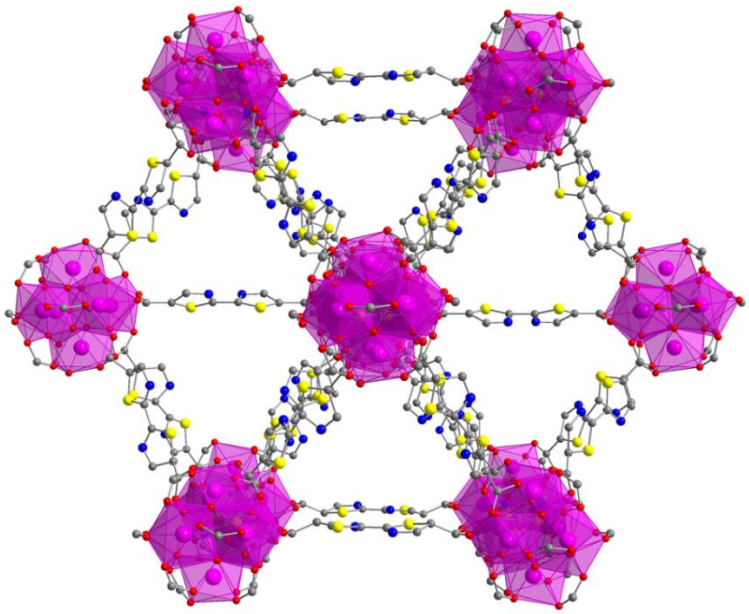

Fig. 7. Portion of the crystal structure of $[Zr_6O_4(OH)_4(TzTz)_6] \cdot n(DMF)$, viewed in perspective along the *c* crystallographic direction. Atom color code: grey, C; red, O; blue, N; yellow, S; violet, Zr. Solvent molecules and hydrogen atoms omitted for clarity. Adapted from ref.[46].

The synthetic methodology called SALI (Solvent Assisted Linker Incorporation) to get functionalized derivatives of already known stable and mesoporous zirconium MOFs has been exploited for the preparation of thiazole-decorated samples. A tailor-made benzothiazolium bromide salt functionality [(HBzTz)Br, Table 2] was introduced *via* SALI into the mesoporous Zr-based metal–organic framework NU-1000 $[Zr_6O_4(OH)_8(H_2O)_4(TBAPy)_2]$, where $TBAPy^{4-}$ = 1,3,6,8-tetrakis(p-benzoic-acid)pyrene. The resulting NU-1000-BzTz MOF $[Zr_6O_4(OH)_{6.3}(H_2O)_4(TBAPy)_2]$ ·1.7(BzTz)Br shows a maximum loading of 1.7 molecules of benzothiazolium extra-linkers per $[Zr_6]$ node, as inferred from the ^1H NMR peaks relative integration coming from samples digested in D_2SO_4/D_2O/DMSO-*d*$_6$. The material remains crystalline and with identical reticular topology after the inclusion process.[47]

1.3 Polymeric formates (Firenze)

The very first stages of MOF research in Firenze were focused on the preparation of polymeric formates. Formic acid (HCOOH) is the simplest and smallest organic carboxylic acid conceivable. A

boost on the study of polymeric metal formates has been given by the discovery of a wide variety of crystalline phases that can be obtained with this linker, along with the large number of applicative fields where these materials can be exploited, spanning from gas storage to luminescence and magnetism. The formate molecule is very small and possesses a strong coordinating ability, thus tending to form high-density phases. Most of the polymeric formates known show an ABX_3 "perovskite-like" structure, with A = organic cation, B = M^{II} in an octahedral coordination geometry (M = Mn, Co, Ni, Zn, Mg), X = μ-$HCOO^-$. The organic cation (usually in the form of an ammonium salt) sits within the cubic pores of the anionic 3D framework. The final crystallographic lattice symmetry (and related space group) is variable, and it depends on shape, size and charge factors. In 2008, the Firenze team published the preparation and solid-state characterization of the new Mg^{II} formate $[(CH_3)_2NH_2][Mg(\mu\text{-}HCOO)_3]$ isomorphous to the (already known) Mn^{II}, Co^{II}, Ni^{II} and Zn^{II} analogues.[52] High-quality single crystals were grown under solvothermal conditions in DMF. The structure consists of a rhombohedral polymeric network (space group $R\bar{3}c$) with channels of cubic section in which the vertices are occupied by six-coordinated Mg^{II} ions. The formate molecule bridges adjacent metal centers in an *anti-anti* coordination mode. The cubic cavities are occupied by dimethylamine molecules, deriving from thermal decomposition of the DMF solvent (Fig. 8). The location of the proton that neutralizes the overall charge is unknown. Therefore, the MOF can be formulated either as $[(CH_3)_2NH_2][Mg(\mu\text{-}HCOO)_3]$ or as $Mg(HCOO)_2(HCOOH) \supset (CH_3)_2NH$. Nevertheless, the possibility to remove the amine after thermal activation and measurement of a BET surface area of 448 m^2/g[53] leads to a preference for the latter formulation.

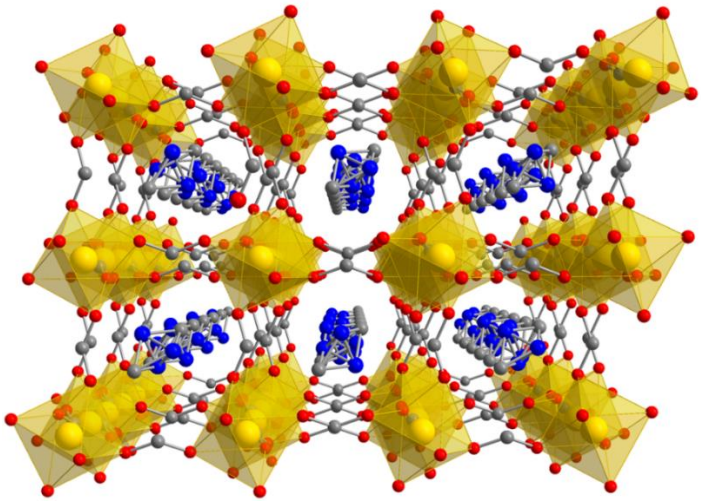

Fig. 8. Portion of the crystal structure of $[(CH_3)_2NH_2][Mg(\mu\text{-}HCOO)_3]$: view of the cubic cavities with Mg atoms at the corners, containing (disordered) dimethylamine molecules [view orthogonal to the (011) Miller planes]. Atom color code: orange, Mg; gray, C; red, O; blue, N. Hydrogen atoms omitted for clarity. Adapted from ref.[52].

In our attempts to prepare Mg^{II}-based MOFs with different organic acids, the solvothermal reaction between magnesium perchlorate hydrate and the ditopic cyclobutane-1,1'-dicarboxylic acid in formamide led to the unexpected formation of the polymeric formate $(Fmd)Mg(HCOO)_3$, where Fmd^+ = formamidinium cation, $[HC(NH_2)_2]^+$. In this synthesis, cyclobutane-1,1'-dicarboxylic acid does not form any MOF; its role is merely that of a medium-strength acid that catalyzes condensation between ammonia (deriving from the thermal decomposition of the solvent) and one molecule of formamide to generate *in situ* the formamidinium cation. The latter is eventually included into the final crystalline product. When an ‘‘auxiliary’’ templating cation is introduced in solution as its carbonate salt, the same reaction leads to a different formate: $(Gua)Mg(HCOO)_3$, with Gua^+ = guanidinium, $[C(NH_2)_3]^+$. The two phases are isostructural and belong to the same cubic network topology found for $[(CH_3)_2NH_2][Mg(\mu\text{-}HCOO)_3]$ and for the ABX_3 “perovskite-like” polymeric M^{II} formates of the literature. The formamidinium and guanidinium formates have been extensively characterized through solid-state multinuclear (^1H, ^{13}C and ^{15}N) NMR spectroscopy.[54] The simultaneous presence of many hydrogen bonds gives these materials a significant thermal and chemical stability.

A slight variation on the theme was achieved through the employment of lanthanide salts under the same experimental conditions. When Ln^{III} metal salts are chosen as starting reagents under the same experimental conditions, the analogous species of general formula (Fmd)Ln^{III}(μ-HCOO)$_4$ (Ln = Eu, Gd, Tb, Dy) could be prepared, where the central rare Earth can expand its coordination number to eight, because of its larger ionic radius.[55] The new coordination geometry is square antiprismatic, with eight bridging formates surrounding the metal nodes (Fig. 9a). The as-obtained four MOFs are isostructural; they are featured by an orthorhombic (chiral) $C222_1$ space group. Chirality stems from the peculiar spacial arrangement of the bridging formates that creates regularly alternated left-handed and right-handed helices in the lattice (Fig. 9b).

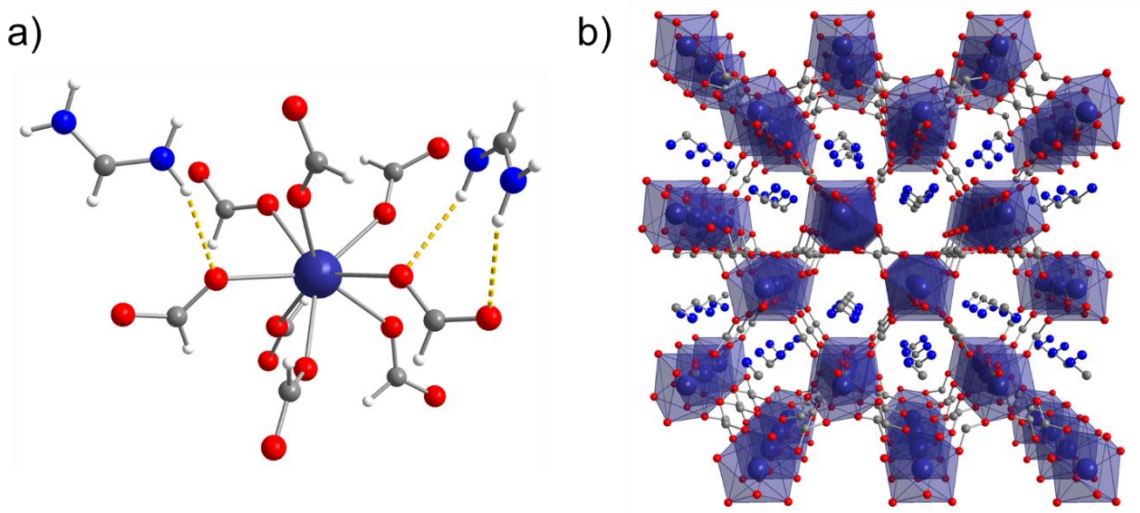

Fig. 9. (a) Asymmetric unit of the crystal structure of (Fmd)Dy(HCOO)$_4$ and (b) view of the 1D channels along the *a* axis. In (b), hydrogen atoms omitted for clarity. Atom color code: navy blue, Dy; gray, C; white, H; red, O; blue, N. Hydrogen bonds depicted in yellow dotted lines. Adapted from ref.[55].

1.4 Phosphonate-based MOFs (Perugia)

The first examples of crystalline open framework metal phosphonates were published in the 1990s[56-58] by the research group based in Perugia, led by Alberti, after a multidecennal research experience in this field.[59] In particular, zirconium phosphonates gained a relevant interest due to their remarkable stability, when compared to carboxylate-based MOFs, and to a high structural

flexibility generated by the wide coordination capabilities of phosphonate tetrahedra. In some cases, these early studies anticipated some recent leading concepts such as the "breathing effect" shown by flexible MOFs during adsorption-desorption processes,[60] first reported in 2005 by Kitagawa and co-workers.[61] Starting from 2002, the use of aminomethylenephosphonate building blocks has opened new perspectives for the preparation of materials with controlled porosity because of their considerably simpler preparation than that of similar all-carbon phosphonates. A plethora of different structural motifs were obtained, due to the presence of polar amino groups that induce the formation of non-covalent interactions as structure-directing factors.[62-67] The phosphonic acid linkers and related MOFs discussed in this review are collected in Table 3, for the sake of clarity.

Table 3. List of the phosphonate-based linkers and the corresponding MOFs reported in this section, along with the corresponding BET specific surface areas (SSAs) and decomposition temperature. n.p. = non porous.

Linker	Compound	BET SSA (m^2/g)	T_{dec} (° C)	Ref.
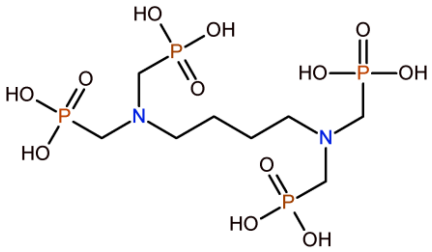 $H_8C_4P_4$	$Zr(H_4C_4P_4)$	n.p.	280	[68]
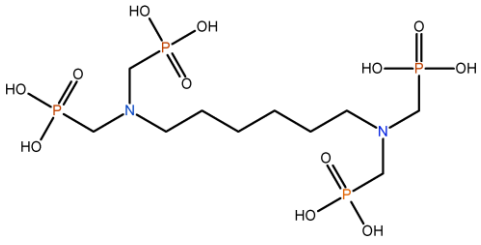 $H_8C_6P_4$	$Cu_3(H_2C_6P_4)(bipy)_2$ $Cu_3(H_2C_6P_4)(PyEtPy)_2$	n.p. n.p.	250 200	[69]
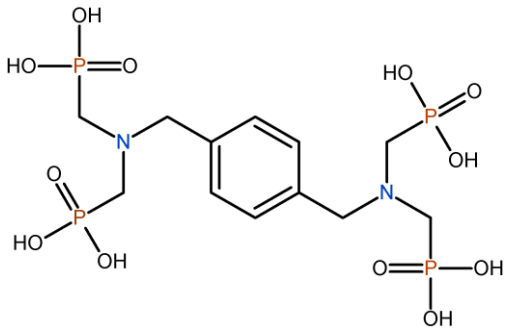	$Cu_3(H_2pxylP_4)(PyEtPy)_2$	n.p.	250	[69]

H_8pxylP_4				
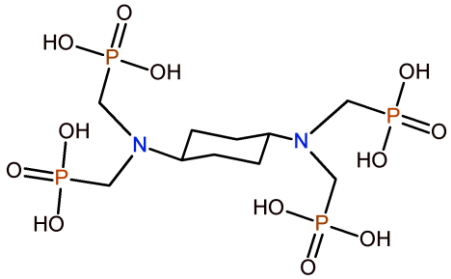 H_8CyP_4	$Zr(H_4CyP_4)$	n.p.	300	[68],[70]
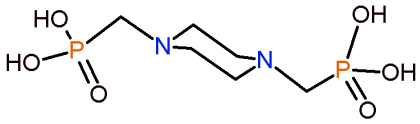 H_4pip	$Zr_2H_4(pip)_3$	n.p	310	[71]
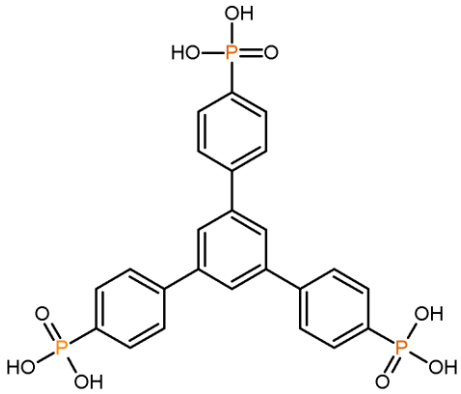 H_6btbp	$Zr_3(H_3btbp)_2$	n.p.	400	[72]
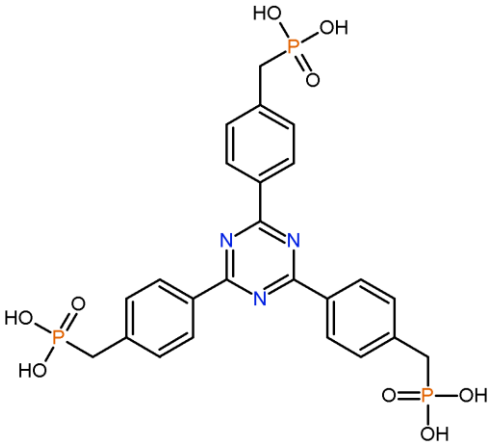 H_6*p*ttbmp	$Zr(H_4$*p*ttbmp$)_2$	410	450	[73]

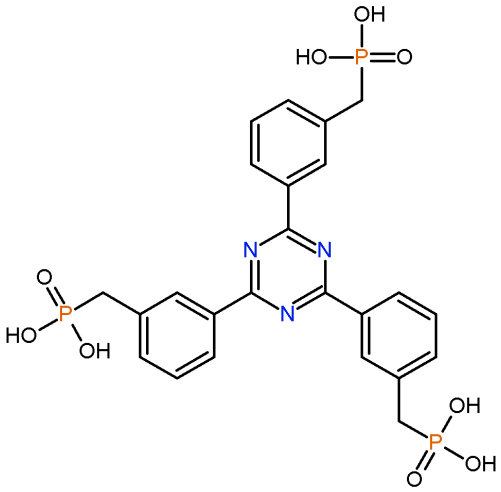 H$_6$*m*ttbmp	Zr(H$_4$*m*ttbmp)$_2$	n.p.	480 [74]

The constant development of experimental and numerical methods for crystal structure determination from powder diffraction data has been crucial for studying these materials, typically obtained as microcrystalline powders with extremely low solubility. Relevant results were obtained with the use of the branched R-diamino-*N*,*N*,*N*′*N*′-tetramethylenephosphonic acids. Fig. 10 schematically shows the crystal structure of two different compounds, in which R is either a butyl or a cyclohexyl residue. In spite of the similarity of the tetraphosphonate building blocks, their crystal structures are very different.[68]

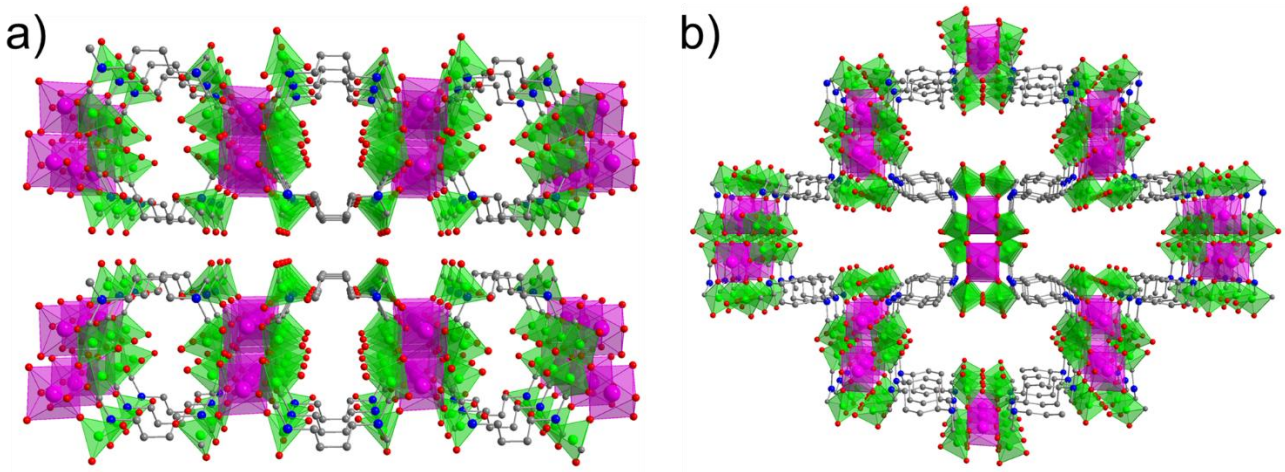

Fig.10. Representation of the crystal structure of (a) zirconium(IV) butyldiamino-*N*,*N*,*N*′,*N*′-tetra(methylenephosphonate) and (b) zirconium cyclohexyldiamino-*N*,*N*,*N*′,*N*′-tetra(methylenephosphonate). ZrO_6 octahedra are violet and PO_3C tetrahedra are green. Atom color code: grey, C; red, O; blue, N; green, P; violet, Zr. Adapted from ref. [68].

The butyldiamino derivative $Zr(HPO_3CH_2)_2N\text{-}C_4H_8\text{-}N(CH_2PO_3H)_2{\cdot}4H_2O$ is layered, with complex layers containing channels running inside them where water molecules are placed (Fig. 10a). Each layer is built up by the bridging of 1D inorganic building units (IBUs) through the butyldiamino group. The cyclohexylamino derivative $Zr(PO_3CH_2)_2N\text{-}C_6H_{10}\text{-}N(CH_2PO_3)_2Na_2H_2{\cdot}5H_2O$ shows a true 3D open framework in which IBUs (with the same connectivity as in the former compound) are connected by the cycloalkyl groups (Fig. 10b). Another promising system is the Zr piperazine-*N*,*N'*-bis(methylphosphonate) $Zr_2H_4[(O_3PCH_2)_2N_2C_4H_8]_3{\cdot}9H_2O$.[71] In this case, the two phosphonate tetrahedra are placed at opposite sides of the building block. Typically, zirconium derivatives containing all-carbon diphosphonates with such geometry have a pillared structure based on layers analogous to those found in α-Zr phosphonates. In this case, a 3D structure is obtained, in which the piperazine moieties act as spacers for inorganic chains in a trigonal arrangement, creating channels filled with water molecules (Fig. 11).

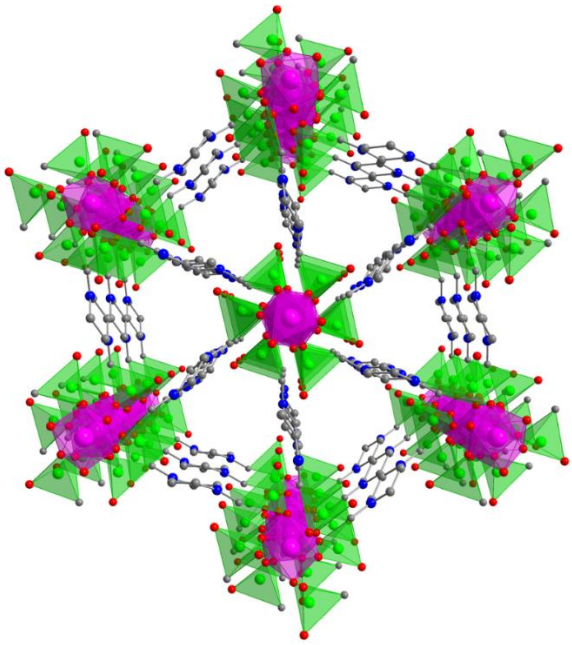

Fig. 11. Representation of the crystal structure of Zr piperazine-*N*,*N'*-bis(methylphosphonate). Water molecules in the channels omitted for clarity. Atom color code: grey, C; red, O; blue, N; green, P; violet, Zr. Adapted from ref.[71].

The three compounds described above did not show relevant N_2 adsorption at 77 K, but water molecules can be reversibly adsorbed and desorbed, indicating that the pores are indeed accessible to guest species. These structures potentially represent archetypes for the preparation of families of isoreticular compounds in which the channel size can be tuned by changing the organic spacer between the phosphonate tetrahedra. The main challenge rests in the synthesis of the organic linkers, which requires starting materials that are not commercially available. Research on this topic is in progress. More recently, a strategy based on the use of rigid, non-linear polytopic phosphonic linkers was adopted, based on the assumption that these spacers should avoid the formation of dense inorganic layers and direct the assembly of the crystal structure towards open frameworks. The first attempt in this direction was made combining Zr^{IV} with the linker 1,3,5-tris(4-phosphonophenyl)benzene (H_6btbp, Table 3),[72] which had already proved to be a promising building block in combination with other metals, such as vanadium and strontium.[75, 76] The resulting compound $Zr_3(H_3btbp)_4 \cdot 15H_2O$ (Zrbtbp) features a honeycomb motif based on trinuclear IBUs connected in two dimensions by the organic linkers, giving rise to cavities of about 10 Å diameter (Fig. 12).[72]

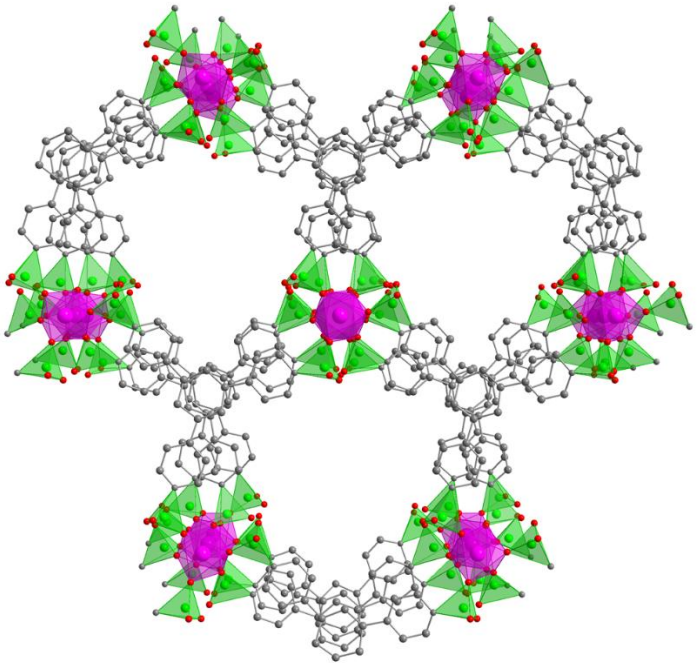

Fig. 12. Portion of the crystal structure of Zrbtbp. Atom color code: grey, C; red, O; green, P; violet, Zr. Adapted from ref. [72].

Despite the relatively large amount of water molecules present in the framework of the as-synthesized Zrbtbp, no porosity to either N_2 at 77 K or CO_2 at 195 K was observed upon activation. This was ascribed to the unfavorable stacking of layers in the dehydrated structure, where access to the pores by N_2 and CO_2 is likely prevented by the IBUs of adjacent layers, which lie above and below the apertures. Notably, water can diffuse in and out of the framework, possibly because of its ability to form hydrogen bonds with the abundant free P-OH groups. Stability tests demonstrated that Zrbtbp has thermal and chemical stability comparable to the benchmark Zr-carboxylate MOF UiO-66.[50] In the same year, the similar linker 2,4,6-tris(4-(phosphonomethyl)phenyl)-1,3,5-triazine (H_6*p*ttbmp, Table 3) possessing higher flexibility than H_6btbp owing to its methylene connectors placed between the phosphonic groups and the aromatic rings was employed to synthesize the crystalline and microporous compound named UPG-1: Zr(H_4*p*ttbmp)$_2$·10H_2O (Fig. 13). [73]

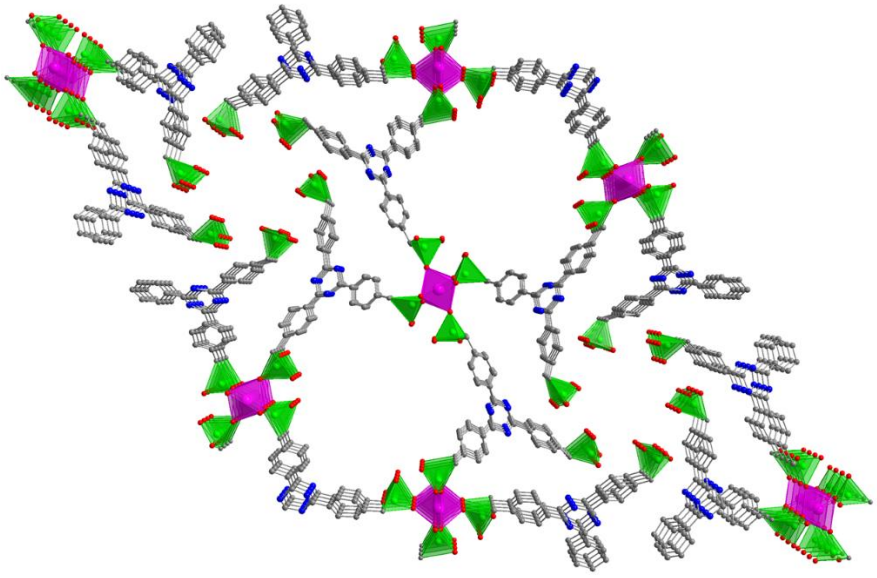

Fig. 13. Portion of the crystal structure of Zr(H_4*p*ttbmp)$_2$. Atom color code: grey, C; red, O; blue, N; green, P; violet, Zr.Adapted from ref. [73].

The structure of UPG-1 is based on one-dimensional IBUs constituted of ZrO_6 octahedra linked by exobidentate PO_3C groups and connected through the organic linkers. This connectivity gives rise to a three-dimensional framework featuring two sets of channels with diameters of about 5 and 10 Å, respectively. Removal of water molecules does not induce relevant structural rearrangements, with the result that UPG-1 is permanently porous to CO_2 and CH_4 at 195 K and to *n*-butane at 273 K, whilst it displays no appreciable uptake of N_2 at 77 K. The BET specific surface area estimated from the CO_2 adsorption isotherm at 195 K is 410 m^2/g, with a pore volume of 0.2 cm^3/g. The thermal stability of UPG-1 was found to be comparable to that of UiO-66, while its stability to hydrolysis in harsh conditions (200 °C in water for two days, 120 °C in 0.1 M HCl for three days) is superior to that of UiO-66. Subsequent to the discovery of UPG-1, the isomeric linker 2,4,6-tris[3-(phosphonomethyl)phenyl]-1,3,5-triazine (H_6*m*ttbmp) was prepared with the aim of studying the variation in the 3D assembly caused by the linker's positional isomerism.[74] Combination of H_6*m*ttbmp with Zr^{IV} precursors afforded the layered, non-porous compound $Zr(H_4$*m*ttbmp$)_2 \cdot 3H_2O$ (UPG-2), displaying a structural arrangement completely different from that of UPG-1, in spite of the nearly identical chemical composition. In UPG-2, isolated zirconium(IV) ions in octahedral geometry are connected by the organic linkers to form 2D sheets. In an effort to expand this chemistry beyond zirconium, copper phosphonates were also investigated to introduce additional coordination possibilities, relying on the affinity of this metal for nitrogen-based linkers. Early attempts using tetraphosphonates derived from hexamethylene- and xylylenediamines led to layered structures where the Cu^{II} centers are coordinated in a square pyramidal fashion and three basal positions are occupied by one nitrogen and two phosphonic oxygen atoms belonging to the same linker.[77] Later on, the role of bipy (4,4'-bipyridyl) as an ancillary ligand in the presence of *meta*- and *para*-xylylenediphosphonic linkers was investigated, finding that it could dominate the assembly of the crystal structure by (i) bridging copper ions and favoring the formation of one-dimensional chains that are connected in the second dimension by the phosphonate linkers; (ii) establishing π-π stacking interactions with the aromatic rings of the phosphonate linkers.[78] As a result, the two coordination

polymers derived from the *meta* and *para* linker isomers display the same chemical composition, *i.e.* $Cu[(HO_3PCH_2)_2C_6H_4][bipy]\cdot 2H_2O$, and remarkably similar layered crystal structures. In 2013, the reaction between tetraphosphonic 1,4-xylylene or hexamethylenediamines (H_8L^1 and H_8L^2, respectively) and bipy or its analogue PyEtPy [1,2-bis(4-pyridyl)ethane] successfully produced a family of three isoreticular Cu-based MOFs of general formula $Cu_3(H_2L^1)(bipy)_2\cdot 9H_2O$, $Cu_3(H_2L^2)(bipy)_2\cdot 11H_2O$ and $Cu_3(H_2L^2)(PyEtPy)_2\cdot 24H_2O$ (Fig. 14).[69] These compounds feature the same trinuclear IBU, and their flexible frameworks contain large 1D channels that can reversibly adsorb and desorb large amounts of water, displaying volume changes up to 26%. The three MOFs are non-porous towards N_2 at 77 K, but they do adsorb CO_2 at 195 K, displaying an hysteretic behavior that can be ascribed to their flexible structure. Despite the relatively low CO_2 uptake, the very low affinity for N_2 makes these MOFs potentially useful for application in CO_2 capture, as suggested by a recent comprehensive computational screening of the CoRE MOF 2014 DDECe database searching for promising candidates for this application.[79]

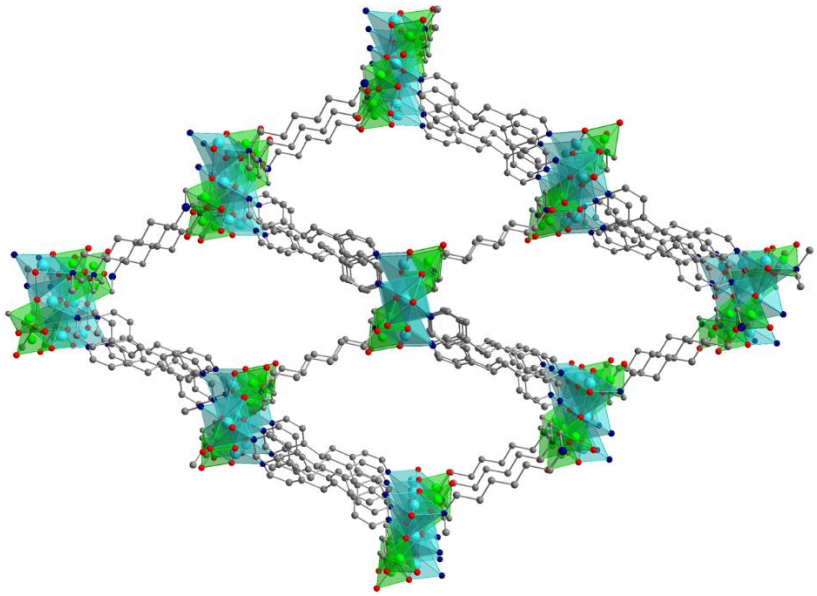

Fig. 14. Portion of the crystal structure of $Cu_3(H_2L^2)(PyEtPy)_2\cdot 24H_2O$. Water molecules in the channels and hydrogen atoms on the linkers omitted for clarity. Atom color code: grey, C; red, O; blue, N; green, P; cyan, Cu. Adapted from ref.[69].

1.5 Ce-based MOFs (Torino, Perugia, Pisa)

The chemistry of Ce^{IV} MOFs started to gain remarkable attention half a decade later than that of their Zr^{IV} analogues. Cerium is a promising candidate for the preparation of stable MOFs at relatively limited cost. With an average abundance of over 60 ppm in the Earth crust, which is much higher than that of the other rare earth (RE) elements, it is the most accessible RE element.[80] Its oxide (CeO_2, ceria) finds applications in photocatalysis and redox chemistry, being a well-known catalyst for oxidation (mainly combustion) and reduction reactions.[81] Cerium cations, stable in both +3 and +4 oxidation states (a peculiarity among REs), can easily switch between them and thus be active in redox catalysis. Analogously, cerium in MOFs can be found in both oxidation states. The following general considerations can be drawn from the literature: (i) both Ce^{III} and Ce^{IV} MOFs are stable and can be prepared with a careful selection of the synthetic procedure (mainly the metal precursor choice, secondarily the reaction conditions); (ii) synthetic conditions employed for the obtainment of Ce^{III} MOFs tend to be harsher (higher temperature or/and longer time) than those necessary to get Ce^{IV} MOFs; (iii) sometimes, a reduction of the Ce^{IV} precursors to give Ce^{III} products occurs during the synthesis, while the opposite has never been observed; (iv) Ce^{III}-containing materials are featured by peculiar crystal structures, while Ce^{IV}-based MOFs are normally isostructural with other M^{IV}-containing analogues (*e.g.* Zr^{IV} or Hf^{IV} in UiO-66); (v) the thermal stability of Ce^{IV}-MOFs is generally lower than that of the other M^{IV} counterparts. Eight-coordinated Ce^{IV} displays a slightly larger ionic radius compared to that of Zr^{IV} in coordination number eight (1.1 *vs.* 0.98 for Ce^{IV} and Zr^{IV} respectively, according to Shannon).[82] Owing to these similarities, the hexanuclear oxo/hydroxo Ce^{IV} clusters of formula $[Ce_6O_4(OH)_4]^{12+}$ and isostructural to the zirconium(IV) ones are able to afford Ce-MOFs with the same topologies as their Zr counterparts. The first Ce^{IV} MOFs based on dicarboxylic linkers were reported in 2015 by Lammert and co-authors. The synthesis was carried out in DMF, obtaining isoreticular UiO-66 type Ce-MOFs by using different linear dicarboxylic linkers, namely benzenedicarboxylic, fumaric, naphtalenedicarboxylic and biphenyldicarboxylic acids (H_2BDC, H_2FUM, H_2NDC and H_2BPDC, respectively). Later on, the same group extended the

chemistry of Ce^{IV}-MOFs also to other topologies found in the Zr^{IV} analogues.[83, 84] The activity of the Italian groups in this field is mainly coming from the Torino team of Bordiga and co-workers and by the Perugia group of Costantino and collaborators, whose first contributions concerning the synthesis and the characterization of Ce-based MOFs dates back to 2016. In that year, the Torino group published a work reporting the solvothermal synthesis of a Ce^{III} MOF using a simple one-pot method based on reacting Ce^{III} nitrate and 1,3,5-benzenetricarboxylic acid (H_3BTC) to yield up to 1 g of product.[85] The microcrystalline MOF powder was studied by means of powder X-ray diffraction (PXRD) and X-ray absorption spectroscopy (XAS, also exploiting *in-situ* conditions), analyzing the PXRD data with the so-called Rietveld method and the XAS data with the multiple-scattering EXAFS method. The combined results confirmed that the compound with minimal formula $Ce(BTC)(H_2O)_n$ is isostructural with MOF-76[86] and was therefore labeled as MOF-76-Ce (Fig. 15a).

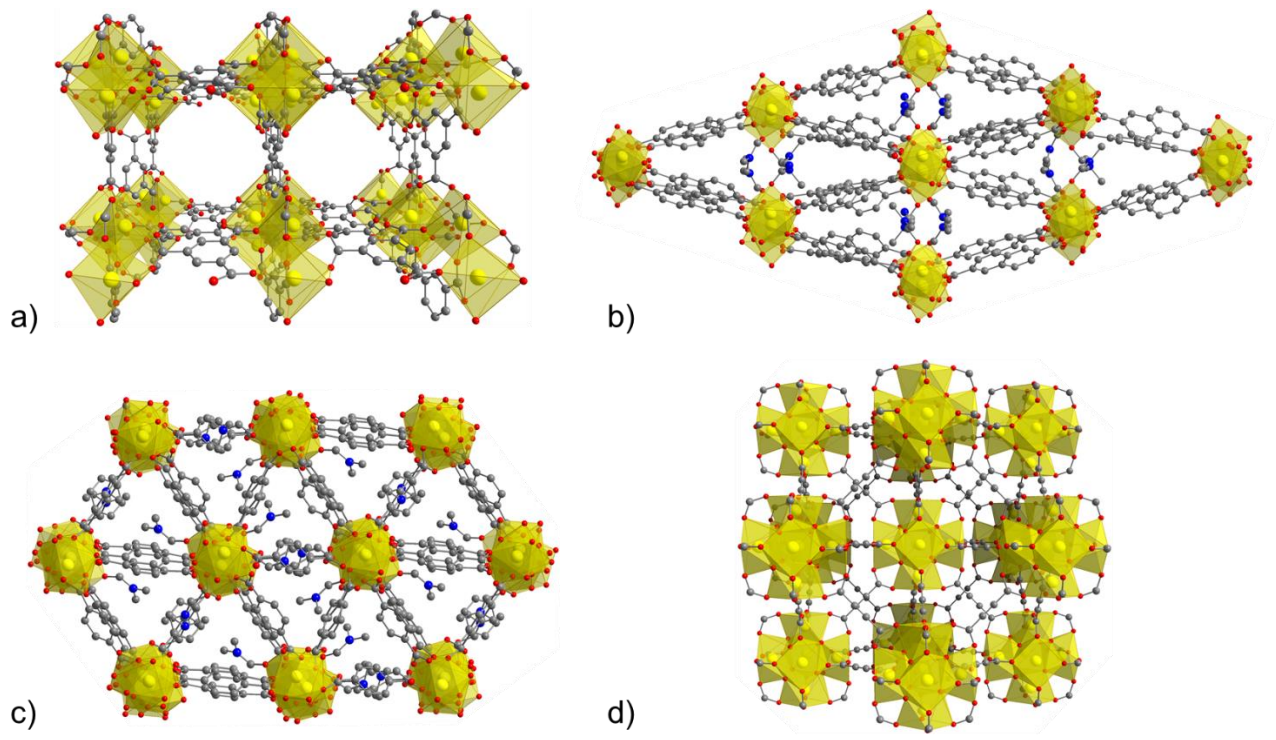

Fig. 15. Representations of the crystal structure of: (a) MOF-76-Ce; (b) $Ce_2(NDC)_3(DMF)_4$; (c) $Ce_5(BDC)_{7.5}(DMF)_4$ and (d) Ce-UiO-66-ADC. Hydrogen atoms on the linkers and clathrated solvent molecules omitted for clarity. Atom color code: yellow, Ce; gray, C; red, O; blue, N. Adapted from refs.[85], [87], [88] and [89].

The thermal stability study of MOF-76-Ce revealed that the material is stable up to 550 °C; three different stable crystalline phases form during heating, corresponding to different solvation extents with a solvent:Ce ratio of 1:1, 1:2 and 0, respectively. Ce cations have a +3 oxidation state as confirmed by XANES and *in-situ* FTIR spectroscopies, while the latter also revealed the presence of an open metal site accessible for CO as a probe. Another Ce-based material reported by the Torino group in 2019[87] was synthesized from Ce^{III} nitrate and the ditopic linker 2,6-naphthalenedicarboxylic acid (H_2NDC) under solvothermal conditions at 160 °C in DMF for three days. The search for the optimal synthetic conditions was made employing high-throughput methods, where a vast number of different syntheses are performed at small scale systematically modifying the reaction conditions.[90] The product prepared in high purity and yield was characterized by means of single-crystal XRD, which allowed the determination of its crystal structure and minimal formula $Ce_2(NDC)_3(DMF)_4$ (Fig. 15b). The Ce^{III} ions have a distorted pentagonal bipyramidal coordination geometry, with six oxygen atoms coming from the carboxylate groups and one oxygen atom belonging to a DMF molecule. Each cerium center shares three carboxylate linkers with the neighboring cations forming extended chains parallel to the diamond-shaped channels. Upon thermal activation, the material loses all the DMF molecules yielding $Ce_2(NDC)_3$. Unfortunately, a severe structural disorder precluded the structure determination from single-crystal X-ray diffraction data alone. The structure was successfully solved by combining the X-ray diffraction results with the information coming from Ce K-edge X-ray absorption spectroscopy. In the fully desolvated phase, disordered channels with triangular section (instead of the diamond-shaped ones) and linkers with fractional occupancy numbers were found. XAS also confirmed the +3 oxidation state of cerium in both phases. The adsorption properties of $Ce_2(NDC)_3$ were studied by means of volumetric adsorption measurements of N_2 at -196°C and CO_2 at -78°C. The material is only porous to carbon dioxide, yielding a specific surface area of about 200 m^2/g. The synthesis of the new Ce^{III} derivative $Ce_5(BDC)_{7.5}(DMF)_4$ containing terephthalic acid was reported by the same group in 2020 using a

very similar recipe: solvothermal conditions and Ce^{III} nitrate as precursor.[88] The crystal structure (previously solved by D'Arras *et al.* [91]) is rather complex, with five different cerium atoms in the asymmetric unit (Fig. 15c). It also presents triangular pores (occupied by DMF molecules) and Ce-O-Ce chains. The study from the Torino group focused, in particular, on the properties of the desolvated phase (after a vacuum heat treatment at 250 °C): a modest specific surface area could be estimated by N_2 adsorption experiments (about 220 m^2/g) but the structural disorder precluded any crystallographic analysis. The successful DMF removal after the thermal treatment was confirmed by FTIR experiments and low-temperature dosage of CO as a probe molecule that showed the accessibility of Ce^{III} open metal sites, whose oxidation state was further confirmed by XAS measurements. Finally, the most recent paper published by the same group in 2020 dealing with Ce-MOFs reports the synthesis and the characterization of Ce-UiO-66-ADC (Fig. 15d), based on Ce^{IV} ions and acetylenedicarboxylic acid (H_2ADC) as linker.[89] This ditopic acid has been used very rarely in MOF literature because of its extreme thermal lability that limits its exploitation for MOFs solvothermal syntheses. As Ce^{IV} MOFs are characterized by milder and faster synthetic conditions than those of their Ce^{III} counterparts, a careful optimization of the synthetic procedure led to the obtainment of a crystalline product, though with low yields (5% or 30% in the absence or in the presence of triethylamine in the synthetic mixture, respectively). The material showed a good powder X-ray diffraction pattern, which allowed the crystal structure of Ce-UiO-66-ADC to be easily refined through the Rietveld method using the crystal structure of its zirconium analogue UiO-66. Thermogravimetric analysis (TGA) and variable-temperature powder X-ray diffraction (VT-PXRD) studies confirmed its poor thermal stability, with loss of crystallinity at temperatures as low as 90 °C.

The first contribution to the chemistry of Ce^{IV}-based MOFs from the Perugia group was published in 2019, when the synthesis of two Ce^{IV}-MOFs based on tetrafluorobenzenedicarboylic acid (H_2-F_4BDC) was reported.[92] In this paper, the synthesis was carried out in water by reacting the perfluorinated linker and cerium ammonium nitrate (CAN) at 110 °C under reflux. A UiO-66-type phase was obtained by using acetic acid as modulator [F4_UiO-66(Ce)]. The synthesis in water

without modulator afforded a new phase having the same topology of MIL-140, a Zr-MOF first reported by Guillerm *et al.* in 2012 [F4_MIL-140A(Ce)].[93] The two structures are shown in Fig. 16a and 16 b, respectively.

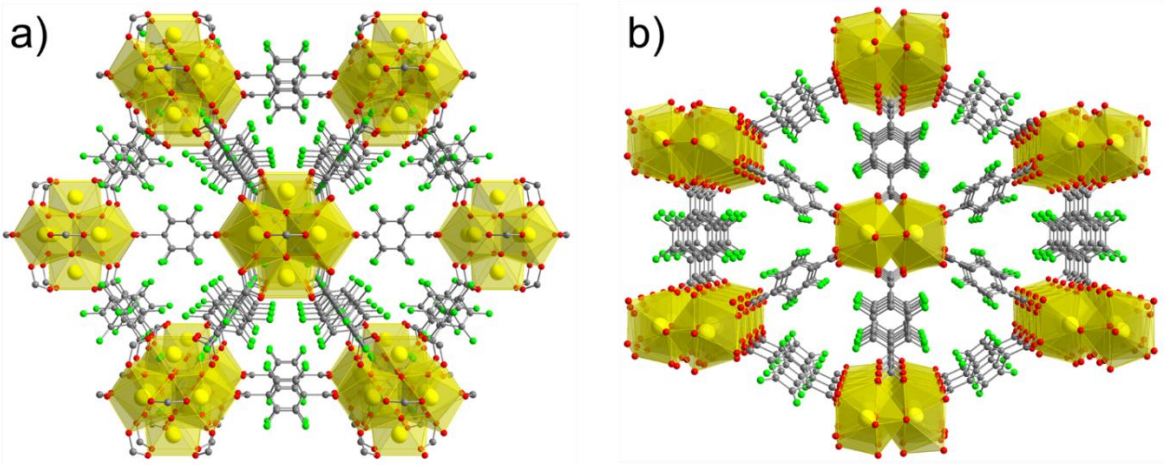

Fig. 16. Portion of the crystal structure of F4_UiO-66(Ce) (a) and F4_MIL-140A(Ce) (b). Atom color code: yellow, Ce; gray, C; red, O; light green, F. Adapted from ref.[92].

The F4_UiO-66(Ce) phase is isostructural with UiO-66. It was found that the tetrafluoro benzene rings are affected by a rotational disorder modelled into two average positions with 50% of occupancy. F4_MIL-140A(Ce) is constituted by 1D IBUs built from the connection of edge-sharing CeO_8 units, carboxylate groups and μ_3-oxide bridges. Notably, this compound is the first example of a Ce^{IV}-based MIL-140 type MOF. X-ray photoelectron spectroscopy (XPS) measurements revealed the presence of a certain amount of Ce^{III} in both samples. The content of Ce^{III} was determined by measuring the magnetic moment generated by the paramagnetism of Ce^{III} ions, confirming that in both phases it is lower than 10%. This fact suggests that Ce^{III} is mainly located over the MOF particles surface. The BET surface area for F4_UIO-66(Ce) is 641 m^2/g. It is quite lower than that found in the BDC-based UiO-66(Ce) (about 1100 m^2/g)[84] and in other monosubstituted-BDC UiO-66 phases previously reported (falling in the 727-1075 m^2/g range).[94] This fact could be attributed to the static rotational disorder and to the steric hindrance of the F_4BDC^{2-} linkers within the MOF structure. F4_MIL-140A(Ce) has a surface area of 320

m^2/g and a total pore volume of 0.11 cm^3/g, with a very narrow pore size distribution centered at 4.2 Å. Although the porosity is relatively low, this MOF has a very attractive potential for CO_2 capture. More recently, the Perugia team has reported on a new synthetic strategy for obtaining Ce^{IV}-MOFs with UiO-66 topology and their photocatalytic properties were investigated.[95] The MOFs were obtained with a quick and easy synthetic procedure by simply grinding the substituted dicarboxylic aromatic linkers and CAN in the presence of a small amount of concentrated acetic acid or nitric acid. The slurry was then heated up to 120 °C for 24 h in 2 mL vials and subsequently washed with DMF and water to remove the unreacted linkers. The crystallinity of the obtained compounds was found to be comparable to that of other MOFs synthesized via conventional hydrothermal routes. On the contrary, porosity was found to be lower, probably due to the presence of a certain amount of an amorphous phase.

2. Advanced characterization techniques applied to MOF materials

MOFs structural complexity requires a plethora of techniques for their thorough characterization. On this ground, the Italian groups in Torino and Como make extensive use of several spectroscopic and diffraction tools to get insight on the local MOF structure, spanning a wide wavelength range from infrared to X-ray. In addition, MOFs porous texture is studied through volumetric and calorimetric measurements. The former provide information on their accessible surface area and pore size distribution, while the latter measure the MOF thermodynamic affinity (isosteric heat of adsorption) for a specific gaseous or liquid guest. Fig. 17 provides a pictorial representation of the techniques used for MOFs characterization.

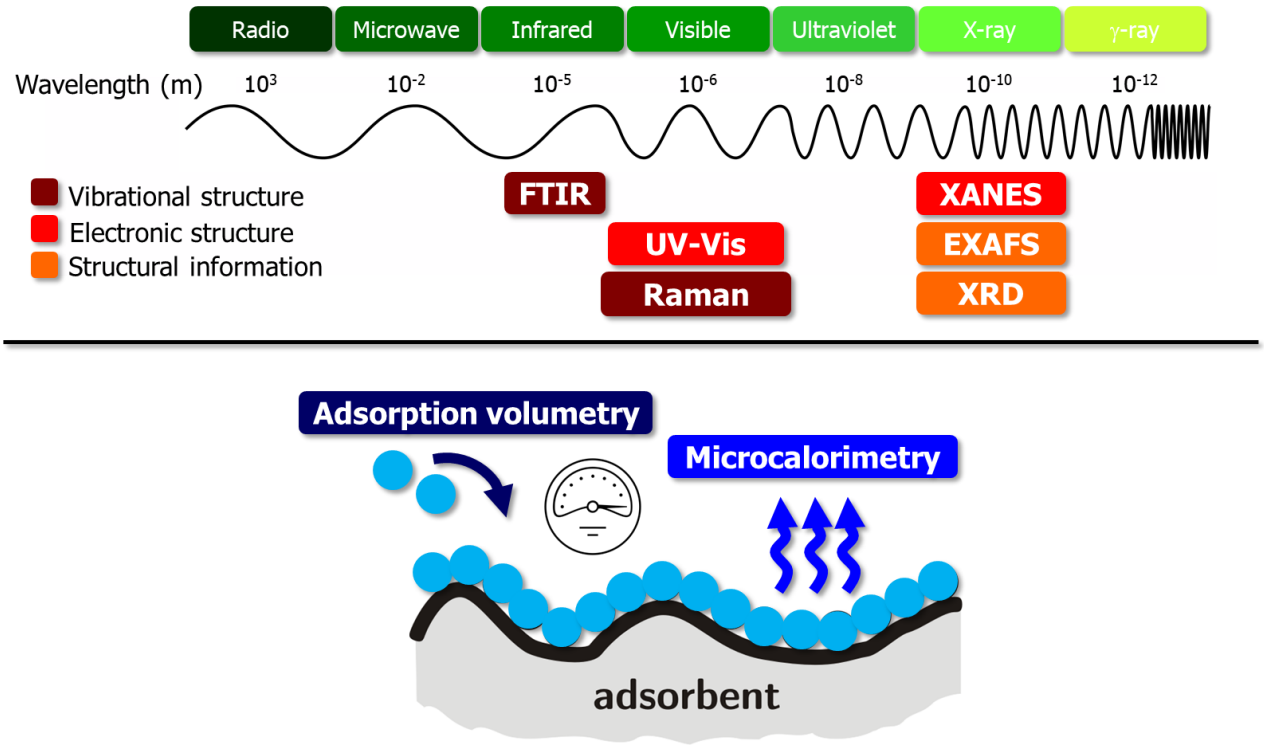

Fig. 17. Pictorial collective representation of the main characterization techniques exploited by the Torino and Como groups for their investigation of MOFs local structure and porosity.

2.1 Powder X-ray diffraction structural characterization at ambient and non-ambient conditions (Como)

The crystal and molecular structures disclosed by single-crystal X-ray or neutron diffraction are experimental datasets from which scientists can get information of paramount importance to rationalize the functional properties shown by crystalline matter in the solid state. Presently, single crystals remain the primary source of structural information on solids. Nonetheless, a large number of substances precipitate from the reaction medium as (microcrystalline) insoluble powders (as underlined in the previous sections), hampering the growth of single crystals and prompting their structural characterization through powder diffraction. An extended and systematic use of PXRD with ordinary laboratory instrumentation to determine the crystal and molecular structures of coordination polymers [with a specific focus on transition metal poly(azolates)] was jointly pioneered in the 1990s by Prof. Norberto Masciocchi and Prof. Angelo Sironi currently at the Università dell'Insubria

(Como) and Università di Milano, respectively.[96] As a matter of fact, all the bi- and tris(pyrazolate) coordination polymers reported in this review have been structurally characterized through PXRD, in a number of occasions without *a priori* knowledge of their structural features. PXRD at non-ambient conditions is a powerful tool that provides information on the chemico-physical properties of the system under investigation. As a complement to classical thermal analyses (TGA and Differential Scanning Calorimetry, DSC), *in situ* VT-PXRD experiments are normally carried out to assess (i) the thermal stability of the system in air (thermal analyses being conventionally carried out under inert atmosphere); (ii) the persistence of the pristine open framework (*vs*. phase transitions or structure collapse) during and after the clathrated solvent loss; (iii) the framework rigidity/flexibility when the external stimulus is the temperature variation. In the analysis of MOFs adsorption performance, *in situ* and *operando* PXRD experiments can be carried out while dosing the gas probe of interest varying both pressure and temperature. This can be realized in an ordinary research laboratory[97] or (more conveniently) at large scale facilities (where the intensity, brilliance and monochromaticity of the primary beam provides much better data and advanced experimental setup is available). As representative examples, we can quote $Fe_2(BPEB)_3$[98] and $Zn(BPZNO_2)$.[27] The structural features beyond the remarkable CO_2 adsorption of $Fe_2(BPEB)_3$ at mild conditions (40.5 wt. % CO_2 at 298 K and 10 bar) were investigated through combined experimental and computational methods. *In situ* and *operando* high-resolution and high-energy PXRD data collection at the beamline ID22 (European synchrotron radiation facility, ESRF) was carried out at 298 K, dosing CO_2 in the pressure range of 0-21 bar. Combining structure determination and refinement (on high-resolution data) with total scattering analysis (on high-energy data) unveiled the primary adsorption sites and the host-guest interactions in the assayed conditions. These studies were complemented by molecular dynamics simulations to confirm the guest molecules location. Prompted by theoretical calculation results[99] predicting that singly NO_2-functionalized MOFs should possess a CO_2 adsorption capacity higher than multi-functionalized (NO_2/NH_2, NO_2/Cl) MOFs (due to the higher local dipole moment shown by the nitro group when present as the sole linker tag), we investigated the CO_2 adsorption capacity

and affinity of the M(BPZNO$_2$) MOFs. At mild conditions (298 K and 1.2 bar), Zn(BPZNO$_2$) adsorbs 21.8 wt % CO_2. High-resolution PXRD at 298 K and different CO_2 loadings, adopted for the first time for an NO_2-tagged MOF, disclosed primary host-guest interactions involving the framework C_{pz}–NO_2 fragment and the CO_2 *oxygen* atoms, as further proved by Grand Canonical Monte Carlo calculations. This interaction is definitely distinct from that unveiled in NH_2-tagged MOFs,[100] where the CO_2 *carbon* atom is involved.

2.2 X-ray absorption spectroscopy (Torino)

X-ray absorption spectroscopy (XAS)[101] is an element-sensitive technique where the fine structure of the absorption spectra across a specific absorption edge (e.g. K, L or M) is measured to obtain information about the structure of matter. Traditionally, the XAS spectrum is divided in XANES and EXAFS, referring to the region across the very absorption edge and to the part at higher energies (hundreds of eV), respectively. XAS needs an intense and focused X-ray beam and, for this reason, it is usually practiced at large scale facilities, *e.g.* synchrotrons specialized in the delivery of synchrotron radiation for experiments. The analysis of the XAS spectra through the EXAFS technique allows to obtain information about the local disposition of the atoms that surround the absorber, thus providing information on coordination numbers, bond lengths and angles. This is of utmost importance in characterizing MOFs, as most of MOFs structural information comes from X-ray diffraction experiments that lack in characterizing *local* features challenging to be characterized like crystal defects, functionalization, changes in the local crystal symmetry. XAS is a powerful tool that provides a lot of information on this ground, owing to its element-selectivity (we can focus on the surroundings of the metal atom in MOFs) and its intrinsically local nature. The exploitation of XAS techniques in MOFs characterization was pioneered by the group of Prof. Carlo Lamberti from the University of Torino. Prof. Lamberti applied to MOFs most of the knowledge gained in studying other crystalline materials (like zeolites) in the past 15 years. As a case study, we report in the present

review two examples where XAS had a pivotal role in MOFs characterization: the Ni^{II} MOF $Ni_8(X)_6(tet)_6$ {X = OH^-, H_2O; H_2tet = (1*H*-pyrazol-4-yl)pyrrolo[3,4-f]isoindole-1,3,5,7(2H,6H)-tetrone}[102] (Fig. 18a) and the Ce^{III} MOF Ce(BTC)·n H_2O·m DMF (MOF-76-Ce)[85] (Fig. 18b).

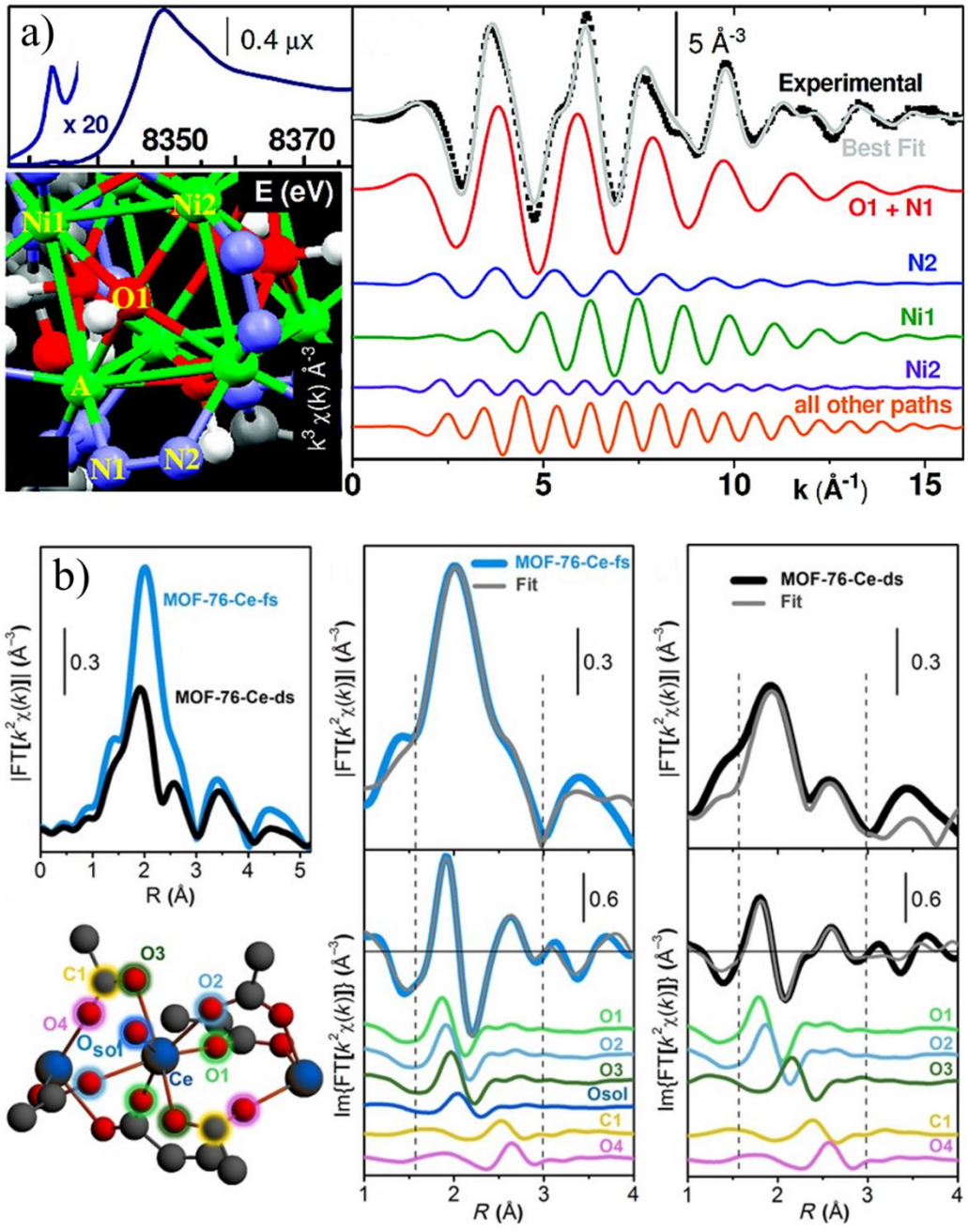

Fig. 18. (a) EXAFS analysis of $[Ni_8(\mu_4\text{-}X)_6(\mu_4\text{-}tet)_6]$; (b) EXAFS analysis of MOF-76-Ce. "ds" and "fs" stand for desolvated and fully solvated, respectively. Reprinted with permission from refs.[102] and [85], respectively. Copyright (2010) American Chemical Society; Copyright 2016 by John Wiley & Sons, Inc.

In the case of $Ni_8(X)_6(tet)_6$, EXAFS analysis in conjunction with Fourier transform infrared spectroscopy (FTIR) and PXRD unveiled the structure of the Ni-containing cluster and gave insight on the presence of water molecules. XANES data confirmed the presence of octahedral Ni^{II} cations and the absence of Ni^{III}, thus allowing to establish the OH^-/H_2O ratio in the metallic node (X-ray diffraction cannot distinguish the two groups because of the difficulty in hydrogen atoms location). MOF-76-Ce showed a quite complex behavior upon solvent removal: the material is synthesized in a DMF/H_2O mixture and both solvents are found trapped inside the pores of the fully solvated material. During the thermal treatment, water is firstly removed at milder conditions, causing a rearrangement of the crystal structure; successively, at higher temperatures DMF is also eliminated with another concomitant phase change. This behavior was highlighted by combined PXRD and EXAFS analyses: the first technique provided information about the long-range order, while EXAFS focused on Ce^{III} coordination sphere.

2.3 Vibrational (IR/Raman) and electronic (UV-Vis in absorption and emission) spectroscopies

2.3.1 Vibrational spectroscopy (Torino)

Vibrational spectroscopies [Fourier-Transform Infrared spectroscopy (FTIR) and Raman spectroscopy] are widely exploited techniques to reveal the structure and the reactivity of surface species present in MOFs.[103, 104] FTIR is very sensitive towards many different chemical groups showing a change in electric dipole associated with the vibrational motion. Raman spectroscopy is complementary to FTIR, being sensitive to apolar bonds vibrations. Both techniques are extremely powerful to answer a series of questions typical of MOFs solid-state science: (i) to check the presence/absence of solvents inside the pores; (ii) to clarify the linkers nature and identity; (iii) to assess the successful insertion of functional groups after post-synthetic procedures; (iv) to evidence

the presence of structural defects in the framework and coordination vacancies formed at the metal sites after desolvation through appropriate probe molecules. Probe-surface interactions can be observed by looking at the vibrational frequency perturbation and band intensity change of the probe molecule after interaction with the adsorption sites. In MOF materials, skeletal and surface vibrational fingerprints perturbation upon probe adsorption can be also investigated. This kind of information is crucial in understanding the role of MOFs active sites in many applications (like gas adsorption and separation or heterogeneous catalysis). As a representative example, *in situ* FTIR and Raman spectra were collected for Ce-UiO-66-ADC (ADC^{2-} = acetylenedicarboxylate).[89] Along thermal activation under high vacuum, the adsorbates were removed (Fig. 19a) and the MOF skeletal vibrational fingerprint appeared, as confirmed by the comparison with reference compounds (Fig. 19b). The FTIR analysis led to the final conclusion that a UiO-66-like derivative containing acetylene dicarboxylate as linker was successfully synthesized, even if this spacer is reactive and extremely thermolabile. However, the product of linker decarboxylation (propiolic acid) was also present in the MOF scaffold, generating defective sites that are frequently found in many members of the UiO family and analyzed through combined experimental and computational studies.

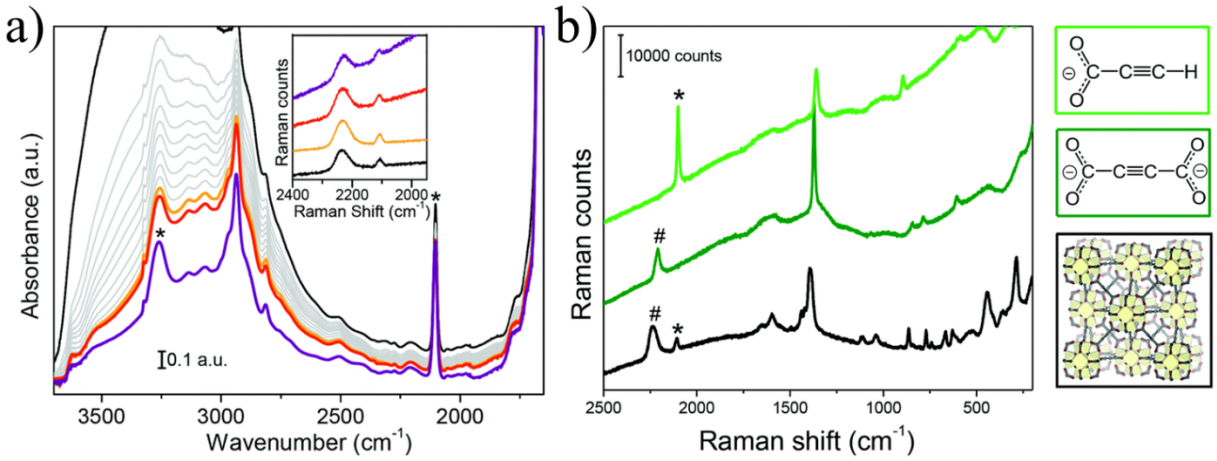

Fig. 19. (a) FTIR spectra collected during Ce-UiO-66-ADC thermal activation; inset: Raman spectra collected with λ_{inc} = 785 nm. Black: as synthesized RT; grey: in vacuum RT outgassing; yellow: 303 K; orange: 333 K; violet: 363 K. (b) Raman spectra (λ_{inc} = 785 nm) of Ce-UiO-66-ADC and reference compounds. Reproduced from ref.[89] with permission of The Royal Society of Chemistry.

As an example of investigation of MOFs open metal sites by means of probe molecules, we report the case of Ni(BDPB) [H_2BDPB = 4,4′-bis(1Hpyrazol-4-yl)biphenyl].[105] Dosing of CO at T = –213 °C (Fig. 20a) and H_2 at T = –259 °C (Fig. 20b) on a Ni(BDBP) activated sample revealed the absence of exposed metal sites. This finding is in line with the results obtained from a parallel gas adsorption study carried out on the same MOF.

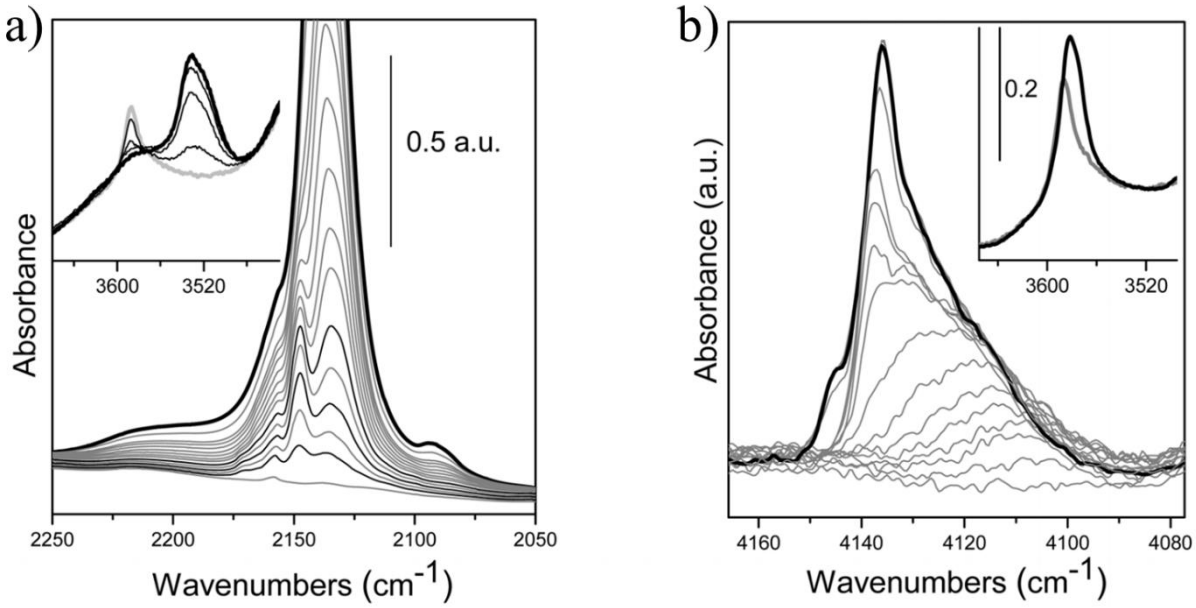

Fig. 20. FTIR spectra of selected probe molecules on a Ni(BDBP) activated sample: (a) CO at –213 °C and (b) H_2 at –259 °C. Dosages (black bold curves represent the maximum coverage) and successive degassing. Reproduced from ref.[105] with permission of The Royal Society of Chemistry.

2.3.2. Electronic spectroscopy (Torino)

UV-Visible spectroscopy in absorption and emission (photoluminescence) is one of the most common techniques to study the electronic transitions of molecules and materials. As for the absorption, it can be monitored and quantified by using both transmittance and reflectance mode (Diffuse Reflectance UV-Visible, DR-UV-Vis) depending on the sample form, if in solution or in powder, respectively. Reflectance modality is the normal choice for (powdery) MOF materials. In most of the UV-Visible

and photoluminescence studies, the attention is focused on the metal atoms (usually transition metals) present in the MOF framework. Any change around the metal atom (nature and number of coordinating linkers, coordination geometry) affects the material optical properties. Indeed, a variety of phenomena spanning from desolvation or probe molecule adsorption/desorption to more complex events such as linker or metal node exchange can be easily followed by means of UV-Visible spectroscopy both in absorption and emission mode. In here we report two case studies of the use of DR-UV-Vis spectroscopy applied to study MOF desolvation. The DR-UV-Vis spectra of $Ni_8(OH)_4(H_2O)_2(tet)_6$[102] activated at different temperatures showed a contribution of the linker and the *d-d* electronic transitions of Ni^{II} ions in a octahedral coordination geometry (Fig. 21a), while those of the Ni(BDPB) MOF (Fig. 21b)[105] showed components due to electronic transitions of the linker and *d-d* transitions of distorted octahedral Ni^{II} metal nodes.

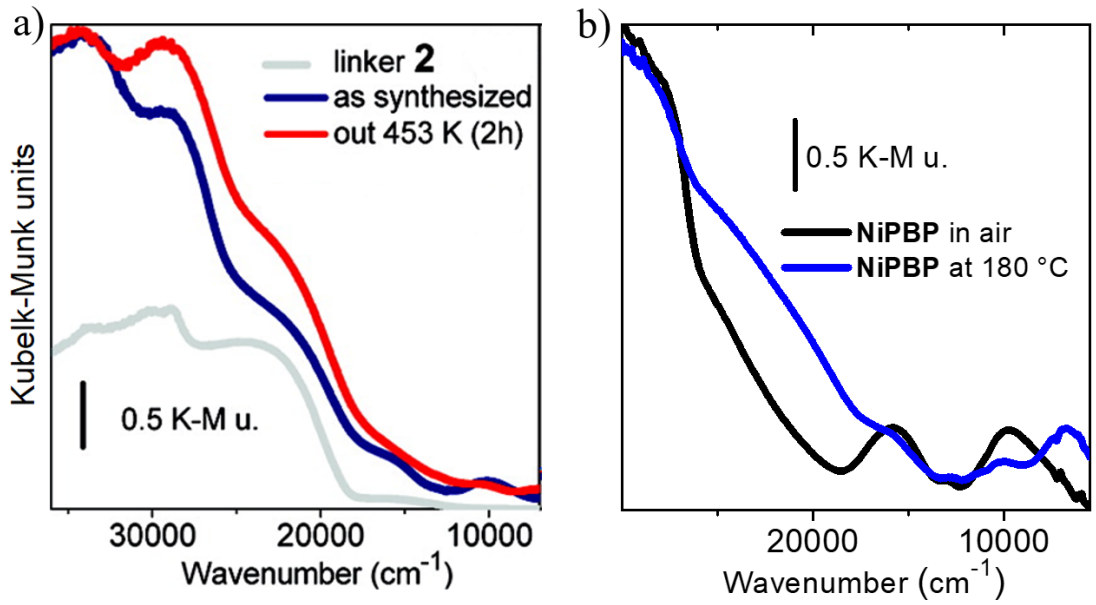

Fig. 21. (a) DR-UV-Vis spectrum of $[Ni_8(OH)_4(OH_2)_2(tet)_6]$. Adapted with permission from ref.[102], Copyright (2010) American Chemical Society. (b) DR-UV-Vis spectrum of Ni(BDBP) before and after thermal activation. Adapted from ref.[105] with permission of The Royal Society of Chemistry.

2.4 Volumetric and calorimetric measurements (Torino)

Being MOFs porous materials, they can have extremely high specific surface areas (in the range of thousands of square meters per gram of material) when the internal pore surface is accessible. With such high surface areas, adsorption of mobile phases (gaseous or liquid) has been proven to be a very useful phenomenon to define MOF properties and structures. For this reason, the collection of MOFs adsorption isotherms is one of the most important and typical characterization tools of this class of materials. Indeed, most MOFs applications rely on adsorption: gas storage and capture,[106] gas separation,[106] catalysis[107] or drug delivery.[108] The adsorption properties of a MOF material are normally investigated for two main reasons: (i) to obtain information on the pore structure using an adsorbate as a probe molecule to evaluate the amount (and nature) of accessible porosity; (ii) to study the material for applications in an industrial context that involves an adsorption step (gas capture and storage for example). Albeit closely related, the conditions used in these adsorption experiments are quite different: in the first case a weakly interacting molecule (*e.g.* N_2, Ar, Kr) is dosed at low temperature and pressure (typically at T = −196 °C and p < 1 bar), while in the second case the gas of industrial interest (H_2, CO_2 or CH_4 as the most popular) is dosed at conditions closest to the industrial process, which may range widely in both temperature (up to 500 °C) and pressure (even up to 200 bars). The vast majority of the research teams who are involved in MOF chemistry Worldwide characterizes their materials using volumetric techniques, measuring the specific surface area of the material by means of the BET or Langmuir theories, using N_2 as a probe dosed at −196 °C.[109] Italian groups make no exception, measuring routinely adsorption isotherms with the same purpose. In addition, the Torino group also uses adsorption microcalorimetry[110] to study adsorption processes in MOFs, measuring the adsorption isotherm and the heat involved in the process at the same time. As a representative example, the study of the adsorption properties of $Ce_2(NDC)_3(DMF)_2$ [87] revealed a peculiar aspect: upon DMF desorption to yield $Ce_2(NDC)_3$ by means of an *in vacuo* heat treatment, the material showed a certain degree of structural disorder but still the presence of diamond-shaped pores within its structure. The N_2 adsorption isotherm collected at −196 °C (Fig. 22) showed a negligible nitrogen uptake by $Ce_2(NDC)_3$, apparently contradicting the presence of such

pores or even pointing out their inaccessibility by the probe. Surprisingly, the CO_2 adsorption isotherm measured on $Ce_2(NDC)_3$ at −78 °C is a type I curve, typical of microporous materials (Fig. 22). The BET model applied to this isotherm led to the evaluation of a specific surface area of about 170 m^2/g. This result shows that $Ce_2(NDC)_3$ is featured by a porosity that cannot be traditionally determined through N_2 adsorption at −196 °C. The kinetic diameter of CO_2 is smaller than that of N_2; therefore, the former has access to smaller pores than the latter. Additionally, the experiment with carbon dioxide is performed 118 degrees above that of nitrogen, unlocking some phase change that may explain the appearance of porosity.

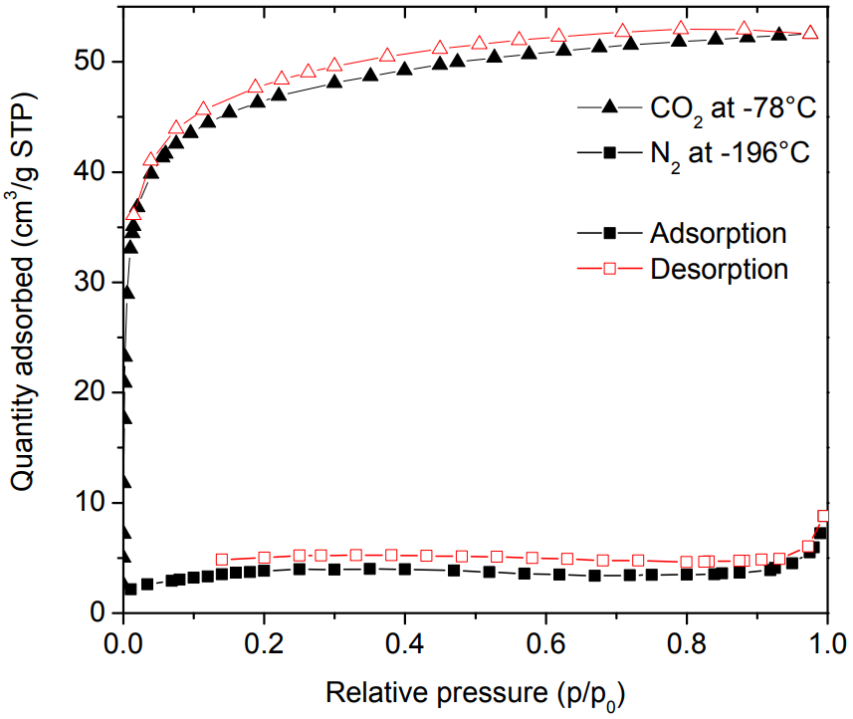

Fig. 22. N_2 and CO_2 adsorption isotherms measured at 77 K (squares) and 195 K (triangles) respectively on $Ce_2(NDC)_3$. Empty symbols indicate the desorption process. Reprinted with permission from ref.[87]. Copyright (2019) American Chemical Society.

UTSA-16 (UTSA = University of Texas at San Antonio) is a MOF based on Co^{II} and K^{I} and featuring citrates as linkers, whose formula is $K(H_2O)_2Co_3(cit)(Hcit)$ (cit^{4-} = fully deprotonated citrate anion). This material has gained a lot of attention within the MOF community because of its rare feature to

capture a remarkable amount of CO_2 (17 wt.% at T = 25 °C and p = 1 bar) even in the presence of water vapour (which usually brings MOFs to decomposition). These features make UTSA-16 a promising candidate for application in post-combustion CO_2 capture. The group from the University of Torino reported in a series of papers[111-113] the chemistry underneath CO_2 adsorption into the pores of UTSA-16, using volumetric and microcalorimetric techniques among the others. The main results are summarized in Fig. 23.

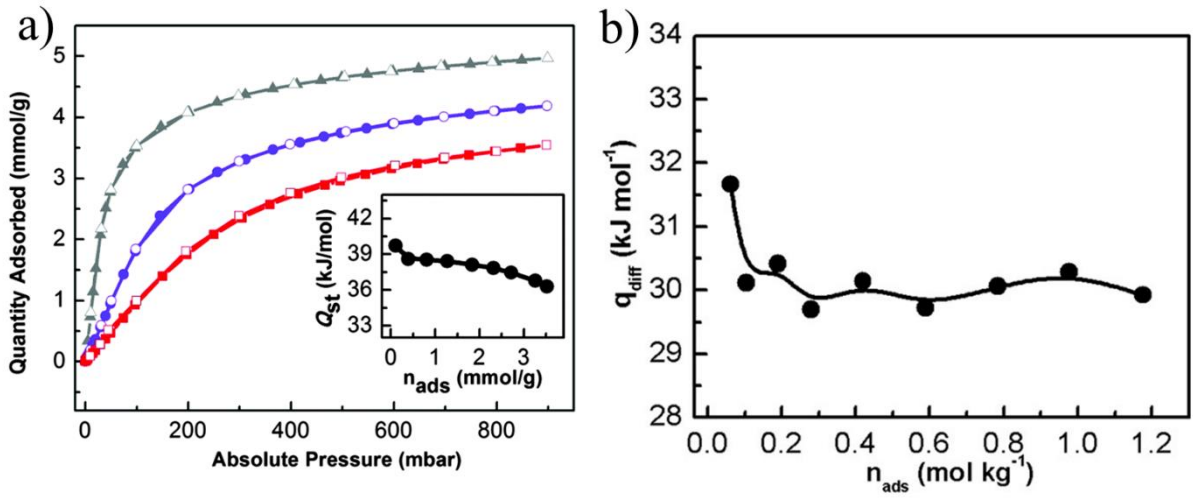

Fig. 23. (a) CO_2 volumetric adsorption and desorption isotherms on UTSA-16 and isosteric heat of adsorption (inset); isotherms at pressures between 0 to 1 bar at T = 0 °C (grey), 25 °C (violet) and 40 °C (red). Reproduced from ref.[112], with permission of The Royal Society of Chemistry. (b) Differential adsorption heat of CO_2 adsorption measured by means of microcalorimetry on UTSA-16 at T = 25 °C. Reprinted with permission from ref.[113]. Copyright (2019) American Chemical Society.

The UTSA-16 CO_2 adsorption isotherms are of type I (Langmuir). Isotherms collected at different temperatures provide the isosteric heat of adsorption (inset in Fig. 23a) through application of the Clausius-Clapeyron equation. This value can be compared with the differential heat coming from a "direct" measurement, obtained by means of a microcalorimeter (Fig. 23b). These heat *vs.* coverage curves are a wonderful tool in characterizing a gas sorbent like UTSA-16 because they can measure the amount of heat released during the adsorption of increasing doses of adsorbate, ultimately characterizing the nature and abundance of the adsorption sites. Differences between the isosteric

heat and the differential heat curves may be due to the simplified assumptions of the isosteric heat model, which may not be completely fulfilled during adsorption on a "real" porous material.

3. Theoretical studies on MOFs physico-chemical properties (Torino)

The computational work carried out in Torino aims at elucidating the role of the two building blocks of MOFs, *i.e.* the metallic node and the organic linker, and of the framework to highlight structure-property relationships. While SBUs can play a distinct role in determining the properties of MOFs, the framework as a whole often shows new intriguing properties that are not the simple sum of those of its constituents. The first theoretical investigation on a MOF carried out by the Torino team was reported in 2006 with a thorough modelling of MOF-5 that at that time was still the subject of many investigations, while has presently assumed the role of the archetypical MOF. The structural, electronic and vibrational properties of MOF-5 were analyzed in details to understand the interplay between the organic linker and the inorganic cluster.[4] It was shown that the former determines the energy levels of the frontier orbitals while the [Zn_4O] cluster shows similar bonding features as cubic zinc oxide but with a significantly different electronic structure. This result demonstrated the role of the organic linker in modulating the band gap of an isoreticular MOF family, as confirmed experimentally[114] and theoretically[115, 116] a few years later. The remarkably good results obtained for MOF-5 stimulated the interest of people working in the field of MOFs to combine experiment and theory. Very fruitful collaborations then started with several groups both in Italy (Como) and abroad (Oslo and Oxford). For instance, the synergic combination of experiment and theory allowed us to describe the complex structure of the well-known Zr MOF UiO-66[117] and its isoreticular parent UiO-67,[118] thus supporting and confirming the experimental findings on the phase transition of UiO-66 from a fully hydroxylated to a fully dehydroxylated form with a modification of the coordination number of the zirconium atoms. It is worth to mention that other Italian computational chemists also supported experimentalists in understanding the structure of a

different series of isoreticular Zr oxide dicarboxylate MOFs with the same structural type of MIL-140.[119] Theoretical modelling was also employed to analyze the structure of bipyrazole- and tris(pyrazole)-based coordination polymers and MOFs in collaboration with the research teams in Camerino and Como, in particular the M-BPZ and M-BDP MOF families (Table 1 and Section 1.1) with different divalent metals (Co, Ni, Cu, Zn)[23, 120, 121] and $Ni_3(BTP)_2$.[122] Nevertheless, one of the major successes in structure prediction was the rationalization of the exceptional bistability of MIL-53(Al). This material is known for its guest-free reversible transition driven by temperature between a narrow pore (low-temperature phase, LT) and a large pore (high-temperature phase, HT) form (Fig. 24). The occurrence of LT to HT phase transition was elucidated through *ab initio* calculations; the results showed that the temperature increase sparkles a competition between short- and long-range interactions and entropic factors. Consequently, the LT structure is stabilized at low temperature by dispersion interactions, while entropy drives the pore opening to the HT phase.[123]

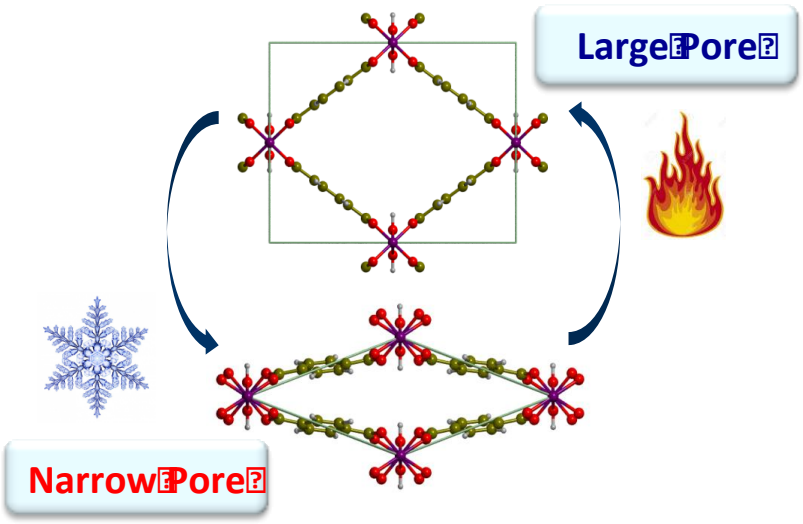

Fig. 24. Schematic picture of the reversible temperature-driven phase transition of MIL-53(Al) from a narrow pore to a large pore structure. Color code: violet Al, red O, yellow C, grey H.

3.1 Adsorption of small molecules: from small to giant MOFs

Over the years, one of the primary goals of computational studies has been the in depth understanding of MOFs ability to adsorb molecules for applications in gas capture and storage. Indeed, MOFs are particularly suitable for this application, due to their highly porous structure and the frequent presence of open metal sites after activation. Open metal sites are created after labile linkers removal through thermal activation treatment, leaving behind coordination vacancies that may work as strong adsorption sites for many different molecules (*e.g.* CO, CO_2, acetylene, H_2S), but they can also act as Lewis acidic catalytic sites. Among the various MOFs of the literature, MOF-74 and its analog CPO-27 formed with a divalent metal and the 2,5-dihydroxyterephthalate organic linker (Fig. 25b) gained a lot of attention for the presence in their channels of exposed metal sites. A family of isostructural CPO-27(M) MOFs containing different divalent metals (Mg, Fe, Co, Ni, Zn) was successfully prepared, to tune the type and strength of the host-guest interactions.

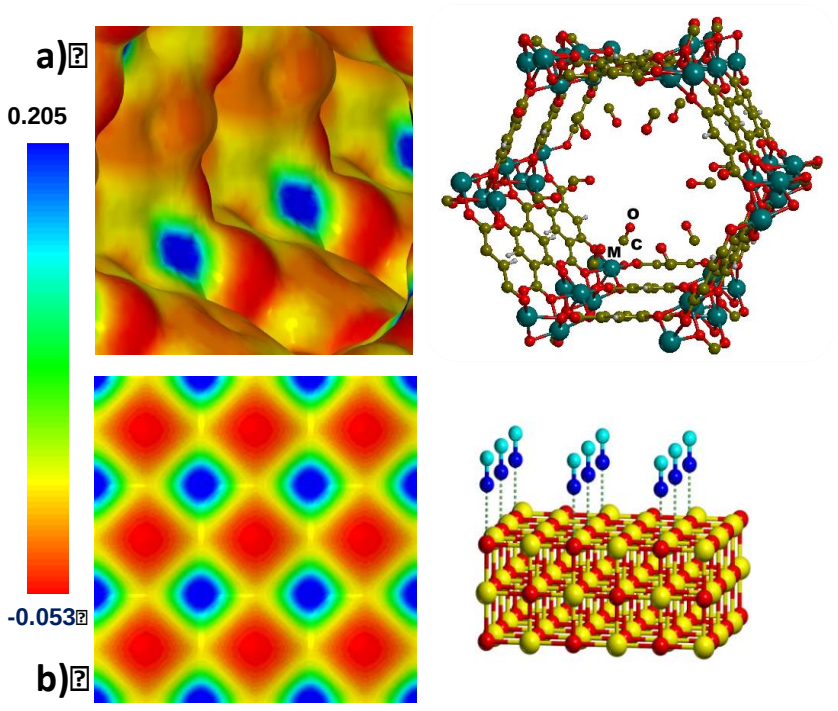

Fig. 25. Comparison between (a) the electrostatic potential mapped on a charge density isosurface of the inner surface of CPO-27(Mg) and the MgO(001) surface and (b) the corresponding structural arrangement of CO in the channels of CPO-27(Mg) and at the surface of MgO(001).

In Torino, along with an extensive experimental work, a theoretical work was also carried out in parallel to better understand the adsorption properties of CPO-27(M) toward small molecules such as CO, N_2, CO_2, NO, H_2O and H_2S.[124-127] In particular, a detailed *ab initio* study was carried out in collaboration with Prof. J. Sauer in Berlin on the prediction of the heats of adsorption of CO and CO_2 in CPO-27(M) (M=Mg, Ni, Zn). Density functional theory periodic calculations including dispersion corrections at the B3LYP-D* level were combined with a hybrid high-level (MP2 with complete basis set extrapolation): low level (B3LYP+D*) method. The MP2 calculations were performed on cluster models. Calculated values of the heat of adsorption at zero coverage (Q_{st}) were in reasonably good agreement with those experimentally obtained. Calculations also showed the significant role played by dispersion forces, which account for more than one-half of the adsorption enthalpy. Both the B3LYP-D* and the hybrid MP2/CBS:B3LYP+D* method correctly predicted the same sequence of binding energies for carbon monoxide (Ni > Mg > Zn) and carbon dioxide (Mg > Ni > Zn) adsorption on open metal cation sites. Theoretical calculations also provided insights into the role of the MOF inorganic building unit by answering the following questions: can the inorganic part of a MOF be considered as a nanostructured oxide? Can open metal sites always be effective adsorption sites? For instance, the adsorption properties of CO on the MgO_5 moiety in CPO-27(Mg)[126, 127] showed a somewhat large difference with respect to the corresponding oxide MgO(001) surface.[128] Indeed, the computed Q_{st} values (with a B3LYP-D* method and a triple-zeta quality basis set) are 34.2 kJ/mol and 13.8 kJ/mol for CPO-27(Mg) and MgO(001), respectively. In the MOF, the Mg^{II} open sites are more exposed at the surface because of a less regular arrangement of the surrounding oxygen atoms so that the metal ion is more prone to interact with the adsorbed molecule. Indeed, while the contribution to dispersion interactions is similar in both cases (about 14-16 kJ/mol), the remaining contribution to the interaction energy is 2.3 kJ/mol for the MgO(001) surface and 17.7 kJ/mol for CPO-27(Mg) despite the almost identical Mg···CO distance (*ca.* 2.49 Å). Such a difference can also be highlighted in the electrostatic potential of the two surfaces, as shown in Fig. 25a. Therefore, the exposed metal sites at the inner surface of the MOF show largely different adsorption properties and

higher interaction energies with respect to the corresponding counterparts in MgO, because of the different local coordination environment. In contrast to CPO-27(M) where the metal ion acts as a strong adsorption site for probe molecules,[127] in Ni^{II} bipyrazole- and tris(pyrazole)-based MOFs (Section 1.1) no specific interactions were observed despite the coordinatively unsaturated metal sites, as evidenced by FTIR measurements (Section 2.3).[121, 122] In CPO-27(Ni), Ni^{II} is five-coordinated (in a square pyramidal coordination geometry) with a high-spin (HS) state, while the linking with pyrazolate generates four-coordinated square planar coordination arrangements with the metal in a low-spin (LS) state. The high stability of the Ni^{II} LS state together with the limited accessibility of the metal centers due to steric effects were demonstrated to be at the basis of the absence of preferential M···CO interactions in Ni(BPB) and $Ni_3(BTP)_2$. Such stability-reactivity behavior was even more evident in $Ni_3(BTP)_2$ where the metal is well exposed in the pores. The electrostatic potential map of the optimized low spin structure (Fig. 26) did not show any evidence of a positive region in close proximity of the metal sites (normally observed for Lewis acidic metal ions; see Fig. 25a for comparison). This may be due to the strong N-donor character of the pyrazolate linkers. Accordingly, the calculated Ni···CO binding energy of a few kJ/mol is negligible. The interaction with CO is stronger when Ni^{II} is in a HS state (with a binding energy of 45 kJ/mol), but this is not enough to lead to a spin transition because of the high LS-to-HS energy barrier of 75 kJ/mol.

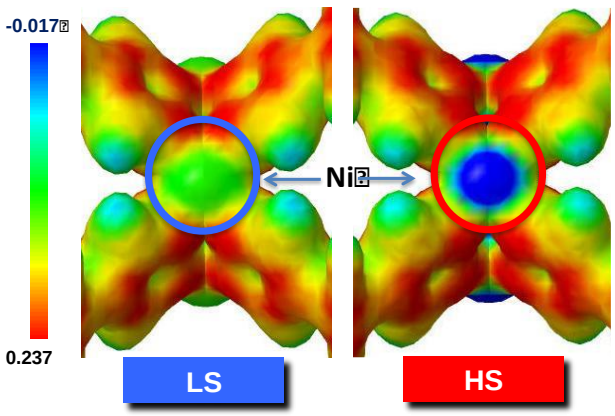

Fig. 26. Electrostatic potential of the two LS/HS phases of $Ni_3(BTP)_2$ mapped on top of the charge density isosurface (*i.e.* 0.02 a.u.) around the Ni metal ion. Adapted from ref.[122].

In the research field of adsorption of small molecules in MOFs, a hot topic area is CO_2 capture and storage. *Ab initio* modeling is a valuable tool to investigate the interactions between the framework and carbon dioxide. Along with the role played by the open metal sites as discussed above for CPO-27(M), tailored functionalized linkers can also act as efficient adsorption sites, in particular those bearing basic sites like amino groups. In a joint collaboration between Torino and Oslo, both hydroxylated and dehydroxylated forms of the amino-functionalized UiO-66 were investigated.[129] Theoretical calculation corroborated the experimental evidence that the interaction of carbon dioxide with the $-NH_2$ group is rather small: less than 20 kJ/mol. A combined effect of -OH and $-NH_2$ groups is observed, instead, that leads to an estimated $Q_{st}(298K)$ = 29.1 kJ/mol which nicely compares with the experimental adsorption enthalpy of 27 kJ/mol. Torino, Como and Camerino also worked together on a combined experimental and theoretical study of the interaction of CO_2 with the pyrazolate-based MOFs M(BPZ) (M = Co, Cu and Zn).[23] In particular, none of the examined systems showed a specific adsorption site for CO_2. For the Co and Zn pyrazolate MOFs, results showed that the tetrahedrally coordinated metal prevent a direct interaction with the molecule and the computed adsorption enthalpies approaches the liquid-like limit. Also for the Cu pyrazolate, where the metal is in a square-planar coordination geometry, the interaction resulted to be rather small. In both cases, theoretical predictions agreed with experimental findings. For several years the theoretical studies of MOFs in Torino focused on small-to-medium size MOFs, but with the advent of supercomputers and efficiently parallelized codes as CRYSTAL,[130] quantum mechanical calculations on MOFs were pushed a step forward by tackling the very challenging task of modelling the gigantic metal-organic framework MIL-100(M)[131] that contains 2788 atoms in the unit cell.[132] As a comparison, MOF-5 contains only 106 atoms in the unit cell. Large scale DFT-D calculations were exploited to shed light on the structural features of MIL-100(M) materials, where M^{III} = Al, Sc, Cr, Fe. Strikingly, the

predicted structures were in overall agreement with the experimental ones even for such a huge system. It is worth mentioning that within the MIL-100(M) family, the chromium-containing MOF shows the highest affinity for CO_2 as measured so far for various porous materials.[106] Therefore, calculations were extended to analyze the interaction of carbon dioxide with the open metal sites of MIL-100(M). Note that there are 136 possible sites, so that only a very low CO_2 loading was modelled. The matching between calculated and experimental interaction energies was not always good; chromium and scandium in particular gave the worst outcomes. However, the results showed the correct sequence overall, with chromium being the strongest adsorption site followed by scandium, iron and aluminum. The latter shows the largest electrostatic potential, but it is tightly surrounded by oxygen atoms and less exposed at the surface, while scandium (with a larger ionic radius) is well exposed at the surface and with an easier interaction with CO_2. Chromium has a strong affinity for CO_2, providing the shortest $M\cdots CO_2$ distance among the various metals investigated. This may be ascribed to its high electrostatic potential and to its d^3 valence electron configuration. In spite of the discrepancy with the experimental data, the computed interaction energies were consistent with those of MIL-127 (a MOF with similar open metal sites) and with calculations on cluster models.[133] The latter findings suggested that the main contribution to the interaction energy comes from the exposed metal nodes, and not from the organic linkers. The discrepancy between experimental and theoretical data on MIL-100(Cr) probably stems from a defective nature of the real framework and the consequent lack of a uniform distribution of the adsorption sites. Finally, we would like to evidence a very recent work on the adsorption of drugs in MOFs carried out in Torino within a collaboration with Prof. J.C. Tan of Oxford University.[134] In particular, theoretical modelling based on a newly developed cost-effective hybrid HF/DFT composite method for solids[135] was used to reveal the interaction of 5-fluoro-uracil with the Cu^{II}-based MOF HKUST-1 at an atomistic level. In addition, the detailed dynamics of vibrational motions underpinning the dissociation of the drug upon water exposure was analyzed to support the experimental investigation via *in situ* synchrotron microspectroscopy.

3.2 Understanding structure-property relationships in MOFs

Beyond adsorption properties, MOFs exhibit other promising physico-chemical features (*e.g.* electronic, dielectric, mechanical) that emerge from the remarkable versatility and structural behavior of the frameworks. This is central to other growing fields such as stimuli-responsive devices and MOF-mechanics, to mention a few. In the following paragraphs, we briefly review some recent results on MOFs dielectric response and elasticity/lattice dynamics, which are crucial for their exploitation in technological applications. Most of the work has been carried out within a collaboration between Torino and Oxford. For next-generation devices in micro- and optoelectronics, ultra-low-κ dielectric materials ($\kappa < 2.0$) with a crystalline and porous structure are highly desirable. MOFs have then attracted a lot of attention and have been suggested as future low-κ materials in the International Roadmap for Devices and Systems - More Moore White Paper, IEEE (Institute of Electrical and Electronics Engineers, New York, 2016). Because of their customizability it is crucial to rationalize the role of the SBUs and the framework in controlling the dielectric response of MOFs. A systematic study was recently conducted for a large set of MOFs to rationalize the structural and chemical features that can influence the electronic and dielectric properties.[115] It was shown that most of the examined MOFs are ultra-low-κ materials with a static dielectric constant that reaches a value as low as 1.25. Furthermore, despite the chemical versatility of MOFs that allows for tuning the material band gap and polarizability by using different metals and organic linkers, the value of the static dielectric constant is mostly related to the framework. Indeed, a clear correlation of the dielectric constant with the framework porosity was highlighted (Fig. 27). Notably, this result was confirmed by combining experiment and theory through pioneering synchrotron-based infrared reflectivity experiments and *ab initio* calculations for a series of zeolitic imidazolate frameworks (ZIFs), a topical family of MOFs.[136] The strong dependence of the dielectric constant on the level of porosity of the framework for the two sets of the examined MOFs (Fig. 27a) and ZIFs (Fig. 27b) is illustrated.

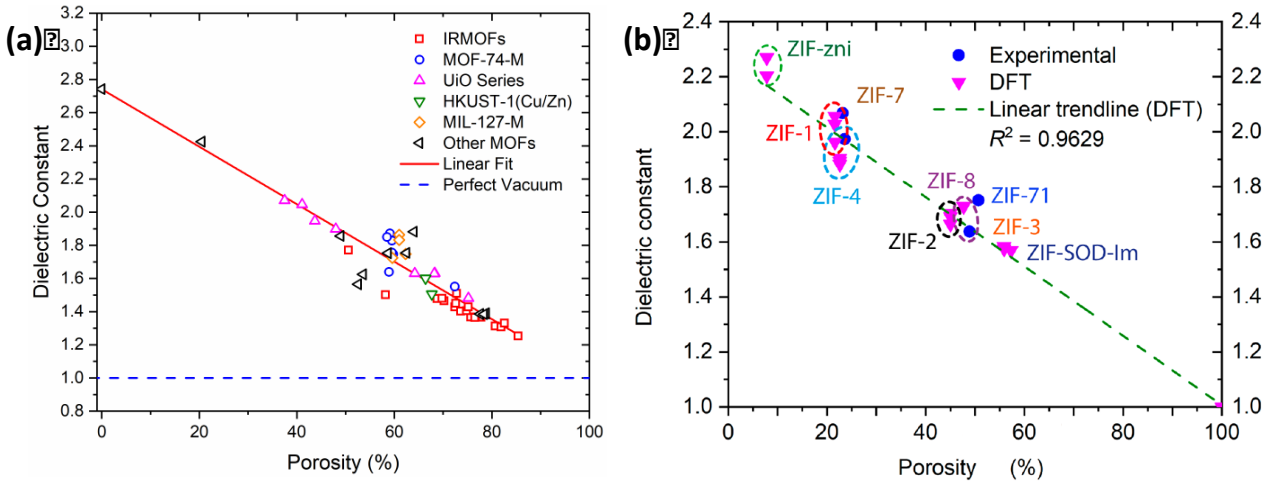

Fig. 27. Dependence of the dielectric constant on the level of porosity of MOFs (a) and ZIFs (b). The linear trend is highlighted with a solid red line (a) and a dashed green line (b). Adapted from refs [136] and [115].

MOFs are stimuli-responsive materials. Indeed, they show large amplitude structural changes in response to physical or chemical stimulation.[137] The transformation can be induced by temperature, mechanical pressure, guest adsorption or evacuation, light absorption. It has been found that the phase transition occurring in MIL-53(Al) described above in Section 3.1 can also be induced through the application of an external pressure to the framework. Recently, theoretical calculations were combined with high-resolution synchrotron infrared specular reflectance experiments to study the change in the dielectric response of MIL-53(Al) as a function of the applied stress.[138] The switching between the large pore (LP) and the narrow pore (NP) structure causes a remarkable decrease in the band gap and increase in the dielectric constant (LP: 1.5 $\rightarrow$ NP: 2.2) for the closed phase as the porosity is removed. These results demonstrate the tunability of the dielectric response as a function of the composition of the material in terms of the LP:NP ratio, as shown in Fig. 28 for the real part of the complex dielectric function. This interesting behavior could open the door to the reversible and controllable switch between the LP $\rightleftharpoons$ NP configurations. Furthermore, an excellent agreement of experimental complex dielectric function data with theoretical DFT calculations was obtained that suggested a pathway to the *in silico* design of tunable MOF dielectrics. A similar

investigation was also carried out on the prototypical Cu^{II} MOF HKUST-1[139] to gain insights on the temperature- and pressure-dependent broadband dielectric behavior.

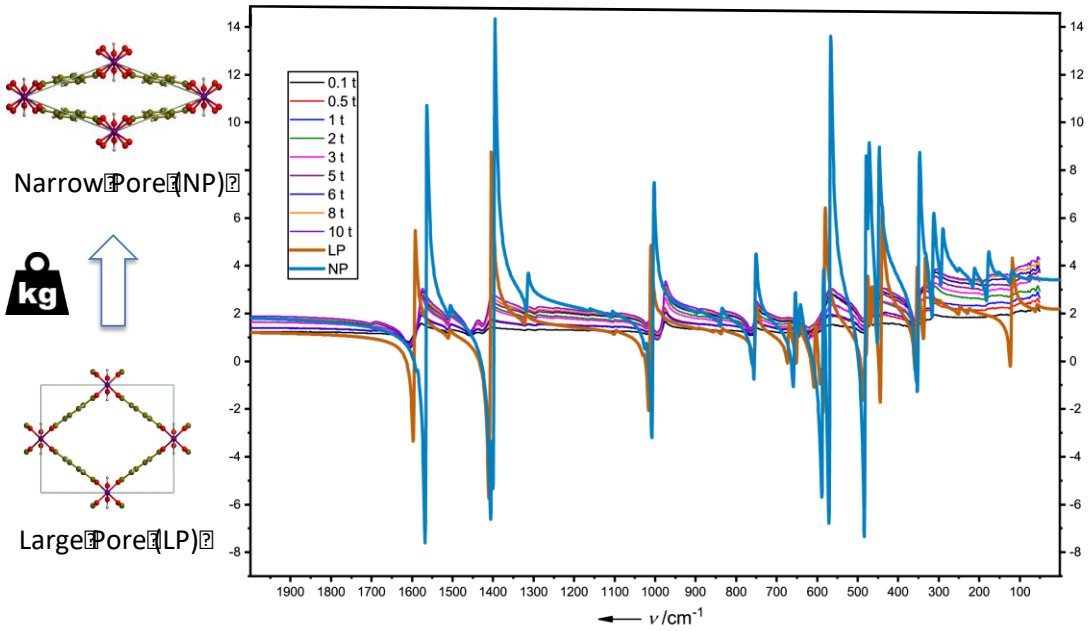

Fig. 28. Comparison between experimental data (thin solid curves) as a function of the applied pressure and predicted values (thick solid curves) for the real part of the complex dielectric function of MIL-53(Al). Adapted from ref.[138].

It is clear from the discussion above that flexibility of MOFs is a key concept, which is actually related to elasticity and lattice dynamics. The latter are also crucial to understand the mechanical properties of MOFs that are relevant to address the robustness, durability and resilience of the framework for designing devices to be used in technological applications. In the last years, a combined experimental and theoretical work in Oxford and Torino was undertaken to connect elasticity and lattice dynamics to the materials mechanical stability. In particular, synchrotron vibrational spectroscopies, in conjunction with *ab initio* calculations, were used to study the low-frequency vibrational modes in the THz region of MOFs as HKUST-1,[140] MIL-140A[141] and a series of ZIFs.[142] Modelling revealed the complex nature of the collective atomic motions that lead to low-energy conformational dynamics underpinning framework deformation mechanisms such as hindered rotations of organic

linkers and trampoline-like motions. The computed results aided to highlight the linking of THz modes to gate-opening, pore-breathing and shearing deformations that are relevant to structural stability/instability (*e.g.* framework collapse and/or amorphization). In parallel, further theoretical work was carried out to connect lattice dynamics to elasticity (and *vice versa*). The results found here showed that soft modes could be related to the softening of the material and unveil elastic anomalies in the mechanical behaviour of MOFs. Calculation of the second-order elastic constants through density functional methods was employed to predict related mechanical properties (Young's modulus, shear modulus, linear compressibility and Poisson's ratio). Interestingly, most of the examined systems showed a clear anisotropic elastic response. For instance, it was discovered that the prototypical imidazolate-based framework material ZIF-8[143] shows an exceptionally low shear modulus that might lead to a structural instability. Indeed, the latter is connected to a shear distortion soft mode of the framework[142] which is responsible for a phase transition when ZIF-8 is subjected to high pressure.[144] This finding was later confirmed by another theoretical study of the anisotropic mechanical response of ZIF-8 as a function of pressure.[145] The pressure-driven mechanical instability of the framework was then explained in terms of the C_{44} shear elastic constant with a shear deformation entangled with asymmetric "gate-opening" vibrations. Similar highly anisotropic elastic properties were predicted for other ZIFs, namely ZIF-4 and ZIF-zni, according to which ZIF-4 could exhibit a negative Poisson's ratio thus potentially manifesting some auxeticity.[146] For HKUST-1 (Fig. 29a),[140] a detailed investigation of the elastic properties in conjunction with a careful vibrational analysis highlighted that the co-existence of soft modes (*e.g.* hindered rotations and trampoline-like motions, Fig. 29b-c) and intrinsic shear distortions governed the emergence of anomalous phenomena such as auxeticity (as highlighted in Fig. 29d by the negative values of the Poisson's ratio surfaces) and negative thermal expansion.

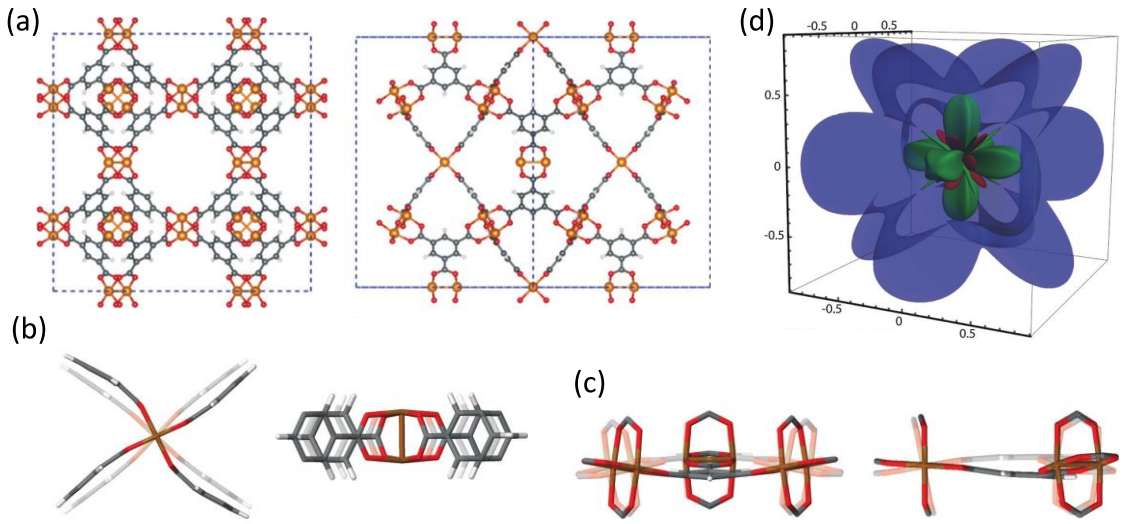

Fig. 29. HKUST-1 unit cell (a) viewed along the [100] and [110] directions; (b) and (c) show examples of hindered rotations of organic linkers and trampoline-like motions, respectively; (d) Poisson's ratio surfaces: maximum is depicted as blue and minimum as green and red for positive and negative values. Adapted from ref.[140]. The full set of computed vibrational modes can be visualized at the following link: https://www.crystal.unito.it/vibs/hkust-1.

Unusual elastic anisotropy due to the exceedingly low shear moduli properties of MOFs was also discovered in the isoreticular family of MIL-140 A-D[147] in which infinite 1-D zirconium oxide (ZrO) chains are linked together through different organic linkers (Fig. 30a-b). Within this family, the structure–mechanical property trends were rationalized referring in terms of different spacers length. The rigidity of the framework is dramatically reduced by shear deformations for structures with longer linkers (Fig. 30c-d). An excellent correlation was established to experiments in that the predicted trends agree with the grinding time required to cause mechanical collapse of the framework in ball-milling experiments. Understanding structure–mechanical stability trends is then important for the design of tailored frameworks for technological applications.

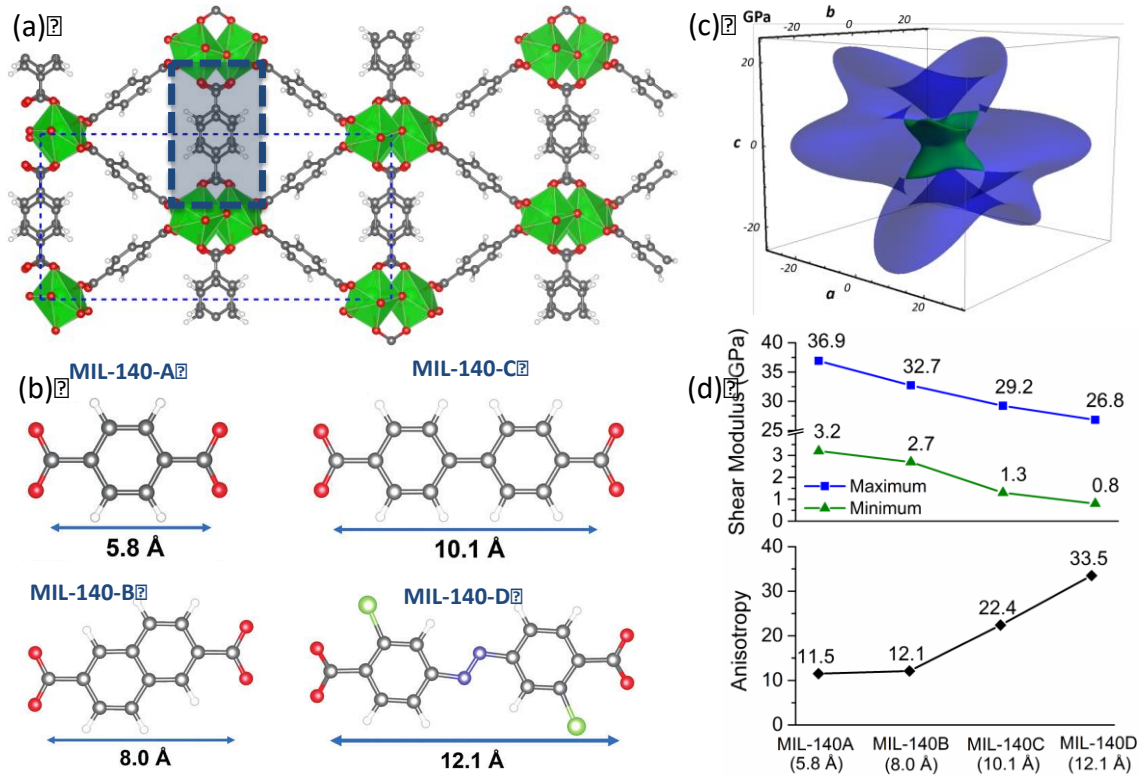

Fig. 30. (a) Hybrid framework of the MIL-140 MOF along with the different linkers of the MIL-140 family (A-D) (b); (c) Shear modulus surface of MIL-140-A and (d) dependence of the shear modulus and anisotropy on the linker length. Adapted from ref.[147].

Finally, it is worth mentioning a recent work on the quasi-harmonic lattice dynamics of MOF-5[148] as an example of the inclusion of thermal effects in the modelling of MOFs. The observed negative thermal expansion of MOF-5 was nicely reproduced by *ab initio* calculations. A value for the linear thermal expansion at 300K of -11 $\cdot 10^{-6}$ K^{-1} was predicted in agreement with the experimental data that range from -12 to -14$\cdot 10^{-6}$ K^{-1}. By combining temperature and pressure, a shear-induced instability was also shown upon compression, responsible for a group-subgroup phase transition at about 0.45 GPa.

Overall, the theoretical work carried out in the last decades in Torino demonstrates that modelling offers valuable insights into the detailed physical and chemical characterization of MOFs both as a support for the elucidation of experimental findings and as a stand-alone predictive tool.[149]

4. Applications

4.1 Gas storage and separation

This field of investigation is probably the most widely explored in MOFs science. Examples dealing with many different gases (either pure or in binary mixtures to assess adsorption selectivity) physisorbed under various temperature and pressure conditions are present in the literature. The renaissance of the interest in coordination polymers and MOFs at the beginning of the new century stems from the initial discovery of (micro)porosity and high surface areas for some of these materials and the possibility to store molecular hydrogen (H_2) at cryogenic temperatures inside them. In more recent years, the interest in hydrogen adsorption in MOFs has faded because of the limited storage capacity of the materials discovered so far and of the impossibility to store this gas in significant amounts (for practical applications in vehicles equipped with fuel cells) at temperatures above –196 °C. Thus, new research lines have started to appear towards storage/separation of other gases of environmental/energetic interest like carbon dioxide (CO_2) and methane (CH_4), short-chain hydrocarbons like ethylene, acetylene, hexanes or chemical welfare agents employed in military contexts like mustard gas [bis(2-chloroethyl) sulfide] or hydrogen sulfide (H_2S).

4.1.1 Hydrogen storage (Firenze)

For very light gases like hydrogen, the employ of lightweight materials (*i.e.* MOFs containing light elements like lithium, magnesium, calcium, aluminum) is essential to increase the weight percentage of the adsorbed hydrogen and consequently to have a better-performing gas sponge. Hydrogen storage measurements were carried out at T = –196 °C in a low-to-high pressure interval with the polymeric

formate $Mg(HCOO)_2(HCOOH)$ after amine guest removal through thermal activation.[53] The maximum experimental H_2 uptake at T = –196 °C and p_{H2} = 30 bar corresponds to 12 H_2 molecules per cell, *i.e.* 0.88 H wt. % (Fig. 31a). The existence of preferred H_2 adsorption sites was assessed through Grand Canonical Monte Carlo (GCMC) simulations. No specific low-energy site was found (there are no open metal sites in the activated framework), and H_2 location in the framework pores is simply determined by packing effects. Consequently, the center of the cubic cavities (that assures a spatially uniform H_2-framework interaction) is the preferred adsorption site at low pressures (Fig. 31b), while, two more "localized" positions were found at high pressures because of the reduced empty space available under these "more packed" conditions (Fig. 31c).

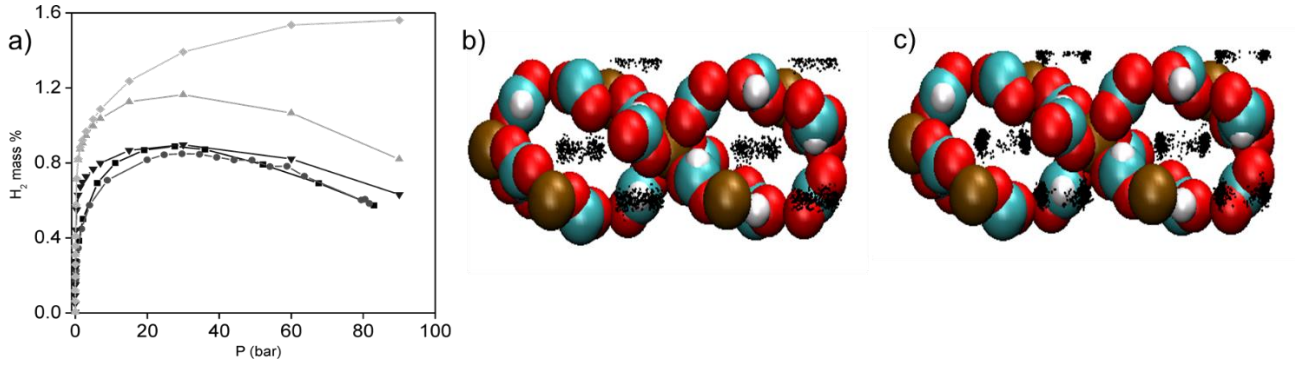

Fig. 31. (a) H_2 adsorption isotherms recorded at –196 °C on $Mg(HCOO)_2(HCOOH)$; GCMC density distributions at p_{H2} = (b) 0.2 bar and (c) 100 bar. View along the Z-axis. Atom color code: brown, Mg; light blue, C; white, H; red, O. Adapted with permission from ref.[53]. Copyright (2011) American Chemical Society.

4.1.2 Carbon dioxide capture and separation (Como, Camerino, Firenze, Perugia, Pisa, Torino)

The abundant presence of polar C-N and C-S bonds in thiazole- and thiazolidine-based MOFs is helpful to improve the interaction with the polar C=O bonds of carbon dioxide, despite the very low BET area found in the materials. It has been demonstrated[106] that the CO_2 adsorption capacity in post-combustion industrial flue gas (where the CO_2 percentage in the mixture is very low if compared with that of N_2) is predominantly dictated by the chemical features of the pore surface, and it is not

strictly related to the surface area of the material. Thus, the best performing materials are those bearing highly polarized surfaces. Indeed, CO_2 adsorption in the thiazolidine-containing MOF Co(L-*RR*) after thermal activation (Fig. 5) gave the satisfactory value of 4.7 CO_2 wt. % at T = 0 °C and p_{CO2} = 1.2 bar.[44] The Cu^{II} MOF CuL_2 made with thiazole-5-carboxylate (Fig. 6) shows an even higher and remarkable CO_2 uptake of 9.0 CO_2 wt. % at T = 30 °C and p_{CO2} = 1.2 bar.[45] Finally, the Zr^{IV} bithiazole-based MOF $[Zr_6O_4(OH)_4(TzTz)_6]$ (Fig. 7) with a longer linker and a higher BET area (840 m^2/g) can store 7.5 CO_2 wt. % at T = 25 °C and p_{CO2} = 1 bar.[46]

The MOF-76-Ce prepared in Torino[85] (Fig. 15a) showed excellent carbon dioxide adsorption properties, with an uptake of 15 wt. % at 1.1 bar and 25 °C after activation at 250 °C (and concomitant full desolvation). The high isosteric heat of adsorption (35 kJ/mol) and the negligible nitrogen uptake under the same conditions make this material an ideal candidate for CO_2/N_2 separation processes in dry environments. The same team has also studied CO_2 adsorption through volumetric and calorimetric techniques on $Ce_5(BDC)_{7.5}(DMF)_4$ (Fig. 15c): a modest adsorption capacity (3.5 wt. %) was found, and a specific heat of adsorption (32-33 kJ/mol) compatible with the existence of some kind of interaction with the MOF open metal sites.[88]

The Ce^{IV}-MOF F4_MIL-140A(Ce) prepared by the Perugia team (Fig. 16b) displays a peculiar CO_2 adsorption behavior. The isotherm has sigmoidal shape, with pores saturation occurring over a small range of pressures, a behavior typical of the so-called phase-change adsorbents (Fig. 32a). The inflection point in the isotherm appears at pressures compatible with post-combustion capture and shifts to higher pressure as the temperature increases. Since the same phase-change behavior is not triggered by N_2 adsorption, F4_MIL-140A(Ce) displays the remarkable CO_2/N_2 selectivity of over 1900, estimated using the ideal adsorbate solution theory (IAST) for an ideal 0.15:0.85 CO_2:N_2 v/v gas mixture at 20 °C and 1 bar total pressure, which is among the highest values reported for a MOF (Fig. 32b).[92] Despite the total CO_2 uptake of F4_MIL-140A(Ce) at 1 bar and 20 °C is moderate (1.9 mmol/g, 8.4 wt. %), the absence of hysteresis upon CO_2 desorption is very attractive to achieve

high working capacity with little energy penalty. The isosteric heat of adsorption (Q_{st}) measured at zero coverage is around 40 kJ/mol, indicative of favorable physical interactions between the adsorbate and the MOF surface without formation of strong chemical bonds. The CO_2 adsorption sites in this material are likely to be both coordinatively unsaturated cerium ions and the linker's perfluorinated aromatic rings. Investigations are ongoing to unravel this aspect.

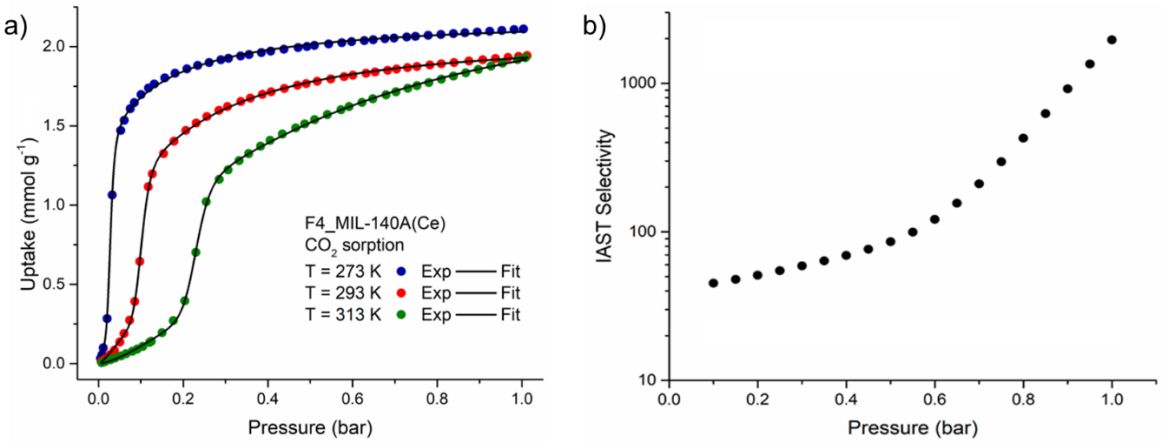

Fig. 32. (a) CO_2 adsorption isotherms collected at 0 °C (blue), 20 °C (red) and 40 °C (green) for F4_MIL-140A(Ce); (b) IAST selectivity as a function of total pressure for a 0.15:0.85 CO_2/N_2 mixture at 25 °C for F4_MIL-140A(Ce). Adapted with permission from ref.[92]. Copyright (2019) American Chemical Society.

As a representative example of the influence of the linker steric hindrance on the CO_2 uptake in a series of isostructural MOFs, the Como and Camerino teams assessed the CO_2 adsorption capacity of the M(Me_2BPZ) (M = Co, Zn) MOFs[21] and compared it to that of the non-methylated M(BPZ) parents.[18] The beneficial effect of the methyl groups in the thermodynamics of CO_2 sorption, as suggested by the adsorption energy trend [E_{ads}(M(Me_2BPZ)) > E_{ads}(M(BPZ))] and supported by theoretical calculations at the B3LYP-D3 level coupled to topological analyses, is unfortunately compensated by the higher steric hindrance of the tagged linker. Consequently, the quantity of gas adsorbed by the tagged MOFs *vs*. its untagged counterpart is reduced (2.0-2.6 mmol/g *vs*. 3.8-4.4 mmol/g, respectively, at 0 °C and 1 bar pressure). When moving to the analysis of the tags polarity influence on the CO_2 adsorption performance, the Camerino, Como and Firenze groups investigated the CO_2 adsorption capacity and affinity of the M($BPZNO_2$)[27] and M($BPZNH_2$)[28] (M = Cu, Ni,

Zn) families. $Zn(BPZNH_2)$ adsorbs 3.07 mmol g^{-1} (13.5 wt. % CO_2) at T = 25 °C and p_{CO2} = 1 bar, with an isosteric heat of adsorption Q_{st} = 35.6 kJ mol^{-1} and a CO_2/N_2 Henry and IAST selectivity of 17 and 14, respectively, outperforming its nitro-tagged counterpart $Zn(BPZNO_2)$. As a prosecution of this work, the mixed-linker MOFs (MIXMOFs) $Zn(BPZ)_x(BPZNO_2)_{1-x}$, $Zn(BPZ)_x(BPZNH_2)_{1-x}$, $Zn(BPZNO_2)_x(BPZNH_2)_{1-x}$, and $Zn(BPZ)_x(BPZNO_2)_y(BPZNH_2)_{1-x-y}$ were isolated and analysed for CO_2 adsorption capacity, CO_2/N_2 selectivity and isosteric heat of adsorption.[150] This comparative study (including also the single-linker analogues) highlighted the influence of both tag nature and linker stoichiometric ratio on CO_2 adsorption. In particular, the NH_2-decorated compounds showed higher Q_{st} values and CO_2/N_2 selectivity *vs*. the nitro-functionalized counterparts. On the other hand, tag "dilution" with BPZ^{2-} increased CO_2 adsorption selectivity over N_2. Overall, the best compromise among capacity, isosteric heat of adsorption and CO_2/N_2 selectivity was obtained with $Zn(BPZ)_x(BPZNH_2)_{1-x}$. The Ni(BDP) and Zn(BDP) MOFs[19] with BET areas of 1600 and 2000 m^2/g have been studied as CO_2 and CH_4 adsorbents at 0 °C. For both gases, the adsorption capacity of Ni(BDP) is higher than that of Zn(BDP), reaching 10.0 mmol CO_2/g and 3.7 mmol CH_4/g for Ni(BDP) and 9.1 mmol CO_2/g and 2.4 mmol CH_4/g for Zn(BDP) at p = 30 bar. This is in contrast with the specific surface areas trend, suggesting the existence of framework breathing in the case of Ni(BDP), as frequently found for MOFs sharing the same structural motif.[151] Together with HKUST-1,[152] the two MOFs were also evaluated in the removal of thiophene (~30 ppm) from a $He:CH_4:CO_2$ 1:2.25:1 (v:v.v) flow in both dry and humid conditions. The results showed that the M(BDP) MOFs are suitable for the selective capture of thiophene in dynamic conditions also in the presence of water vapours, at odds with HKUST-1. As a development of this research line, to disclose the role of the different functionalities in the linker skeleton, the M(BDPX) isoreticular series (M = Ni, Zn; X = H, NO_2, NH_2, OH, SO_3H)[25] was exploited for binary mixtures selective separation. The study was performed combining single-component adsorption isotherms, pulse gas chromatography and breakthrough curve measurements. Overall, functionalization does improve the

separation of probes with highly different polarities (N_2/CO_2 or CH_4/CO_2), while is not effective in the separation of gases with similar quadrupole moments (CO_2/C_2H_2).

4.2 Heterogeneous catalysis: CO_2 valorization, hydrocarbon/water oxidation and photocatalysis

Heterogeneous catalysis in MOFs is an important applicative field that is gaining increasing attention among the MOF community. The tailored design of MOFs coming from a judicious choice of nodes and linkers is extremely helpful in the creation of performing catalysts for a specific reaction of interest. Many ideas and experimental results collected in the past on single-site molecular metal-based catalysts (organometallic/coordination compounds) can be put to good use and extended to MOFs, because the latter can be considered a "3D-extended" version of the former, with a "plus" that is given by the presence of a porous crystalline scaffold that forces the catalysis to occur in a confined portion of space. This often deeply modifies the catalytic outcomes with respect to a homogeneous process. The proper linker functionalization with reactive tags or the facile creation of reactive open metal sites are other striking features of MOFs as catalysts. Finally, the discovery of MIXMOFs (MOFs made of more than one metal type or linker type together in the same solid phase) opens infinite horizons for their exploitation as heterogeneous catalysts. A few examples are discussed in this Section.

4.2.1 Alkanes and alkenes oxidation (Firenze, Como, Camerino)

The Firenze team has exploited the activated MOF Co(L-*RR*) (Fig. 5) as heterogeneous alkenes oxidation catalyst using hydroperoxides (ROOH) or molecular oxygen (O_2) as oxidants.[153] In this MOF, one open metal site is generated after water removal from the metal coordination sphere. The vacant site can interact with selected cyclic/linear olefins (cyclohexene, *Z*-cyclooctene, 1-octene) to promote their oxidation under relatively mild conditions (T = 70 °C, 24 h, p_{O2} = 5 bar) with satisfactory conversions and selectivities. A moderate chiral induction was observed in selected

(prochiral) substrates, given the intrinsic MOF chirality. The interaction of O_2 with the vacant coordination site on cobalt has been analysed in detail through a DFT study in the solid state. The collected computational results are all consistent with the existence of a Co(η^1-superoxo-O_2) complex. The calculated O_2 adsorption energy is in good agreement with the experimental value coming from temperature-programmed O_2 desorption analysis (TPD). In 2015, the Camerino and Como teams reported a study concerning the catalytic activity of the polymers M(Me_4BDP) (M = Cd, Co, Cu, Zn) towards the solventless oxidation of 1-phenylethanol and cyclohexane using peroxides as oxidants and assisted by microwave irradiation under mild conditions (Scheme 2).[24] The copper-containing compound showed the highest efficiency in both reactions, leading selectively to a maximum product yield of 92% (and TON up to 1.5×10^3) in the oxidation of 1-phenylethanol and of 11% in the oxidation of cyclohexane, which is higher than that granted by the current industrial process.

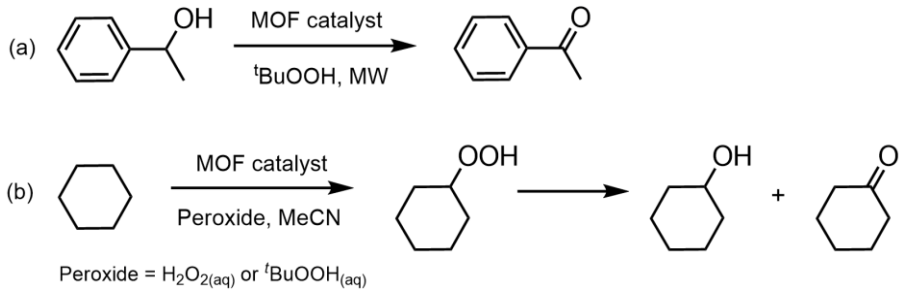

Scheme 2. (a) MW-assisted, solvent-free oxidation of 1-phenylethanol to acetophenone, 80-120 °C. (b) Peroxidative oxidation of cyclohexane, r.t. or 50 °C.

In one of the latest joint works,[154] the Camerino, Como and Firenze research groups employed the isostructural MOFs Co(BPZX) (X = H, NH_2, NO_2) with linkers bearing different chemical tags (Table 1) as heterogeneous catalysts for aerobic liquid-phase oxidation of cumene with O_2 (Scheme 3).

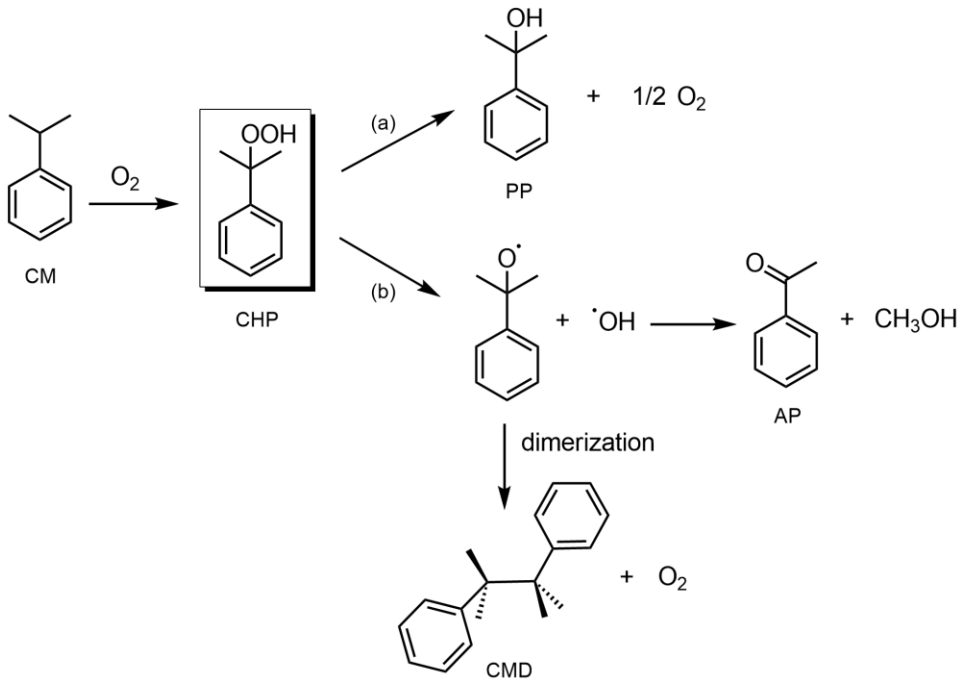

Scheme 3. Cumene oxidation to CHP and its further oxidation to 2-Phenyl-2-propanol (PP) and Acetophenone (AP).

The selectivity towards cumene oxidation products depends on the chemical nature of the functional group decorating the channel cavities. In fact, while cumene hydroperoxide (CHP) is the main product obtained with Co(BPZ) (84% selectivity to CHP), further oxidation to 2-phenyl-2-propanol (PP) is observed in the presence of Co(BPZNH$_2$) as the catalyst (69% selectivity to PP). This study shows that Co(BPZNH$_2$) is a good candidate for the production of 2-phenyl-2-propanol as a major product. This result, to our knowledge, seems to be the first case in which pyrazolate-based MOFs are used for the catalysis of cumene oxidation. The study also highlights an unusual selectivity dependent on the type of substituent, never observed before in a MOF.

4.2.2 CO_2 valorization (Firenze, Como, Camerino)

CO_2 valorization through its conversion into useful chemical feedstock (Carbon Capture and Utilization, CCU) is a hot topic in contemporary chemistry research Worldwide. In CCU, CO_2 is an

abundant, non-flammable and harmless inexpensive C_1 synthon that is taken as starting reagent to produce other C_n products and industrial feedstock of added value like formic acid, methanol, ethanol, methane and carbonates. To date, a number of catalytic processes that use CO_2 as substrate are studied by the international chemical community. One of the simplest and most popular is its addition to epoxides to form cyclic carbonates (epoxidation, Scheme 4). Carbonates are green, aprotic, polar and high-boiling solvents; they are also used as precursors for polyurethanes and polycarbonates.

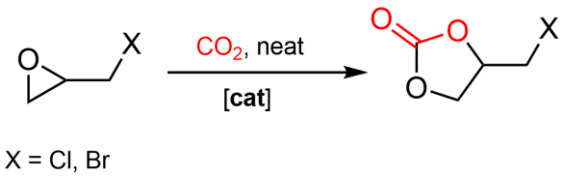

Scheme 4. CO_2 epoxidation to produce cyclic carbonates.

The Firenze team has exploited the bithiazole MOF $[Zr_6O_4(OH)_4(TzTz)_6]$ ($TzTz^{2-}$ = 2,2'-bithiazole-5,5'-dicarboxylate, Fig. 7) as heterogeneous CO_2 epoxidation catalyst under green conditions. The substrates of choice were activated epoxides with a $–CH_2X$ substituent (X = Cl: epichlorohydrin; X = Br: epibromohydrin). The highest conversion recorded was 74% for epibromohydrin transformation into its cyclic carbonate at p_{CO2} = 1 bar and T = 120 °C.[46] Another successful example of CCU catalyst is the MOF $Zn(BPZNH_2)$.[28] In view of its capacity and affinity *vs*. CO_2, it was tested as heterogeneous catalyst in the same reaction and conditions as above. At T = 120 °C and p_{CO2} = 1 bar, $Zn(BPZNH_2)$ converts 47% of epibromohydrin, with a TOF of 3.9 mmol(carbonate) $(mmolZn)^{-1}$ h^{-1}.

4.2.3 Photocatalysis (Perugia, Pisa)

In a recent theoretical paper,[155] Ce^{IV}-MOFs were investigated for their potential photocatalytic applications. Cerium has low-energy-lying partially empty 4*f* orbitals that stabilize long-life charge separation states induced by linker-to-metal charge transfer (LMCT) upon UV light irradiation. Due

to the light absorption properties and high redox potential of Ce^{IV}, the Ce-MOFs prepared in Perugia (Fig. 16) were tested for the photo-oxidation reaction of substituted benzylic alcohols to the corresponding aldehydes, using near-UV light ($\lambda = 355$ nm) and in the presence of molecular oxygen. The substrate used for testing the catalytic efficiency was 4-methoxy benzylic alcohol (Scheme 5).[95]

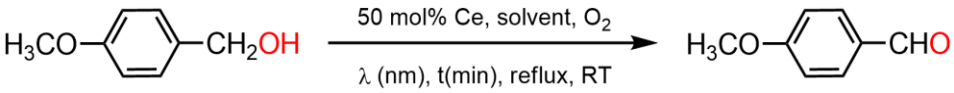

Scheme 5. Photo-oxidation of 4-methoxy benzylic alcohol to 4-methoxy benzaldehyde catalyzed by Ce-MOFs.

Reactions were carried out in ethanol as solvent at ambient temperature. The effect of the dangling group on the terephthalate linker was examined by taking into account the conversion yield and time. The best performing MOF was Ce-UiO-66-PDC, with pyridine-2,5-dicarboxylic acid as linker. The catalyst (with a band-gap of 2.70 eV calculated on the absorption onset) was able to convert into aldehyde more than 96% of starting alcohol within 75 min of irradiation. The effect of band-gap was interpreted by considering also the LMCT level, responsible for the charge-separation state lifetime. When Ce-MOFs are photoexcited, the photogenerated electrons undergo LMCT to form charge-separated states, thus preventing the rapid recombination of the photogenerated charges. The kinetics of this process depend on the LMCT energy, E_{LMCT}, which is defined as the energy change upon transferring the photogenerated electron from the photoexcited linker orbital to the lowest unoccupied metal orbital. The substituents on the linker have a great influence both on the MOF oxidative ability and on the efficiency of separating the photogenerated charges. In particular, the less electron-withdrawing the linker substituent (*i.e.* the more favored the electron-hole separation), the more negative the E_{LMCT} value. Accordingly, also the electron-hole recombination rate (the competitive reaction with the photo-oxidation) will slow down. In general, the reactivity was found to have an opposite trend with respect to the oxidative potential of the used BDC linkers.

4.3 Other applications

4.3.1 Luminescence sensing (Firenze)

Among the various MOF families, that of luminescent MOFs is rapidly growing in terms of interest and investigation efforts. The nature of MOFs building blocks invariably dictates their luminescence properties. Numerous MOFs or CPs contain unsaturated organic linkers showing intrinsic luminescence, due to intraligand $n \rightarrow \pi^*$ or $\pi \rightarrow \pi^*$ electronic excitation with an appropriate wavelength. When the constituting transition metal center has a closed-shell electronic configuration (like d^0 or d^{10}), the emission is exclusively coming from the organic linker. Modifications in luminescence properties can be triggered by guest molecules adsorption in MOFs pores or capture by a CP. Luminescence intensity, wavelength and/or lifetime are the parameters that can vary upon guest inclusion. Thiazoles are intrinsically luminescent and suitable to build luminescent MOFs or CPs.[156] In Firenze, the NU-1000-BzTz MOF has been exploited for the luminescence sensing of cyanide, cyanate, thiocyanate and selenocyanate anions in water. The easy bromide $\leftrightarrow$ polluting anion exchange occurring when the MOF is suspended in water induces a remarkable and *reversible* blue shift of its emission band from 490 to 450 nm in all cases, with the associated emission color change from light green to blue under a UV lamp (Fig. 33). The detection limit of CN^- (1.08×10^{-6} M) is particularly low, and the process occurs efficiently even in the presence of other competing ions (*i.e.* in ordinary tap water), opening promising application perspectives in cyanide luminescent sensing in drinking water.

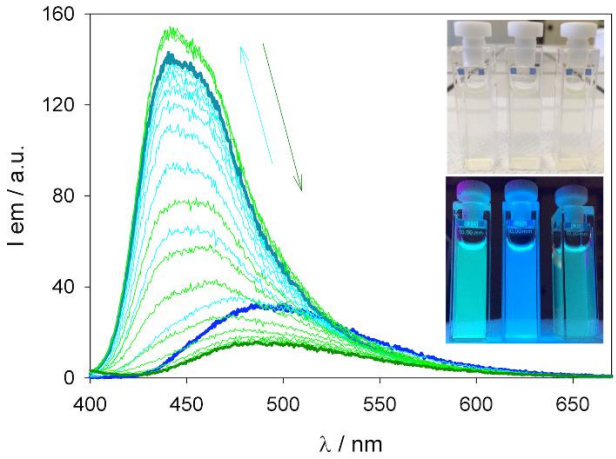

Fig. 33. Evolution of the emission spectra recorded for a suspension of NU-1000-BzTz upon additions of KCN (from 0 to *ca*. 0.33 mM, blue to turquoise line, respectively) in H_2O at r.t. followed by additions of $Ag(CF_3SO_3)$ (up to *ca*. 1.3 mM, dark green line). λ_{ex}=385 nm; 0.25 < A_{385nm} < 0.44. Inset: photos taken on three suspensions of NU-1000-BzTz in pure water (left), 0.5 mM KCN (centre) and 0.5 mM KCN plus excess of $Ag(CF_3SO_3)$ (right), under ambient light (top) and under UV excitation (bottom). Adapted from ref.[47]. Published by The Royal Society of Chemistry.

4.3.2 Magnetic properties and magnetocaloric effect (Firenze)

Hybrid materials that have a strong response to external magnetic fields normally contain paramagnetic metal ions or/and open-shell organic linkers. Lanthanides are the ideal choice in this context, exhibiting very large magnetic moments and very strong magnetic anisotropy in some cases. Lanthanide-Organic Frameworks (LOFs) are numerous in the MOFs database. The high coordination versatility (in terms of both coordination number and geometry) of rare Earths is well-documented; this leads to assorted LOFs with variable topology and inner surface areas. Given the high lanthanides oxophilicity stemming from high ionic charge (*hard* acids), carboxylic acids are the organic spacers *par excellence* in LOFs construction. However, a short connection between the metal ions is necessary to maximize their magnetic communication in the solid polymeric matrix. With this concept in mind, the Firenze group studied the magnetic behavior of the lanthanide formates $(Fmd)Ln^{III}(HCOO)_4$ (Ln = Gd, Dy, Fig. 9).[55] Formic acid is the shortest carboxylic acid conceivable; it has been found to transmit a weak antiferromagnetic interaction between Ln^{III} centers

only in the case of gadolinium. Another important emerging application of magnetic materials is the Magnetocaloric Effect (MCE). MCE is a magneto-thermodynamic phenomenon in which the temperature changes of a (magnetically responsive) material are caused by exposing it to a changing magnetic field. This is also known as adiabatic demagnetization. When the externally applied magnetic field is removed, the magnetic domains present in a magnetocaloric material lose their parallel orientation to the external field using thermal energy. If the process is adiabatic (*i.e*. the material is isolated and no external energy is absorbed during this spin re-orientation), the temperature drops as the domains absorb their own thermal energy to go back to their initial magnetic state. One of the most notable examples of the magnetocaloric effect is in gadolinium and some of its alloys. The ideal materials for practical applications in magnetic refrigeration devices should have a magnetic phase transition temperature near the temperature region of interest (normally room temperature for domestic refrigerators). In the ideal LOF material for magnetocaloric cooling, the spatial density of the magnetic centers should be maximized, reducing as much as possible the amount of non-magnetic elements between them. Hence, the need of employing short lightweight linkers like formate. Following this idea, the magnetocaloric features of polymeric gadolinium formate $Gd(HCOO)_3$ were examined in 2013.[157] Gadolinium formate is a dense MOF, characterized by a relatively high packing density of Gd^{III} ions (Fig. 34a). Our magnetic and thermal studies showed that $Gd(HCOO)_3$ is indeed featured by a huge MCE. A maximum variation of the magnetic entropy ($-\Delta S_m$) of *ca.* 168.5 and 215.7 mJ cm^{-3} K^{-1} was recorded for a change of the external field (ΔB) of (2 − 0) T and (7 − 0) T, respectively (Fig. 34b).

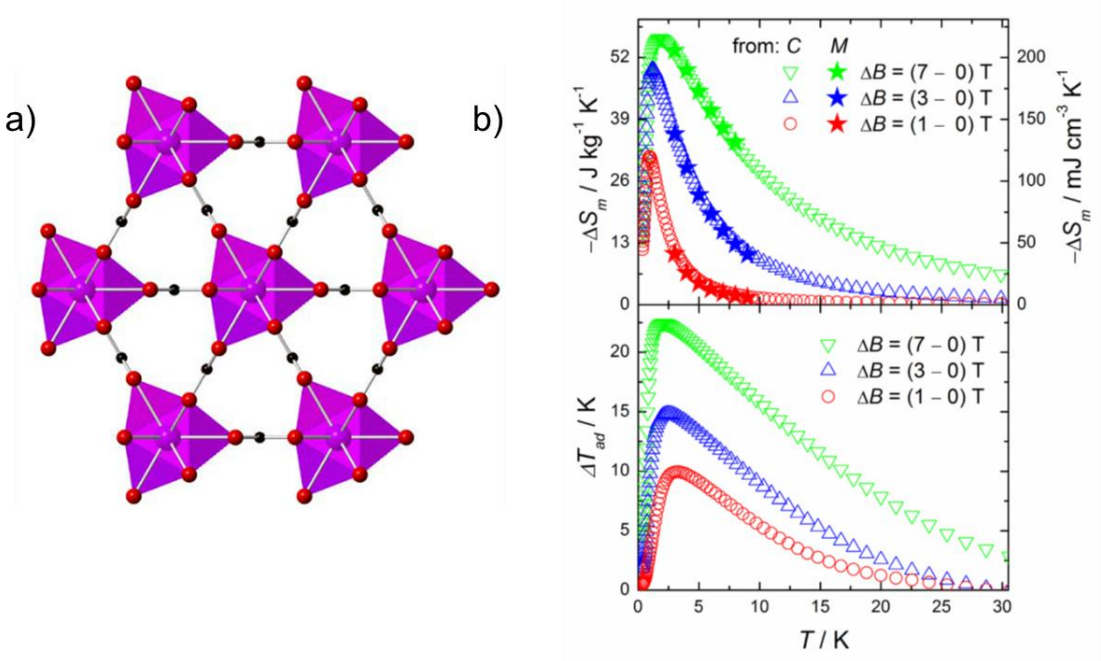

Fig. 34. (a) Portion of the crystal structure of $Gd(HCOO)_3$. Color code: Gd, purple, O, red, C, black. Hydrogen atoms omitted for clarity. The nine-coordinate tricapped trigonal prism coordination sphere of Gd^{III} ions is highlighted. (b) Top: temperature-dependence of the magnetic entropy change ΔS_m, as obtained from magnetization and heat capacity data for the indicated applied-field changes ΔB. Bottom: temperature-dependence of the adiabatic temperature change ΔT_{ad}, as obtained from heat capacity data for the indicated ΔB. Adapted with permission from ref.[157], John Wiley & Sons.

Conclusions and Perspectives

The chemistry of MOFs is still largely unexplored, and given the infinite possibilities to build crystalline architectures with peculiar applicative properties, there is still a lot to do and discover in this field. Italian groups have set a mature investigation on MOFs, each one with a specific flavor, but new and possibly unexpected outcomes are waiting for them and for their new collaborative activities. We are all looking forward to making this dream come true in the years to come.

Conflicts of Interest. The authors have no conflicts of interest to declare.

ORCID

Andrea Rossin: 0000-0002-1283-2803

Simona Galli: 0000-0003-0335-5707

Giuliano Giambastiani: 0000-0002-0315-3286

Claudio Pettinari: 0000-0002-2547-7206

Corrado Di Nicola: 0000-0002-0958-6103

Rebecca Vismara: 0000-0001-9474-7671

Ferdinando Costantino: 0000-0002-2120-1456

Marco Taddei: 0000-0003-2805-6375

Cesare Atzori: 0000-0002-3227-7421

Francesca Carla Bonino: 0000-0002-6822-6685

Bartolomeo Civalleri: 0000-0003-3198-3161

Silvia Bordiga: 0000-0003-2371-4156

Riccardo Vivani: 0000-0001-9666-2997

Acknowledgments

Current investigation in MOFs in Italy is sponsored by the FIRB2017 and AMIS projects, "Dipartimenti di Eccellenza -2018-2022", Università di Perugia. A.R. and G.G. would like to thank the Italian MIUR through the PRIN 2017 project MULTI-e (20179337R7) "Multielectron transfer for the conversion of small molecules: an enabling technology for the chemical use of renewable energy" and the TRAINER project "Catalysts for Transition to Renewable Energy Future" (Ref. ANR-17-MPGA-0017) for financial support.

References

[1] J.D. Evans, B. Garai, H. Reinsch, W. Li, S. Dissegna, V. Bon, I. Senkovska, R.A. Fischer, S. Kaskel, C. Janiak, N. Stock, D. Volkmer, Coord. Chem. Rev., 380 (2019) 378-418.

[2] S. Bordiga, C. Lamberti, G. Ricchiardi, L. Regli, F. Bonino, A. Damin, K.P. Lillerud, M. Bjorgen, A. Zecchina, Chem. Commun., (2004) 2300-2301.

[3] R. Dovesi, A. Erba, R. Orlando, C.M. Zicovich-Wilson, B. Civalleri, L. Maschio, M. Rérat, S. Casassa, J. Baima, S. Salustro, B. Kirtman, WIREs Comput Mol Sci. , 8 (2018) e1360.

[4] B. Civalleri, F. Napoli, Y. Noel, C. Roetti, R. Dovesi, CrystEngComm, 8 (2006) 364-371.

[5] C. Pettinari, A. Tăbăcaru, S. Galli, Coord. Chem. Rev., 307 (2016) 1-31.

[6] J.-P. Zhang, Y.-B. Zhang, J.-B. Lin, X.-M. Chen, Chem. Rev., 112 (2012) 1001-1033.

[7] A. Demessence, D.M. D'Alessandro, M.L. Foo, J.R. Long, J. Am. Chem. Soc., 131 (2009) 8784-8786.

[8] Y.-Q. Tian, Y.-M. Zhao, Z.-X. Chen, G.-N. Zhang, L.-H. Weng, D.-Y. Zhao, Chem. Eur. J., 13 (2007) 4146-4154.

[9] K.S. Park, Z. Ni, A.P. Coté, J.Y. Choi, R. Huang, F.J. Uribe-Romo, H.K. Chae, M. O'Keeffe, O.M. Yaghi, Proc. Nat. Acad. Sci., 103 (2006) 10186-10191.

[10] X.-C. Huang, Y.-Y. Lin, J.-P. Zhang, X.-M. Chen, Angew. Chem. Int. Ed., 45 (2006) 1557-1559.

[11] J.J. Low, A.I. Benin, P. Jakubczak, J.F. Abrahamian, S.A. Faheem, R.R. Willis, J. Am. Chem. Soc., 131 (2009) 15834-15842.

[12] S.S. Kaye, A. Dailly, O.M. Yaghi, J.R. Long, J. Am. Chem. Soc., 129 (2007) 14176-14177.

[13] J.A. Greathouse, M.D. Allendorf, J. Am. Chem. Soc., 128 (2006) 10678-10679.

[14] J. Catalan, J. Elguero, Adv. Heterocycl. Chem., 41 (1987) 187-274.

[15] A.J. Howarth, Y. Liu, P. Li, Z. Li, T.C. Wang, J.T. Hupp, O.K. Farha, Nat. Rev. Mater., 1 (2016) 15018.

[16] A. Tăbăcaru, C. Pettinari, S. Galli, Coord. Chem. Rev., 372 (2018) 1-30.

[17] H. Zhao, Z.-R. Qu, H.-Y. Ye, R.-G. Xiong, Chem. Soc. Rev., 37 (2008) 84-100.

[18] C. Pettinari, A. Tăbăcaru, I. Boldog, K.V. Domasevitch, S. Galli, N. Masciocchi, Inorg. Chem., 51 (2012) 5235-5245.

[19] S. Galli, N. Masciocchi, V. Colombo, A. Maspero, G. Palmisano, F.J. Lopez-Garzon, M. Domingo-Garcia, I. Fernandez-Morales, E. Barea, J.A.R. Navarro, Chem. Mater., 22 (2010) 1664-1672.

[20] S. Galli, A. Maspero, C. Giacobbe, G. Palmisano, L. Nardo, A. Comotti, I. Bassanetti, P. Sozzani, N. Masciocchi, J. Mater. Chem. A, 2 (2014) 12208-12221.

[21] N. Mosca, R. Vismara, J.A. Fernandes, S. Casassa, K.V. Domasevitch, E. Bailón-García, F.J. Maldonado-Hódar, C. Pettinari, S. Galli, Cryst. Growth Des., 17 (2017) 3854-3867.

[22] A. Taďačaru, C. Pettinari, I. Timokhin, F. Marchetti, F. Carrasco-Marin, F.J. Maldonado-Hodar, S. Galli, N. Masciocchi, Cryst. Growth Des., 13 (2013) 3087-3097.

[23] J. Baima, R. Macchieraldo, C. Pettinari, S. Casassa, CrystEngComm, 17 (2015) 448-455.

[24] I. Timokhin, C. Pettinari, F. Marchetti, R. Pettinari, F. Condello, S. Galli, E. Alegria, L. Martins, A.J.L. Pombeiro, Cryst. Growth Des., 15 (2015) 2303-2317.

[25] V. Colombo, C. Montoro, A. Maspero, G. Palmisano, N. Masciocchi, S. Galli, E. Barea, J.A.R. Navarro, J Am. Chem. Soc. , 134 (2012) 12830-12843.

[26] S. Bracco, F. Castiglioni, A. Comotti, S. Galli, M. Negroni, A. Maspero, P. Sozzani, Chem. Eur. J., 23 (2017) 11210-11215.

[27] N. Mosca, R. Vismara, J.A. Fernandes, G. Tuci, C. Di Nicola, K.V. Domasevitch, C. Giacobbe, G. Giambastiani, C. Pettinari, M. Aragones-Anglada, P.Z. Moghadam, D. Fairen-Jimenez, A. Rossin, S. Galli, Chem.-Eur. J., 24 (2018) 13170-13180.

[28] R. Vismara, G. Tuci, N. Mosca, K.V. Domasevitch, C. Di Nicola, C. Pettinari, G. Giambastiani, S. Galli, A. Rossin, Inorg. Chem. Front., 6 (2019) 533-545.

[29] R. Vismara, C. Di Nicola, R. Gil-San Millán, K.V. Domasevich, C. Pettinari, J.A.R. Navarro, S. Galli, Nano Res., (2020).

[30] V. Colombo, S. Galli, H.J. Choi, G.D. Han, A. Maspero, G. Palmisano, N. Masciocchi, J.R. Long, Chem. Sci., 2 (2011) 1311-1319.

[31] A. Tăbăcaru, S. Galli, C. Pettinari, N. Masciocchi, T.M. McDonald, J.R. Long, CrystEngComm, 17 (2015) 4992-5001.

[32] I. Timokhin, J. Baguña Torres, A.J.P. White, P.D. Lickiss, C. Pettinari, R.P. Davies, Dalton Trans., 42 (2013) 13806-13808.

[33] I. Timokhin, A.J.P. White, P.D. Lickiss, C. Pettinari, R.P. Davies, CrystEngComm, 16 (2014) 8094-8097.

[34] I. Boldog, J. Sieler, A.N. Chernega, K.V. Domasevitch, Inorg. Chim. Acta, 338 (2002) 69-77.

[35] Q.-F. Sun, K.M.-C. Wong, L.-X. Liu, H.-P. Huang, S.-Y. Yu, V.W.-W. Yam, Y.-Z. Li, Y.-J. Pan, K.-C. Yu, Inorg. Chem., 47 (2008) 2142-2154.

[36] A. Maspero, S. Galli, N. Masciocchi, G. Palmisano, Chem. Lett., 37 (2008) 956-957.

[37] A.V. Sharko, G.A. Senchyk, E.B. Rusanov, K.V. Domasevitch, Tetrahedron Lett., 56 (2015) 6089-6092.

[38] W.L. Mosby, J. Chem. Soc., (1957) 3997-4003.

[39] S.-H. Li, H.-P. Huang, S.-Y. Yu, X.-P. Li, Chin. J. Chem., 24 (2006) 1225-1229.

[40] J. Angbrant, E. Homan, T. Lundbaek, J. Martinsson, M. Sari, M. Joensson, K. Faernegaardh, K. Hallber,WO2011161201,2011,K. AB,Sweden

[41] P. Cui, Y.-G. Ma, H.-H. Li, B. Zhao, J.-R. Li, P. Cheng, P.B. Balbuena, H.-C. Zhou, J. Am. Chem. Soc., 134 (2012) 18892-18895.

[42] S. Zhang, Q. Yang, X. Liu, X. Qu, Q. Wei, G. Xie, S. Chen, S. Gao, Coord. Chem. Rev., 307 (2016) 292-312.

[43] A.K. Franz, S.O. Wilson, J. Med. Chem., 56 (2013) 388-405.

[44] A. Rossin, B. Di Credico, G. Giambastiani, A. Peruzzini, G. Pescitelli, G. Reginato, E. Borfecchia, D. Gianolio, C. Lamberti, S. Bordiga, J. Mater. Chem. , 22 (2012) 10335-10344.

[45] A. Rossin, G. Tuci, G. Giambastiani, M. Peruzzini, ChemPlusChem, 79 (2014) 406-412.

[46] P. Müller, B. Bucior, G. Tuci, L. Luconi, J. Getzschmann, S. Kaskel, R.Q. Snurr, G. Giambastiani, A. Rossin, Mol. Syst. Des. Eng., 4 (2019) 1000-1013.

[47] L. Luconi, G. Mercuri, T. Islamoglu, A. Fermi, G. Bergamini, G. Giambastiani, A. Rossin, J. Mater. Chem. C, 8 (2020) 7492-7500.

[48] B. Di Credico, G. Reginato, L. Gonsalvi, M. Peruzzini, A. Rossin, Tetrahedron, 67 (2011) 267-274.

[49] A. Rossin, B. Di Credico, G. Giambastiani, L. Gonsalvi, M. Peruzzini, G. Reginato, Eur. J. Inorg. Chem., (2011) 539-548.

[50] J.H. Cavka, S. Jakobsen, U. Olsbye, N. Guillou, C. Lamberti, S. Bordiga, K.P. Lillerud, J. Am. Chem. Soc., 130 (2008) 13850-13851.

[51] M. Yoon, D. Moon, Microp. Mesop. Mater., 215 (2015) 116-122.

[52] A. Rossin, A. Ienco, F. Costantino, T. Montini, B. Di Credico, M. Caporali, L. Gonsalvi, P. Fornasiero, M. Peruzzini, Cryst. Growth Des., 8 (2008) 3302-3308.

[53] A. Rossin, D. Fairen-Jimenez, T. Düren, G. Giambastiani, M. Peruzzini, J.G. Vitillo, Langmuir, 27 (2011) 10124-10131.

[54] A. Rossin, M.R. Chierotti, G. Giambastiani, R. Gobetto, M. Peruzzini, CrystEngComm, 14 (2012) 4454-4460.

[55] A. Rossin, G. Giambastiani, M. Peruzzini, R. Sessoli, Inorg. Chem., 51 (2012) 6962-6968.

[56] G. Alberti, E. Brunet, C. Dionigi, O. Juanes, M.J. de la Mata, J.C. Rodríguez-Ubis, R. Vivani, Angew. Chem. Int. Ed., 38 (1999) 3351-3353.

[57] G. Alberti, F. Marmottini, S. Murcia-Mascarós, R. Vivani, Angew. Chem. Int. Ed., 33 (1994) 1594-1597.

[58] G. Alberti, U. Costantino, F. Marmottini, R. Vivani, P. Zappelli, Angew. Chem. Int. Ed., 32 (1993) 1357-1359.

[59] G. Alberti, M. Casciola, U. Costantino, R. Vivani, Adv. Mater., 8 (1996) 291-303.

[60] G. Alberti, S. Murcia-Mascarós, R. Vivani, J. Am. Chem. Soc., 120 (1998) 9291-9295.

[61] S. Kitagawa, K. Uemura, Chem. Soc. Rev. , 34 (2005) 109-119.

[62] M. Taddei, P. Sassi, F. Costantino, R. Vivani, Inorg. Chem., 55 (2016) 6278-6285.

[63] M. Taddei, R. Vivani, F. Costantino, Dalton Trans., 42 (2013) 9671-9678.

[64] M. Taddei, A. Donnadio, F. Costantino, R. Vivani, M. Casciola, Inorg. Chem., 52 (2013) 12131-12139.

[65] R. Vivani, F. Costantino, M. Nocchetti, G.D. Gatta, J. Solid State Chem., 177 (2004) 4013-4022.

[66] R. Vivani, U. Costantino, M. Nocchetti, J. Mater. Chem., 12 (2002) 3254-3260.

[67] U. Costantino, M. Nocchetti, R. Vivani, J. Am. Chem. Soc., 124 (2002) 8428-8434.

[68] R. Vivani, F. Costantino, U. Costantino, M. Nocchetti, Inorg. Chem., 45 (2006) 2388-2390.

[69] M. Taddei, F. Costantino, A. Ienco, A. Comotti, P.V. Dau, S.M. Cohen, Chem. Commun., 49 (2013) 1315-1317.

[70] F. Costantino, A. Donnadio, M. Casciola, Inorg. Chem., 51 (2012) 6992-7000.

[71] M. Taddei, F. Costantino, R. Vivani, Inorg. Chem., 49 (2010) 9664-9670.

[72] M. Taddei, F. Costantino, R. Vivani, S. Sabatini, S.-H. Lim, S.M. Cohen, Chem. Commun., 50 (2014) 5737-5740.

[73] M. Taddei, F. Costantino, F. Marmottini, A. Comotti, P. Sozzani, R. Vivani, Chem. Commun., 50 (2014) 14831-14834.

[74] M. Taddei, S.J.I. Shearan, A. Donnadio, M. Casciola, R. Vivani, F. Costantino, Dalton Trans., 49 (2020) 3662-3666.

[75] W. Ouellette, G. Wang, H. Liu, G.T. Yee, C.J. O'Connor, J. Zubieta, Inorg. Chem., 48 (2009) 953-963.

[76] R. Vaidhyanathan, A.H. Mahmoudkhani, G.K.H. Shimizu, Can. J. Chem., 87 (2009) 247-253.

[77] F. Costantino, T. Bataille, N. Audebrand, E. Le Fur, C. Sangregorio, Cryst. Growth Des., 7 (2007) 1881-1888.

[78] M. Taddei, F. Costantino, R. Vivani, C. Sangregorio, L. Sorace, L. Castelli, Cryst. Growth Des., 12 (2012) 2327-2335.

[79] K.T. Leperi, Y.G. Chung, F. You, R.Q. Snurr, ACS Sustainable Chem. Eng., 7 (2019) 11529-11539.

[80] V. Sridharan, J.C. Menéndez, Chem. Rev., 110 (2010) 3805-3849.

[81] T. Montini, M. Melchionna, M. Monai, P. Fornasiero, Chem. Rev., 116 (2016) 5987-6041.

[82] R.D. Shannon, C.T. Prewitt, Acta Cryst., B26 (1970) 1046-1048.

[83] M. Lammert, C. Glißmann, H. Reinsch, N. Stock, Cryst. Growth Des., 17 (2017) 1125-1131.

[84] M. Lammert, M.T. Wharmby, S. Smolders, B. Bueken, A. Lieb, K.A. Lomachenko, D. De Vos, N. Stock, Chem. Commun., 51 (2015) 12578-12581.

[85] J. Ethiraj, F. Bonino, J.G. Vitillo, K.A. Lomachenko, C. Lamberti, H. Reinsch, K.P. Lillerud, S. Bordiga, ChemSusChem, 9 (2016) 713-719.

[86] N.L. Rosi, J. Kim, M. Eddaoudi, B. Chen, M. O'Keeffe, O.M. Yaghi, J. Am. Chem. Soc., 127 (2005) 1504-1518.

[87] C. Atzori, K.A. Lomachenko, S. Øien-Ødegaard, C. Lamberti, N. Stock, C. Barolo, F. Bonino, Cryst. Growth Des., 19 (2019) 787-796.

[88] C. Atzori, J. Ethiraj, V. Colombo, F. Bonino, S. Bordiga, Inorganics, 8 (2020) 9.

[89] A. Airi, C. Atzori, F. Bonino, A. Damin, S. Øien-Ødegaard, E. Aunan, S. Bordiga, Dalton Trans., 49 (2020) 12-16.

[90] N. Stock, Micropor. Mesopor. Mat., 129 (2010) 287-295.

[91] L. D'Arras, C. Sassoye, L. Rozes, C. Sanchez, J. Marrot, S. Marre, C. Aymonier, New J. Chem., 38 (2014) 1477-1483.

[92] R. D'Amato, A. Donnadio, M. Carta, C. Sangregorio, D. Tiana, R. Vivani, M. Taddei, F. Costantino, ACS Sustainable Chem. Eng., 7 (2019) 394-402.

[93] V. Guillerm, F. Ragon, M. Dan-Hardi, T. Devic, M. Vishnuvarthan, B. Campo, A. Vimont, G. Clet, Q. Yang, G. Maurin, G. Férey, A. Vittadini, S. Gross, C. Serre, Angew. Chem. Int. Ed., 51 (2012) 9267-9271.

[94] A. Buragohain, S. Biswas, CrystEngComm, 18 (2016) 4374-4381.

[95] M. Campanelli, T. Del Giacco, F. De Angelis, E. Mosconi, M. Taddei, F. Marmottini, R. D'Amato, F. Costantino, ACS Appl. Mater. Interfaces, 11 (2019) 45031-45037.

[96] N. Masciocchi, S. Galli, A. Sironi, X-Ray Powder Diffraction Characterization of Polymeric Metal Diazolates, in: J.P. Fackler Jr., L.R. Falvello (Eds.) Techniques in Inorganic Chemistry, CRC Press, 2010.

[97] J.A.R. Navarro, E. Barea, A. Rodriguez-Dieguez, J.M. Salas, C.O. Ania, J.B. Parra, N. Masciocchi, S. Galli, A. Sironi, J. Am. Chem. Soc., 130 (2008) 3978-3984.

[98] C. Giacobbe, E. Lavigna, A. Maspero, S. Galli, J. Mater. Chem. A, 5 (2017) 16964-16975.

[99] S.S. Han, D. Kim, D.H. Jung, S. Cho, S.-H. Choi, Y.J. Jung, J. Phys. Chem. C, 116 (2012) 20254-20261.

[100] R. Vaidhyanathan, S.S. Iremonger, G.K.H. Shimizu, P.G. Boyd, S. Alavi, T.K. Woo, Science, 330 (2010) 650-653.

[101] M.A. Soldatov, A. Martini, A.L. Bugaev, I. Pankin, P.V. Medvedev, A.A. Guda, A.M. Aboraia, Y.S. Podkovyrina, A.P. Budnyk, A.A. Soldatov, C. Lamberti, Polyhedron, 155 (2018) 232-253.

[102] N. Masciocchi, S. Galli, V. Colombo, A. Maspero, G. Palmisano, B. Seyyedi, C. Lamberti, S. Bordiga, J. Am. Chem. Soc., 132 (2010) 7902-7904.

[103] F. Bonino, C. Lamberti, S. Bordiga, IR and Raman Spectroscopies Probing MOFs Structure, Defectivity and Reactivity, in: S. Kaskel (Ed.) The Chemistry of Metal–Organic Frameworks: Synthesis, Characterization and Applications, Wiley-VCH, 2016, pp. 657-690.

[104] F. Bonino, C. Lamberti, S. Chavan, J.G. Vitillo, S. Bordiga, Characterization of MOFs. 1. Combined Vibrational and Electronic Spectroscopies, in: F. Llabres i Xamena, J. Gascon (Eds.) Metal Organic Frameworks as Heterogeneous Catalysts, Royal Society of Chemistry, Cambridge, 2013, pp. 76-142.

[105] L. Mino, V. Colombo, J.G. Vitillo, C. Lamberti, S. Bordiga, E. Gallo, P. Glatzel, A. Maspero, S. Galli, Dalton Trans., 41 (2012) 4012-4019.

[106] K. Sumida, D.L. Rogow, J.A. Mason, T.M. McDonald, E.D. Bloch, Z.R. Herm, T.-H. Bae, J.R. Long, Chem. Rev., 112 (2012) 724-781.

[107] Metal Organic Frameworks as Heterogeneous Catalysts, F. Llabrés i Xamena, J. Gascon (Eds.), Royal Society of Chemistry, Cambridge, 2013.

[108] M.-X. Wu, Y.-W. Yang, Adv. Mater., 23 (2017) 1606134.

[109] M. Thommes, K. Kaneko, A.V. Neimark, J.P. Olivier, F. Rodriguez-Reinoso, J. Rouquerol, K.S.W. Sing, Pure Appl. Chem., 87 (2015) 1051-1069.

[110] V. Solinas, I. Ferino, Catal. Today, 41 (1998) 179-189.

[111] A. Masala, J.G. Vitillo, G. Mondino, C.A. Grande, R. Blom, M. Manzoli, M. Marshall, S. Bordiga, ACS Appl. Mater. Interfaces, 9 (2017) 455-463.

[112] A. Masala, J.G. Vitillo, F. Bonino, M. Manzoli, C.A. Grande, S. Bordiga, Phys. Chem. Chem. Phys., 18 (2016) 220-227.

[113] A. Masala, F. Grifasi, C. Atzori, J.G. Vitillo, L. Mino, F. Bonino, M.R. Chierotti, S. Bordiga, J. Phys. Chem. C, 120 (2016) 12068-12074.

[114] J. Gascon, M.D. Hernndez-Alonso, A.R. Almeida, G.P.M. van Klink, F. Kapteijn, G. Mul, ChemSusChem, 1 (2008) 981-983.

[115] M.R. Ryder, L. Donà, J.G. Vitillo, B. Civalleri, ChemPlusChem, 83 (2018) 308-316.

[116] C.H. Hendon, D. Tiana, M. Fontecave, C. Sanchez, L. D'arras, C. Sassoye, L. Rozes, C. Mellot-Draznieks, A. Walsh, J Am. Chem. Soc., 135 (2013) 10942-10945.

[117] L. Valenzano, B. Civalleri, S. Chavan, S. Bordiga, M.H. Nilsen, S. Jakobsen, K.P. Lillerud, C. Lamberti, Chem. Mater., 23 (2011) 1700-1718.

[118] S. Chavan, J.G. Vitillo, D. Gianolio, O. Zavorotynska, B. Civalleri, S. Jakobsen, M.H. Nilsen, L. Valenzano, C. Lamberti, K.P. Lillerud, S. Bordiga, Phys. Chem. Chem. Phys., 14 (2012) 1614-1626.

[119] V. Guillerm, F. Ragon, M. Dan-Hardi, T. Devic, M. Vishnuvarthan, B. Campo, A. Vimont, G. Clet, Q. Yang, G. Maurin, G. Férey, A. Vittadini, S. Gross, C. Serre, Angew. Chem. Int. Ed., 51 (2012) 9267-9271.

[120] C. Di Nicola, A. Tombesi, M. Moroni, R. Vismara, F. Marchetti, R. Pettinari, L. Nardo, G. Vesco, S. Galli, S. Casassa, L. Pandolfo, C. Pettinari, CrystEngComm, 22 (2020) 3294-3308.

[121] E. Albanese, B. Civalleri, M. Ferrabone, F. Bonino, S. Galli, A. Maspero, C. Pettinari, J. Mater. Chem., 22 (2012) 22592-22602.

[122] G.C. Shearer, V. Colombo, S. Chavan, E. Albanese, B. Civalleri, A. Maspero, S. Bordiga, Dalton Trans., 42 (2013) 6450-6458.

[123] A.M. Walker, B. Civalleri, B. Slater, C. Mellot-Draznieks, F. Corà, C.M. Zicovich-Wilson, G. Romàn-Pérez, J.M. Soler, J.D. Gale, Angew. Chem. Int. Ed., 49 (2010) 7501-7503.

[124] S. Chavan, F. Bonino, L. Valenzano, B. Civalleri, C. Lamberti, N. Acerbi, J.H. Cavka, M. Leistner, S. Bordiga, J. Phys. Chem. C, 117 (2013) 15615-15622.

[125] L. Valenzano, J.G. Vitillo, S. Chavan, B. Civalleri, F. Bonino, S. Bordiga, C. Lamberti, Catal. Today, 182 (2012) 67-79.

[126] L. Valenzano, B. Civalleri, K. Sillar, J. Sauer, J. Phys. Chem. C, 115 (2011) 21777-21784.

[127] L. Valenzano, B. Civalleri, S. Chavan, G.T. Palomino, C.O. Areán, S. Bordiga, J. Phys. Chem. C, 114 (2010) 11185-11191.

[128] B. Civalleri, L. Maschio, P. Ugliengo, C.M. Zicovich-Wilson, Phys. Chem. Chem. Phys., 12 (2010) 6382-6386.

[129] J. Ethiraj, E. Albanese, B. Civalleri, J.G. Vitillo, F. Bonino, S. Chavan, G.C. Shearer, K.P. Lillerud, S. Bordiga, ChemSusChem, 7 (2014) 3382-3388.

[130] A. Erba, J. Baima, I. Bush, R. Orlando, R. Dovesi, J. Chem. Theory Comput., 13 (2017) 5019-5027.

[131] M. D'Amore, B. Civalleri, I.J. Bush, E. Albanese, M. Ferrabone, J. Phys. Chem. C, 123 (2019) 28677-28687.

[132] G. Férey, C. Serre, C. Mellot-Draznieks, F. Millange, S. Surblé, J. Dutour, I. Margiolaki, Angew. Chem. Int. Ed., 43 (2004) 6296-6301.

[133] A. Mavrandonakis, K.D. Vogiatzis, A. Daniel Boese, K. Fink, T. Heine, W. Klopper, Inorg. Chem., 54 (2015) 8251-8263.

[134] B.E. Souza, L. Donà, K. Titov, P. Bruzzese, Z. Zeng, Y. Zhang, A.S. Babal, A.F. Möslein, M.D. Frogley, M. Wolna, G. Cinque, B. Civalleri, J.-C. Tan, ACS Appl. Mater. Interfaces, 12 (2020) 5147-5156.

[135] L. Doná, J.G. Brandenburg, B. Civalleri, J. Chem. Phys., 151 (2019) 121101.

[136] M.R. Ryder, Z. Zeng, K. Titov, Y. Sun, E.M. Mahdi, I. Flyagina, T.D. Bennett, B. Civalleri, C.S. Kelley, M.D. Frogley, G. Cinque, J.-C. Tan, J. Phys. Chem. Lett., 9 (2018) 2678-2684.

[137] F.-X. Coudert, Chem. Mater., 27 (2015) 1905-1916.

[138] K. Titov, Z. Zeng, M.R. Ryder, A.K. Chaudhari, B. Civalleri, C.S. Kelley, M.D. Frogley, G. Cinque, J.-C. Tan, J. Phys. Chem. Lett., 8 (2017) 5035-5040.

[139] A.S. Babal, L. Donà, M.R. Ryder, K. Titov, A.K. Chaudhari, Z. Zeng, C.S. Kelley, M.D. Frogley, G. Cinque, B. Civalleri, J.-C. Tan, J. Phys. Chem. C, 123 (2019) 29427-29435.

[140] M.R. Ryder, B. Civalleri, G. Cinque, J.-C. Tan, CrystEngComm, 18 (2016) 4303-4312.

[141] M.R. Ryder, B. Van de Voorde, B. Civalleri, T.D. Bennett, S. Mukhopadhyay, G. Cinque, F. Fernandez-Alonso, D. De Vos, S. Rudić, J.-C. Tan, Phys. Rev. Lett., 118 (2017) 255502.

[142] M.R. Ryder, B. Civalleri, T.D. Bennett, S. Henke, S. Rudić, G. Cinque, F. Fernandez-Alonso, J.-C. Tan, Phys. Chem. Lett., 113 (2014) 215502.

[143] J.-C. Tan, B. Civalleri, C.-C. Lin, L. Valenzano, R. Galvelis, P.-F. Chen, T.D. Bennett, C. Mellot-Draznieks, C.M. Zicovich-Wilson, A.K. Cheetham, Phys. Chem. Lett., 108 (2012) 095502.

[144] S.A. Moggach, T.D. Bennett, A.K. Cheetham, Angew. Chem. Int. Ed., 48 (2009) 7087-7089.

[145] J. Maul, M.R. Ryder, M.T. Ruggiero, A. Erba, Phys. Rev. B, 99 (2019) 014102.

[146] J.-C. Tan, B. Civalleri, A. Erba, E. Albanese, CrystEngComm, 17 (2015) 375-382.

[147] M.R. Ryder, B. Civalleri, J.-C. Tan, Phys. Chem. Chem. Phys., 18 (2016) 9079-9087.

[148] M.R. Ryder, J. Maul, B. Civalleri, A. Erba, Adv. Theory Simul., 2 (2019) 1900093.

[149] B. Civalleri, G. Maurin, V. Van Speybroeck, Adv. Theory Simul., 2 (2019) 1900196.

[150] R. Vismara, G. Tuci, A. Tombesi, K.V. Domasevitch, C. Di Nicola, G. Giambastiani, M.R. Chierotti, S. Bordignon, R. Gobetto, C. Pettinari, A. Rossin, S. Galli, ACS Appl. Mater. Interfaces, 11 (2019) 26956-26969.

[151] A. Schneemann, V. Bon, I. Schwedler, I. Senkovska, S. Kaskel, R.A. Fischer, Chem. Soc. Rev., 43 (2014) 6062-6096.

[152] D. Britt, D. Tranchemontagne, O.M. Yaghi, Proc. Nat. Acad. Sci., 105 (2008) 11623-11627.

[153] G. Tuci, G. Giambastiani, S. Kwon, P.C. Stair, R.Q. Snurr, A. Rossin, ACS Catal., 4 (2014) 1032-1039.

[154] A. Nowacka, R. Vismara, G. Mercuri, M. Moroni, M. Palomino, K.V. Domasevitch, C. Di Nicola, C. Pettinari, G. Giambastiani, F.X. Llabrés i Xamena, S. Galli, A. Rossin, Inorg. Chem., 59 (2020) 8161-8172.

[155] X.-P. Wu, L. Gagliardi, D.G. Truhlar, J. Am. Chem. Soc. , 140 (2018) 7904-7912.

[156] G. Mercuri, G. Giambastiani, A. Rossin, Inorganics, 7 (2019) 144.

[157] G. Lorusso, J.W. Sharples, E. Palacios, O. Roubeau, E.K. Brechin, R. Sessoli, A. Rossin, F. Tuna, E.J.L. McInnes, D. Collison, M. Evangelisti, Adv. Mater., 25 (2013) 4653-4656.